UNIVERSIDADE FEDERAL DE SANTA CATARINA

CENTRO TECNOLÓGICO

PROGRAMA DE PÓS-GRADUAÇÃO EM ENGENHARIA ELÉTRICA

Christopher da Fonseca Gonçalves

EFFECT OF PARASITIC ELEMENTS IN HIGH-GAIN STEP-UP BOOST CONVERTER WITH COUPLED INDUCTOR GAIN CELL

Florianópolis

2023

Christopher da Fonseca Gonçalves

EFFECT OF PARASITIC ELEMENTS IN HIGH-GAIN STEP-UP BOOST CONVERTER WITH COUPLED INDUCTOR GAIN CELL

Dissertação submetida ao Programa de Pós-Graduação em Engenharia Elétrica da Universidade Federal de Santa Catarina como requisito parcial para a obtenção do título de Mestre em Engenharia Elétrica.

Orientador: Prof. Roberto Francisco Coelho, Dr.
Coorientador: Prof. Lenon Schmitz, Dr.

Florianópolis
2023

Ficha de identificação da obra elaborada pelo autor,
através do Programa de Geração Automática da Biblioteca Universitária da UFSC.

Goncalves, Christopher da Fonseca
Effect of Parasitic Elements in High-Gain Step-Up Boost Converter with Coupled Inductor Gain Cell / Christopher da Fonseca Goncalves ; orientador, Roberto Francisco Coelho, coorientador, Lenon Schmitz, 2023.
124 p.

Dissertação (mestrado) - Universidade Federal de Santa Catarina, Centro Tecnológico, Programa de Pós-Graduação em Engenharia Elétrica, Florianópolis, 2023.

Inclui referências.

1. Engenharia Elétrica. 2. Engenharia Elétrica. 3. Conversores cc-cc não-isolados. 4. Célula de Ganho. 5. Alto ganho. I. Coelho, Roberto Francisco. II. Schmitz, Lenon. III. Universidade Federal de Santa Catarina. Programa de Pós-Graduação em Engenharia Elétrica. IV. Título.

Christopher da Fonseca Gonçalves

EFFECT OF PARASITIC ELEMENTS IN HIGH-GAIN STEP-UP BOOST CONVERTER WITH COUPLED INDUCTOR GAIN CELL

O presente trabalho em nível de Mestrado foi avaliado e aprovado, em 1 de setembro de 2023, pela banca examinadora composta pelos seguintes membros:

Prof. Ricardo Luiz Alves, Dr. Eng.
Instituto Federal de Santa Catarina

Prof. André Luís Kirsten, Dr. Eng.
Universidade Federal de Santa Catarina

Certificamos que esta é a versão original e final do trabalho de conclusão que foi julgado adequado para obtenção do título de Mestre em Engenharia Elétrica.

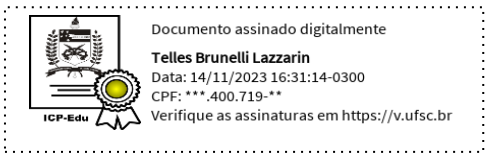

Telles Brunelli Lazzarin, Dr.
Coordenação do Programa de Pós-Graduação

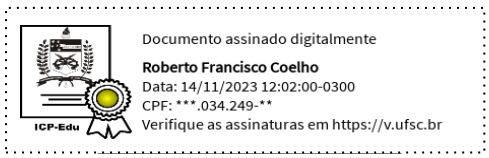

Prof. Roberto Francisco Coelho, Dr.
Orientador

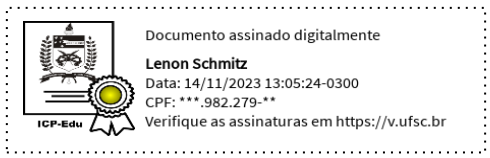

Prof. Lenon Schmitz, Dr.
Coorientador

Florianópolis, 2023.

Aos meus pais,
Sidinei e Luciara.

AGRADECIMENTOS

Quero expressar minha gratidão a todos que fizeram parte da minha caminhada na pós-graduação. Começo agradecendo aos professores Roberto Francisco Coelho e Lenon Schmitz por suas orientações, contribuições e incentivos que viabilizaram a realização deste trabalho. Meu agradecimento também vai para Gabriel Ceolin de Brito, bolsista de iniciação científica, que contribuiu em diversos momentos durante o desenvolvimento deste estudo.

Agradeço aos membros da banca avaliadora, professores Ricardo Luiz Alves e André Luís Kirsten, pela disponibilidade e contribuição que proporcionaram o aprimoramento do presente trabalho com seus conhecimentos. Quero agradecer imensamente também a todos os demais colegas e professores do INEP, pelos ensinamentos e sugestões que de alguma forma contribuíram com este trabalho e com a minha formação. Agradeço a todos os profissionais – equipe técnica, secretaria e terceirizados – que atuam no instituto, pelo profissionalismo e apoio sempre que necessário.

Deixo registrado minha gratidão àqueles que indiretamente participaram desta jornada: a todos que sempre me apoiaram com amizade, carinho, acolhimento, e que não pouparam palavras de incentivo permitindo a superação dos momentos difíceis – em especial a Pedro Luis Ferreira Gois. Agradeço também a CAPES, que através dos impostos do povo brasileiro financia trabalhos como este, incentivando o desenvolvimento da ciência no nosso país.

E, por último, porém a menção que mais transborda gratidão: dedico este trabalho aos meus pais, Sidinei Aguiar Gonçalves e Luciara da Fonseca Gonçalves, por todo amor e pelo apoio incondicional.

RESUMO

Célula de ganho com indutor acoplado é uma técnica muito utilizada para aumentar os níveis de ganho estático e eficiência de conversores cc-cc não isolados baseados no conversor Boost. A técnica combina indutores acoplados a células multiplicadoras de tensão, resultando em várias vantagens desejáveis, como a redução do número de chaves ativas, a possibilidade de ajustar o ganho estático pela relação de espiras do indutor acoplado e a reciclagem da energia armazenada no indutor de dispersão, entre outros recursos. Essa técnica é comumente empregada em conversores Boost com alto ganho (10-30) e alto rendimento (>95%). A modelagem desses conversores abordada na literatura frequentemente se baseia em componentes ideais, resultando em respostas dinâmicas com diferenças consideráveis quando comparadas ao comportamento real de um conversor. Esta dissertação aborda uma análise que inclui elementos parasitas na modelagem de conversores Boost integrados a células de ganho com indutor acoplado operando no modo de condução contínua. Esses elementos parasitas causam perdas nos MOSFETs, diodos, capacitores e no indutor acoplado, representados por meio de modelos equivalentes que são introduzidos nos modelos dos conversores. Um protótipo de um conversor Boost com célula de ganho com indutor acoplado foi construído para validar experimentalmente os modelos desenvolvidos. Mesmo que a inclusão de elementos parasitas na modelagem de conversores cc-cc de alto ganho e alto rendimento resulte em equações mais complexas do que aquelas obtidas com modelos ideais, por meio de testes de resposta ao degrau e resposta em frequência realizados com o protótipo, ficou claro que a inclusão desses componentes gera modelos mais precisos.

Palavras-chave: Conversores cc-cc de alto ganho e alto rendimento; Células de ganho com indutor acoplado; Elementos parasitas.

RESUMO EXPANDIDO

Introdução

Nos últimos anos, os sistemas de energia elétrica passaram por transformações consideráveis: a geração de eletricidade anteriormente era principalmente produzida por meio de grandes usinas de energia centralizadas em um único local, no entanto, hoje em dia, a entrada de pequenos sistemas de geração distribuída está mudando esse cenário. A integração da geração descentralizada à rede elétrica principal está permitindo que pequenas empresas explorem e expandam, por exemplo, o uso dos chamados painéis solares com tecnologia fotovoltaica (FV).

Atualmente, um grande esforço está concentrado na evolução do processamento de energia, pois assim tecnologias como a FV podem se tornar mais eficientes e lucrativas. Tecnologias de eletrônica de potência altamente eficientes e estratégias de controle adequadas são necessárias para reduzir o desperdício de energia e melhorar os parâmetros de desempenho. A conversão de energia é uma etapa que requer atenção especial à sua eficiência e ganho, pois a tensão de saída obtida no módulo FV tem baixo nível de corrente contínua (CC) e deve ser aumentada e posteriormente convertida em uma tensão alternada para ser conectada à rede. Para atingir a tensão da rede, um dispositivo eletrônico de potência chamado conversor CC-CC é amplamente utilizado. Com esse dispositivo, a tensão de entrada CC é convertida em uma tensão de saída CC com uma magnitude maior.

Neste contexto, o conversor *Boost* (elevador) é uma topologia de conversor CC-CC não isolado capaz de produzir tensões de saída com magnitude maior que a tensão de entrada. Aumentar a eficiência e o ganho de tensão é a chave para obter potências de saída mais elevadas com esses circuitos. Embora, em teoria, um conversor *Boost* ideal possa ser usado para obter ganho elevado, uma vez que eles têm ganho estático ilimitado quando a razão cíclica se aproxima da unidade, na prática, sob valores elevados de razão cíclica, a eficiência do conversor é drasticamente reduzida, limitando seus ganhos. Essa redução na eficiência se deve principalmente ao aumento das perdas por condução nos componentes, causado pelo alto valor de pico de corrente em regiões de razão cíclica próxima da unidade. Além disso, semicondutores de alta tensão são necessários para níveis elevados de tensão de saída, aumentando ainda mais as perdas por condução e comutação, devido

às suas características elétricas. Assim, para aumentar os níveis de ganho estático e eficiência dos conversores cc-cc sem a imposição de elevadas razões cíclicas, diferentes técnicas podem ser aplicadas. Em [9], foi apresentada uma família de conversores cc-cc elevadores de alto ganho capazes de obter ganhos elevados (10-30) e eficiência elevada (>95%) aplicando uma técnica de projeto que integra circuitos chamadas células de ganho ao conversor *Boost*.

Uma estrutura de célula de ganho basicamente possui células multiplicadoras de tensão interconectadas com indutores acoplados, proporcionando novas características ao conversor resultante e mantendo algumas de suas características originais. Algumas dessas novas características são vantagens desejáveis, como a possibilidade de ajustar o ganho estático pela relação de espiras do indutor acoplado; exigência de chaves com tensões de estresse e bloqueio menores que a tensão de saída; possibilidade de reciclar a energia armazenada no indutor de dispersão, fato que permite aumentar a eficiência e evitar sobretensões nos interruptores ativos; oportunidade de incorporar a característica de comutação suave na maioria dos conversores, implicando na redução das perdas por comutação e interferência eletromagnética (EMI); mitigação do problema de recuperação reversa relacionado aos diodos por meio da indutância de vazamento; e redução do número de interruptores ativos, resultando em circuitos de controle relativamente simples [8].

Este estudo propõe a consideração de componentes parasitas nos modelos médios de conversores elevadores. O modelo médio ideal do conversor elevador não descreve suficientemente um conversor, pois na prática resistências parasitas estão presentes [11]. Componentes parasitas reduzem consideravelmente o desempenho do conversor, destacando a resistência série equivalente do indutor, a resistência série equivalente do capacitor, a resistência do estado ligado da chave, a tensão de condução do diodo e sua resistência direta, além do efeito da indutância de dispersão, também representado como resistências série equivalentes, conforme proposto em [8].

Objetivos

- Propor modelos médios de conversores elevadores com célula de ganho com indutor acoplado, levando em consideração componentes parasitas;
- Comparar os modelos propostos com modelos médios ideais (sem perdas);

- Construir um protótipo de conversor CC-CC elevador com célula de ganho para comparar a resposta dos modelos propostos com a resposta real do conversor;

- Realizar e analisar a resposta ao degrau no ciclo de trabalho e a resposta em frequência do protótipo construído;

- Validar experimentalmente os modelos e conceitos propostos.

Metodologia

Para o desenvolvimento dos modelos propostos e do protótipo utilizado para validação deste estudo, uma extensa revisão teórica sobre os conversores trabalhados foi realizada. Foi desenvolvida a modelagem de três configurações de conversores elevadores utilizando células de ganho com indutor acoplado considerando componentes parasitas, e para validar estes modelos foram conduzidos testes comparativos com modelos ideias destes conversores através de simulações computacionais e com testes de bancada com o protótipo.

Resultados e Discussão

Este estudo examinou detalhadamente os elementos-chave que constituem um conversor elevador CC-CC de alto ganho com células de ganho com indutor acoplado operando em modo de condução contínua. Foi apresentada uma análise da modelagem de um conversor elevador ideal, juntamente com o conceito de indutor acoplado e seu modelo elétrico equivalente. Posteriormente, o conceito de célula de ganho foi abordado, e as três configurações escolhidas para este estudo foram introduzidas, discutindo a modelagem do conversor em cada configuração.

Foram estudados os componentes parasitas mais relevantes nesse tipo de conversor, apresentando o conceito de perdas nos MOSFETs, diodos, capacitores e indutor acoplado. Essas perdas foram representadas por meio de modelos equivalentes que foram introduzidos nos modelos dos conversores de células de ganho em discussão. A inclusão desses elementos resultou em equações mais complexas do que as obtidas com os modelos ideais, gerando funções de transferências de ordens significativamente mais elevadas. Os modelos foram validados por meio de simulações dos modelos de pequenos sinais destes conversores.

Na etapa final deste estudo o protótipo do conversor elevador CC-CC com célula de ganho com indutor acoplado foi construído, sendo utilizado para comparar os resultados obtidos a partir dos modelos desenvolvidos com a resposta real do conversor. Foram realizados testes de resposta ao degrau e resposta em frequência, e os resultados obtidos apoiam a tese de que a inclusão de componentes parasitas na modelagem de conversores elevadores de alto ganho gera modelos mais precisos do que os modelos ideais.

Considerações Finais

O uso de modelos dinâmicos mais complexos e precisos para projetar um conversor CC-CC pode ser recomendado em alguns cenários, tais como: quando é necessária uma compreensão detalhada do comportamento do conversor, especialmente em condições operacionais complexas ou sob diversas cargas e níveis de tensão de entrada, comuns em pesquisa ou desenvolvimento de tecnologias de ponta; para o design de estratégias avançadas de controle, especialmente em aplicações onde a regulamentação rigorosa da tensão de saída ou corrente é crucial, uma vez que modelos precisos são essenciais para análise de estabilidade e ajuste de malhas de controle; em situações em que a previsão precisa de respostas transitórias - como inicialização, desligamento ou transientes de carga - é crucial, para garantir que o conversor possa lidar com mudanças rápidas nas condições operacionais.

Além disso, para conversores operando em altas frequências de comutação, onde elementos parasitas - como capacitâncias parasitas, indutâncias e interferência eletromagnética - têm um impacto significativo, modelos precisos são necessários para considerar esses efeitos. Outro cenário relevante é ao lidar com topologias de conversores não convencionais ou avançadas, como conversores de vários níveis, conversores ressonantes ou topologias de comutação suave. Essas topologias frequentemente têm modos de operação complexos que exigem modelagem precisa. Ambientes de pesquisa ou no desenvolvimento de protótipos para novas tecnologias, onde uma compreensão profunda do comportamento do conversor é necessária para validar modelos teóricos e testar novos conceitos, e em aplicações onde a segurança é fundamental, como dispositivos médicos ou sistemas aeroespaciais, a modelagem precisa é essencial para garantir que o conversor opere de maneira confiável em todas as condições.

Como trabalho futuro, sugere-se aprofundar o estudo da representação de componentes parasitas na modelagem de conversores CC-CC. Especificamente, a representação da indutância de vazamento do indutor acoplado, juntamente com a estimativa de suas perdas por cobre e núcleo, requer elaboração teórica para aprimoramento de modelos de perdas.

Palavras-chave: Conversores cc-cc de alto ganho e alto rendimento; Células de ganho com indutor acoplado; Elementos parasitas.

ABSTRACT

Coupled-inductor gain cell is a technique used to increase the static gain and efficiency levels of dc-dc Boost converters. It combines coupled inductors to voltage multiplier cells resulting in desirable advantages, such as reduced number of active switches, possibility of adjusting the static gain by the turns ratio of the coupled inductor and recycling the energy stored in the leakage inductor, among other interesting features. This technique is commonly employed in high-gain step-up dc-dc converters capable of obtaining high gain (10-30) and high efficiency (>95%). The modeling of these converters addressed in the literature is often based on ideal components, resulting in dynamic responses with considerable differences when compared to a real converter behavior. This thesis addresses an analysis including parasitic elements in the modeling of Boost converters with coupled inductor gain cells operating in continuous conduction mode. These parasitic elements are losses in the MOSFET, diodes, capacitors, and coupled inductor, represented through equivalent models that are introduced into the models of the converters. A prototype of a Boost converter with coupled-inductor gain cell was built to validate experimentally the developed models. Even if the inclusion of parasitic elements in the modeling of high-gain step-up dc-dc converters results more complex equations than those equations obtained with ideal models, through step-response and frequency-response tests performed with the prototype became clear that including these components generates more accurate models.

Keywords: High-gain step-up dc-dc converters; Coupled-inductor gain cells; Parasitic elements.

LIST OF FIGURES

LIST OF TABLES

LIST OF ABBREVIATIONS AND ACRONYMS

AC	Alternated Current
ANEEL	National Agency of Electric Energy
CCM	Continuous Conduction Mode
CSP	Concentrated Solar Power
DC	Direct Current
EMI	Electromagnetic Interference
ESR	Equivalent Series Resistance
GC	Gain Cell
Ge	Germanium
PV	Photovoltaics
SHC	Solar Heating and Cooling
Si	Silicon
ZCS	Zero-Current Switching
ZVS	Zero-Voltage Switching
RMS	Root Mean Square

LIST OF SYMBOLS

a	Gain cell parameter
b	Gain cell parameter
C	Capacitor
C_1	Capacitor C_1
C_2	Capacitor C_2
C_3	Capacitor C_3
C_4	Capacitor C_4
C_o	Output Capacitor
C_{GC}	Gain Cell Capacitor
d	Duty cycle signal
D	Duty cycle
D_1	Diode D_1
D_2	Diode D_2
D_3	Diode D_3
D_4	Diode D_4
D_{GC}	Gain Cell Diode
D_x	Ratio between the time during which diode D_1 conducts and the switching period T of the Boost converter with gain cell
f_s	Switching Frequency
i_1	Couple-Inductor Primary Current
I_1	Couple-Inductor Primary Current Average Value
I_{1rms}	Couple-Inductor Primary Current RMS Value
i_2	Couple-Inductor Secondary Current
I_2	Couple-Inductor Secondary Current Average Value
I_{2rms}	Couple-Inductor Secondary Current RMS Value
I_{2a}	Couple-Inductor Secondary Current Peak Value
I_{2b}	Couple-Inductor Secondary Current Peak Value
I_{2c}	Couple-Inductor Secondary Current Peak Value
I_{Crms}	Capacitor Current RMS Value
i_{C1}	Capacitor C_1 Current

i_{C2}	Capacitor C_2 Current
i_{C3}	Capacitor C_3 Current
i_{C4}	Capacitor C_4 Current
i_{Co}	Capacitor C_o Current
I_D	Diode Current
I_{Drms}	Diode Current RMS Value
i_{in}	Input Current
i_{Lm}	Magnetizing Inductance Current
I_{Lm}	Magnetizing Inductance Current Average Value
I_{Lkp}	Leakage Inductor Current Peak Value
I_g	Gate Current
I_m	Magnetizing Inductance Current Minimum Value
I_M	Magnetizing Inductance Current Maximum Value
i_o	Output Current
I_o	Output Current Average Value
i_{S1}	Switch Current
I_{S1}	Switch Current Average Value
I_{S1p}	Switch Current Peak Value
L	Inductor
L_1	Inductor L_1
L_2	Inductor L_2
L_m	Magnetizing inductor
L_k	Leakage Inductor
M	Static Gain
n	Transformer Turns Ratio
n_1	Primary Turns Number
n_2	Secondary Turns Number
P_{cond}	Semiconductor Conduction Losses
P_{C-ESR}	Capacitor Losses
P_D	Diode Losses
P_S	MOSFET Losses
P_{switch}	Switching Losses

Q_{sw}	Switching Gate Charge
R_1	Coupled-Inductor Primary Losses Equivalent
R_2	Coupled-Inductor Secondary Losses Equivalent
R_{C-ESR}	Capacitor Equivalent Series Resistance
R_{C1}	Capacitor C_1 Equivalent Series Resistance
R_{C2}	Capacitor C_2 Equivalent Series Resistance
R_{C3}	Capacitor C_3 Equivalent Series Resistance
R_{C4}	Capacitor C_4 Equivalent Series Resistance
R_{D1}	Diode D_1 Equivalent Series Resistance
R_{D2}	Diode D_2 Equivalent Series Resistance
R_{D3}	Diode D_3 Equivalent Series Resistance
R_{D4}	Diode D_4 Equivalent Series Resistance
r_{ds}	Drain-Source Resistance
R_L	Inductor Equivalent Series Resistance
R_{L1}	Inductor L_1 Equivalent Series Resistance
R_{L2}	Inductor L_2 Equivalent Series Resistance
R_{Lk1}	Primary Leakage Inductance Equivalent Series Resistance
R_{Lk2}	Secondary Leakage Inductance Equivalent Series Resistance
R_g	Gate Resistance
r_T	Diode Conduction Resistance
R_o	Output Resistor
S	Switch
T	Switching Period
t_{ON}	Switching Turn-on time
t_{OFF}	Switching Turn-off time
t_x	Diode D_1Conducting Time
V_a	Positive Portion of the Voltage Across Inductor L1
V_b	Absolute Value of Negative Portion of the Voltage Across Inductor L1
V_B	Boost Voltage
V_{C1}	Capacitor C_1Voltage
V_{C2}	Capacitor C_2Voltage
V_{C3}	Capacitor C_3Voltage

V_{C4}	Capacitor C_4 Voltage
V_{Cb}	Capacitor C_b Voltage
V_{Co}	Capacitor C_o Voltage
V_{Df}	Diode Forward Voltage
V_{F1}	Diode D_1 Forward Voltage
V_{F2}	Diode D_2 Forward Voltage
V_{F3}	Diode D_3 Forward Voltage
V_{F4}	Diode D_4 Forward Voltage
V_{gs}	Gate-Source Voltage
V_i	Input Voltage
v_{L1}	Coupled-Inductor Primary Voltage
v_{L2}	Coupled-Inductor Secondary Voltage
V_{Lk1}	Leakage-Inductor Primary Voltage
V_{Lk2}	Leakage-Inductor Secondary Voltage
V_{Lm}	Magnetizing Inductor Voltage
V_o	Output Voltage
V_P	Gate *Plateau* Voltage
V_T	Diode Conduction Voltage

CONTENTS

1 INTRODUCTION

1.1 CONTEXTUALIZATION

In recent years, electrical power systems have been undergoing considerably transformations: the electricity generation before was mainly produced through large power plants centralized in one site, however nowadays the entry of small distributed generation systems is changing this scenario. Because of this diversification of the energy matrix, the relationship between consumers and the distribution system has changed – the consumer that until then was just a load on the network, now can also contribute as power generator. The energy that circulated only in a one-way direction, from the source to the loads, starts to circulate bidirectionally, and the electricity network must be rethought. Brazil, which had a matrix based on hydraulic and thermoelectric generation, began to expand its generation system by adding renewable energy sources such as wind energy, biomass, biofuels, solar, cogeneration, among others [1].

With a considerably high average daily global horizontal solar irradiation (an amount between 1500 and 2500 kWh/m^2), Brazil underutilized its solar resource with low investments in solar power technologies for many years [2]. The Brazilian Regulatory Agency has been conceiving technical notes and promoting public hearings since 2010 to discuss the solar energy use, like micro and mini distributed generation, to stimulate the development of this energy market [3]. A substantial step to the dissemination of these systems is the ANEEL 482/2012 resolution about the integration of decentralized generation to the main electricity network, allowing small companies to explore and expand, for example, the use of the so-called *solar panels* across the country. Because of favorable energy policies, solar photovoltaics is one of the main renewable energy sources to be deployed in Brazil and around the globe in an effort to decrease greenhouse gas emissions in the energy sector [4].

Three main technologies are used for harvesting energy from the sun, namely Solar Heating and Cooling (SHC), Concentrated Solar Power (CSP), and Solar Photovoltaics (PV). The PV technology is the only solar technology that directly converts the sunlight into electricity in direct current (DC) form using an array of modules made with semiconductor materials fabricated usually from the elements Silicon (Si) or Germanium (Ge) [22]. But a PV system is much more than that, and the rest of the components of the

system perform the critical task of making the power generated usable for several appliances. The basic components required for PV electricity generation would be more or less similar for all types of PV installations, grouped into four categories: PV modules, power electronic devices, energy storage devices, and electrical and mechanical components [5].

Figure 1.1 shows a common schematic of a PV system. The PV modules are an attractive energy source due to their relatively small size, noiseless operation, simple installation, and the possibility of installing them closer to the user [6]. This explains why PV is one of the fastest-growing energy generation options available in the modern energy sector.

Figure 1.1 – Schematic of a generic PV system.

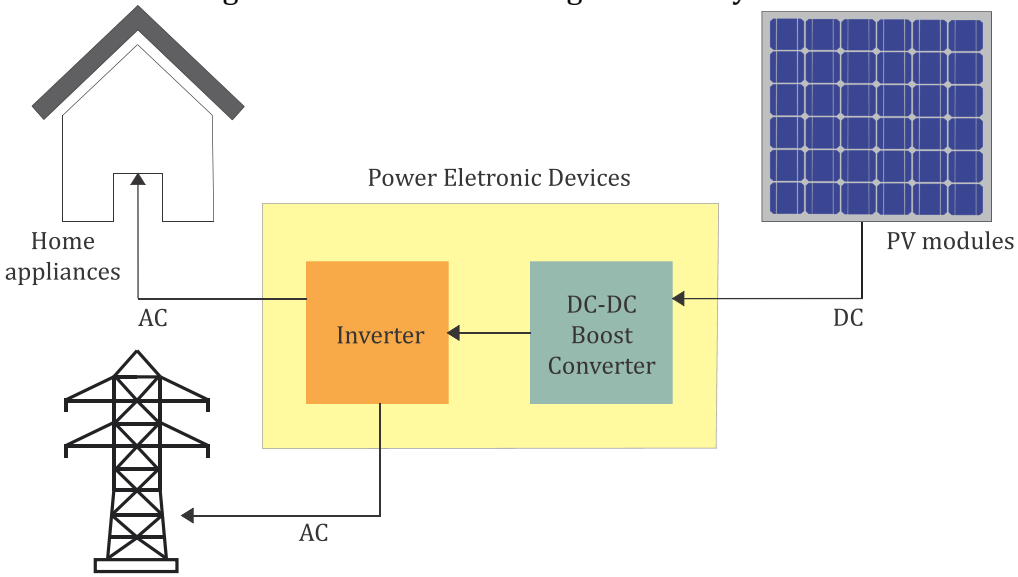

Source: Elaborated by the author.

The PV power generators can be classified into stand-alone system, in which the energy storage has a great influence on the design of the systems; and grid-connected systems, with the grid acting as an energy storage in which the PV power generator can inject power whenever power is available. There are also hybrid solar PV systems, which typically represent the combination of both grid-tied and stand-alone; the PV system generates electrical power to the local consumption or to store in batteries, and the excess is injected into the grid by means of net metering [4].

1.2 POWER ELECTRONICS AND ENERGY CONVERSION

A great effort is concentrated now in the evolution of the power processing of PV technology to become more efficient and lucrative. Highly efficient power electronic technologies and proper control strategies are therefore needed to reduce energy waste and to improve performance parameters [6]. The energy conversion is a stage that requires close attention to its efficiency and gain, as the output voltage obtained in the PV module has low DC level and it has to be increased and later converted into an AC voltage to be connected to the grid. To reach the grid voltage, a power electronic device called *dc-dc converter* is broadly used as first stage PV inverters. With this device, the dc input voltage is converted to a dc output voltage with a larger magnitude.

In this matter, the *boost converter* shown in the Figure 1.2 is a topology of non-isolated dc-dc converter capable of producing output voltages that are larger in magnitude than the input voltage. Increasing the efficiency and voltage gain is the key to obtaining higher output powers with these circuits. The design of switching converters seeking negligible power dissipation must avoid resistive and linear-mode semiconductor devices, applying capacitive and inductive elements; switched-mode semiconductor devices can be used as well, once they have low power dissipation [7].

Figure 1.2 – Ideal boost converter topology.

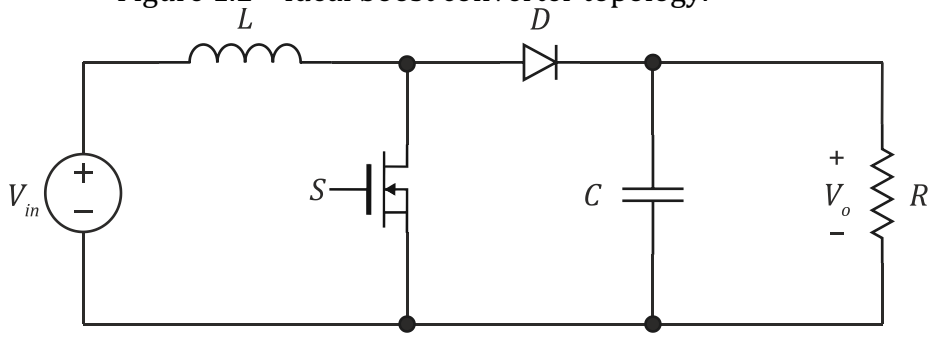

Source: Elaborated by the author.

Although in theory an ideal boost converter can be used to obtain high-gain since they have unlimited static gain when the duty cycle approaches unity, practically under high values of duty cycle the converter efficiency is drastically reduced, limiting their gains. This reduction in efficiency is mainly due to the increase in conduction losses in the components, caused by the current high-peak value in regions of duty cycle close to unity. Furthermore, high-voltage semiconductors are required for high-output-voltage levels,

increasing even more the conduction and switching losses, because of their electrical characteristics [8]. Thus, to increase the static gain and efficiency levels of dc-dc converters without the imposition of high duty cycles, different techniques can be applied. In [9] was presented a family of high-gain step-up dc-dc converters capable of obtaining high gain (10-30) and high efficiency (>95%) applying a design technique that integrates circuitry called *gain cells* to the boost converter, as shown in Figure 1.3.

Figure 1.3 – Generalization of boost converter with gain cell.

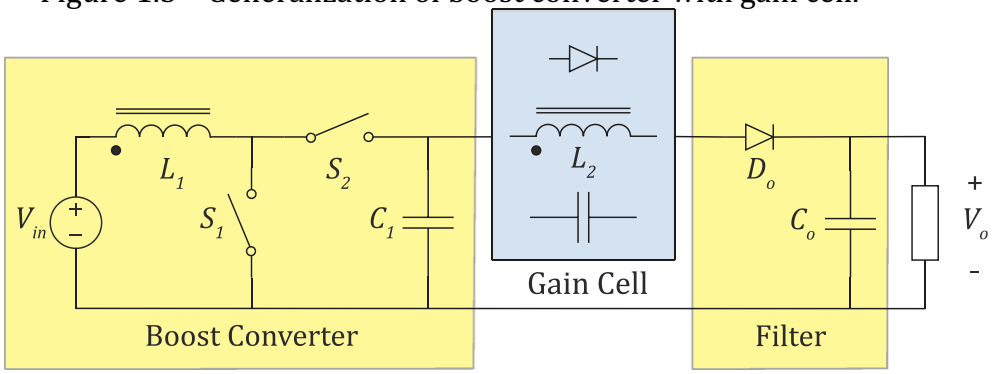

Source: Adapted from [8].

A gain cell structure basically has voltage multiplier cells interconnected with couple inductors providing new features to the resulting converter and keeping some of its original characteristics. Some of these new features are desirable advantages, such as the possibility of adjusting the static gain by the turns ratio of the coupled inductor; requirement of switches with voltage stresses and blocking voltage smaller than the output voltage; possibility of recycling the energy stored in the leakage inductor, a fact that allows increasing efficiency and avoiding overvoltages in active switches; opportunity to incorporate soft-switching feature on most converters, implying reduction of switching losses and electromagnetic interference (EMI); mitigation of the reverse recovery problem related to the diodes through the leakage inductance; and reduced number of active switches, resulting in relatively simple control circuits [8].

1.3 POWER ELECTRONICS AND ENERGY CONVERSION

Three configurations of gain cells are addressed in this work, according to the topologies proposed in [9]: gain cell I (GC-I), gain cell III (GC-III) and gain cell V (GC-V). In the next chapter the difference among these gain cells is covered in detail, keeping the same terminology used in [9]. In addition, this study proposes the consideration of

parasitic components in the estimation of efficiency and gain obtained by use of gain cells in boost-converters average models. Parasitic components reduce considerably the converter performance, highlighting the *inductor equivalent series resistance*, the capacitor *equivalent series resistance*, the *switch on-state resistance*, the *diode conduction voltage* and its *forward resistance*, besides the *leakage-inductance* effect. Choosing to add these parasitic components mostly as resistances is possible, since their impact is seeing mostly in the damping factor of the system and losses by Joule effect [10]. Figure 1.4 shows a boost converter with gain cell considering the parasitic resistances.

Figure 1.4 – Example of boost converter with gain cell and parasitic components.

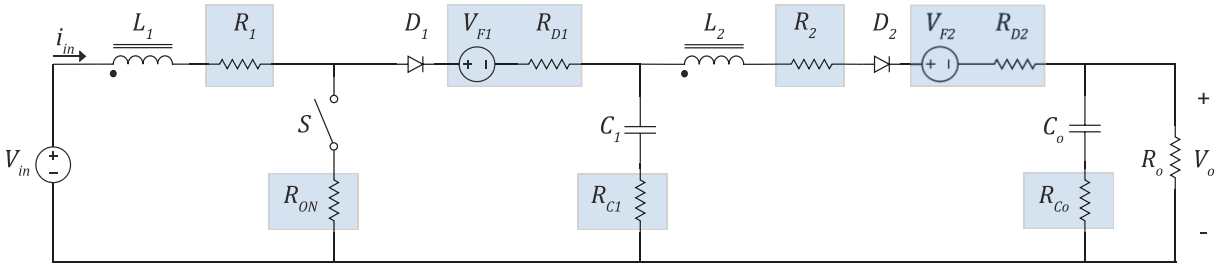

Source: Elaborated by the author.

Average models in general can be obtained by replacing the switched components of the converter - switch and diodes - by their average equivalent quantities over an operation stage, identifying the levels of voltage or current in these elements for each operation stage. These models are essential to understand the dynamic behavior of switching converters. The lossless average model does not sufficiently describe a converter since in practice parasitic resistances are present [11]. A comparation between the *lossless high-gain step-up boost converter with gain cell model* and the *lossy high-gain step-up boost converter with gain cell* is presented in the next chapters for better understanding of the importance of working with more accurate models oriented to controller designs and stability analysis.

1.4 OBJECTIVES

1.4.1 GENERAL OBJECTIVE

Analyze the effects of adding parasitic components in the average model of dc-dc high-gain step-up boost converters with coupled inductor gain cells, in order to represent more accurately their real dynamic response.

1.4.2 SPECIFIC OBJECTIVES

- Propose boost converter with coupled inductor gain cell average models accounting parasitic components;
- Compare the proposed models to ideal (lossless) average models;
- Build a dc-dc boost converter with gain cell prototype to compare the proposed models response to the real converter response;
- Perform and analyze duty cycle step-response and frequency-response of the built prototype;
- Experimental validation of the proposed models and concepts.

1.5 THESIS STRUCTURE

The topics composing this document structure are presented as follows:

- An introductory contextualization of the overall theme covered by this study (Chapter 1);
- Conceptualization of gain cells and their integration to ideal boost converters in different topologies operating in continuous conduction mode (Chapter 2);
- Overview about parasitic components in dc-dc converters and average modeling of lossy boost converters integrated to different gain cell configurations operating in continuous conduction mode (Chapter 3);
- Practical evaluation of high-gain step-up dc–dc boost-based converters with coupled-inductor gain cell and comparation with the theoretical model previously simulated (Chapter 4);
- Final considerations and future studies (Chapter 5).

2 IDEAL BOOST CONVERTER INTEGRATED TO COUPLED INDUCTOR GAIN CELLS: CONCEPTUAL OVERVIEW

This chapter presents the definitions and basic operation of the main components of a high-gain step-up boost-based converter with gain cell, also showing some topological variations explored in this study. This conceptual overview of the ideal models is fundamental to understanding how each aspect of the chosen converters work with each other, giving a background to comprehend how the parasitic components addressed in the next chapters can modify the ideal models.

2.1 IDEAL BOOST CONVERTER IN CCM

The basic circuit of an ideal boost dc–dc converter is shown in Figure 2.1. It consists of an inductor L, a power MOSFET, a diode D_1, a filter capacitor C, and a load resistor R_L. The converter output voltage V_o is always higher than the input voltage V_{in} for steady-state operation, "boosting" the voltage to a higher level. The switch S is turned ON and OFF at the switching frequency $f_s = 1/T$ with the ON duty ratio $d = t_{ON}/T$, where t_{ON} is the time interval when the switch S is ON. The equivalent circuits of the boost converter operating in continuous conduction mode (CCM) are shown in Figure 2.2(a) and 2.2(b) to illustrate the converter behavior when the switch S is ON and the diode is OFF, and when the switch is OFF and the diode is ON, respectively.

Figure 2.1 – Ideal boost converter.

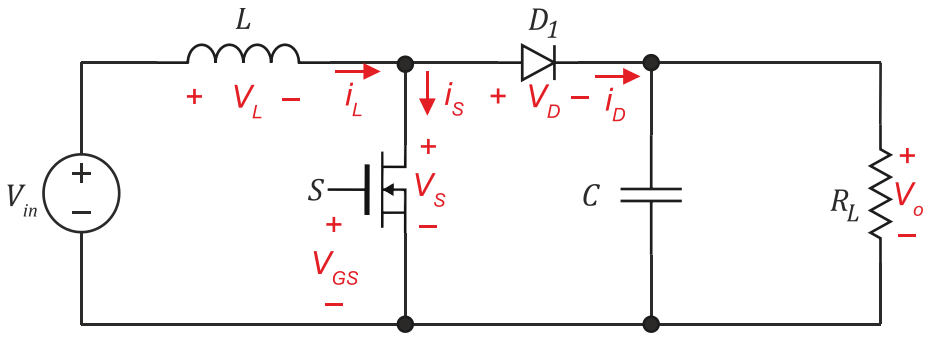

Source: Elaborated by the author.

Figure 2.2 – Equivalent boost converter circuit with: (a) Switch ON and diode OFF; (b) Switch OFF and diode ON.

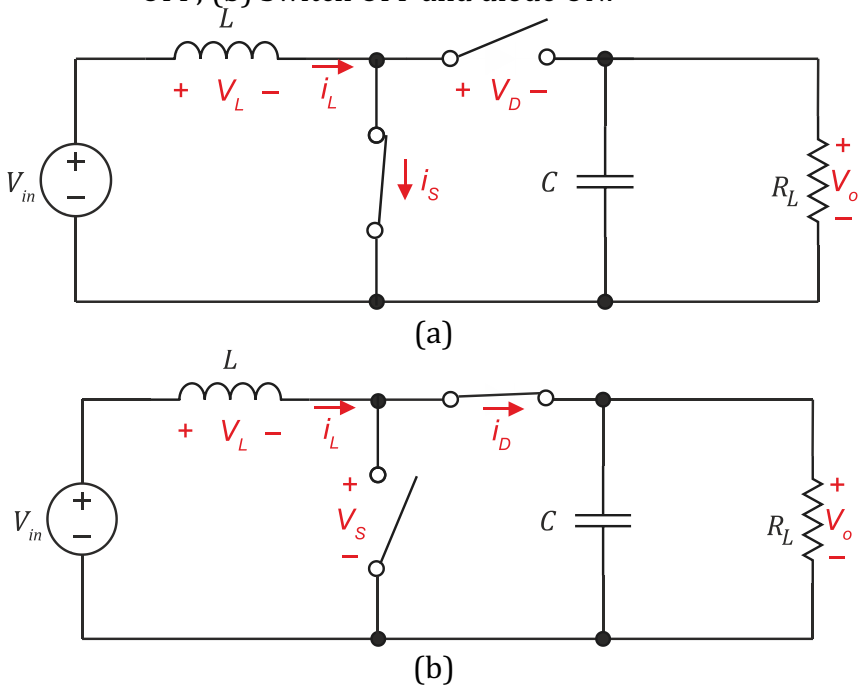

Source: Elaborated by the author.

The principle of operation of the boost converter can be explained analyzing the waveforms of the currents and voltages presented in Figure 2.3. The switch is ON for the time interval $0 < t \leq DT$ and the voltage across the diode is $V_D = -V_o$, causing the diode to be reverse biased. Across the inductor, the voltage is $v_L = V_{in}$ and the inductor current increases linearly with a slope of V_{in}/L, causing to the magnetic energy to increase as well. The switch current is equal to the inductor current [12].

When the switch is turned off by the gate-to-source signal, the inductor starts to act as a current source and turns the diode ON at $t = DT$. Thus, the voltage across the inductor is now $V_L = V_{in} - V_o < 0$. The current across the inductor decreases with a slope of $(V_{in} - V_o)/L$, and the diode current is equal to the inductor current. Over this time interval, the energy is transferred from the inductor L to the filter capacitor C and the load resistance R_L, until the switch is turned ON again, terminating the cycle, at time $t = T$.

Analyzing the operation stages of Figure 2.2(a) and Figure 2.2(b), the state equations of each stage are obtained for the converter model. For the first stage:

$$\frac{di_L}{dt} = \frac{V_{in}}{L}, \tag{2.1}$$

$$\frac{dv_o}{dt} = -\frac{v_o}{R_o C_o}. \tag{2.2}$$

Figure 2.3 – Current and voltage waveforms in the boost converter for CCM.

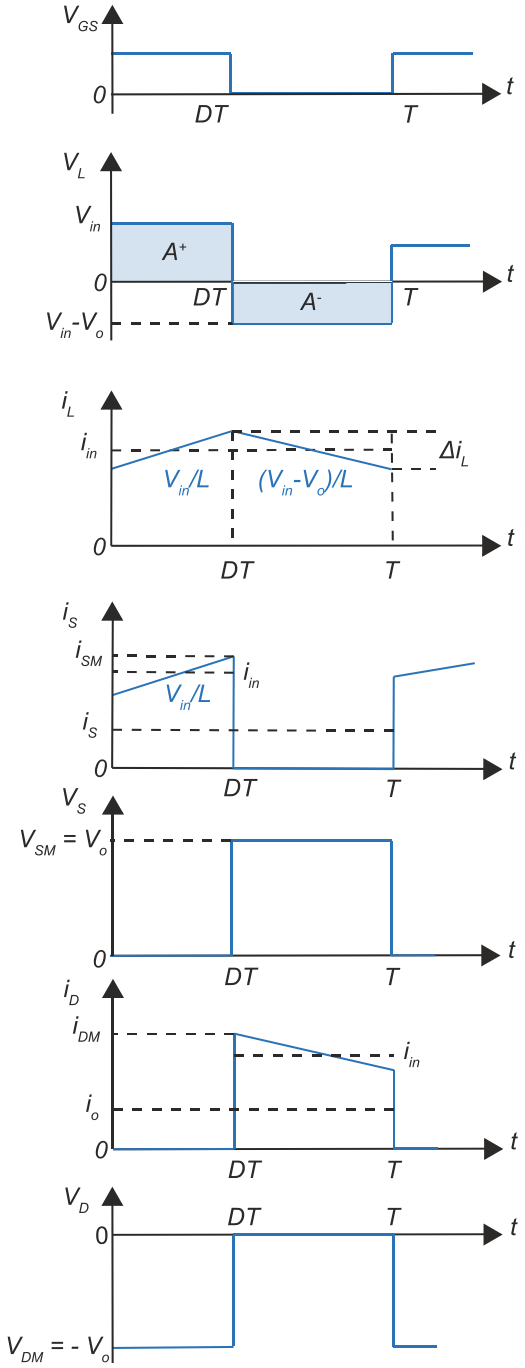

Source: Elaborated by the author.

For the second operation stage of the boost converter, the state equations are:

$$\frac{di_L}{dt} = \frac{V_{in} - v_o}{L}, \tag{2.3}$$

$$\frac{dv_o}{dt} = \frac{i_L}{C_o} - \frac{v_o}{R_o C_o} \quad . \tag{2.4}$$

The average large-signal model represents the low frequency operation of the Boost converter, in which switching information is lost. After obtaining the state equations, their quasi-instantaneous average values are calculated over a switching period according to each operation stage. So, considering $d' = 1 - d$, and accounting the equations (2.1), (2.2), (2.3) and (2.4):

$$\frac{d\langle i_L\rangle}{dt} = \frac{\langle v_{in}\rangle . d}{L} + \frac{(\langle v_{in}\rangle - \langle v_o\rangle) . d'}{L} \quad , \tag{2.5}$$

$$\frac{d\langle v_o\rangle}{dt} = -\frac{\langle v_o\rangle . d}{R_o C_o} + \frac{(R_o\langle i_L\rangle - \langle v_o\rangle) . d'}{R_o C_o} \quad . \tag{2.6}$$

Equations (2.7) and (2.8) are extracted after simplifying equations (2.5) and (2.6), respectively:

$$\frac{d\langle i_L\rangle}{dt} = \frac{\langle v_{in}\rangle - \langle v_o\rangle d'}{L}, \tag{2.7}$$

$$\frac{d\langle v_o\rangle}{dt} = \frac{\langle i_L\rangle d'}{C_o} - \frac{\langle v_o\rangle}{R_o C_o}. \tag{2.8}$$

The large-signal average model is useful for analyzing the converter behavior throughout the duty cycle excursion range. However, there are non-linearities that need to be eliminated, so the system is linearized with the inclusion of small perturbations ($\hat{\imath}_L, \hat{d}$ and $\hat{v}_0$) around the operation points in the equations elements, as follow:

$$\langle i_L\rangle = I_L + \hat{\imath}_L, \tag{2.9}$$

$$\langle d\rangle = D + \hat{d}, \tag{2.10}$$

$$\langle v_o\rangle = V_o + \hat{v}_0. \tag{2.11}$$

Adding (2.9), (2.10) and (2.11) to (2.7) it is possible to obtain:

$$\frac{d\langle I_L + \hat{\imath}_L\rangle}{dt} = \frac{V_{in} - (V_o + \hat{v}_0)(D' - \hat{d})}{L} \quad , \tag{2.12}$$

$$\frac{d\langle I_L\rangle}{dt} + \frac{d\langle \hat{\imath}_L\rangle}{dt} = \frac{V_{in} - V_o D' - D'\hat{v}_0 + V_o\hat{d} + \hat{v}_0\hat{d}}{L} \quad . \tag{2.13}$$

Neglecting the second-order term in (2.13), as the multiplication of two small perturbations tends to be very close to zero, it is obtained:

$$\frac{d\langle I_L\rangle}{dt}+\frac{d\langle \hat{\imath}_L\rangle}{dt}=\frac{V_{in}-V_oD'-D'\hat{v}_0+V_o\hat{d}}{L}\ . \tag{2.14}$$

Equation (2.14) is equivalent to the sum of two terms, one of zero order and the other of first order, so:

$$0=\frac{d\langle I_L\rangle}{dt}=\frac{V_{in}-V_oD'}{L}\ , \tag{2.15}$$

$$\frac{d\langle \hat{\imath}_L\rangle}{dt}=\frac{-D'\hat{v}_0+V_o\hat{d}}{L}\ . \tag{2.16}$$

To find the new value of the equivalent output voltage source, the equations (2.9), (2.10) and (2.11) are inserted in (2.8), and the same procedure is followed. Then, it is obtained:

$$\frac{d\langle V_o+\hat{v}_0\rangle}{dt}=\frac{(I_L+\hat{\imath}_L)(D'-\hat{d})}{C_o}-\frac{(V_o+\hat{v}_0)}{R_oC_o}\ , \tag{2.17}$$

$$\frac{d\langle V_o\rangle}{dt}+\frac{d\langle \hat{v}_0\rangle}{dt}=\frac{I_LR_oD'-I_LR_o\hat{d}+R_oD'\hat{\imath}_L-R_o\hat{\imath}_L\hat{d}-V_o-\hat{v}_0}{R_oC_o}\ . \tag{2.18}$$

Equation (2.18) can be defined as the sum of two voltage sources, so it can be rewritten as:

$$0=\frac{d\langle V_o\rangle}{dt}=\frac{I_LR_oD'-V_o}{R_oC_o}\ , \tag{2.19}$$

$$\frac{d\langle \hat{v}_0\rangle}{dt}=\frac{-I_LR_o\hat{d}+R_oD'\hat{\imath}_L-R_o\hat{\imath}_L\hat{d}-\hat{v}_0}{R_oC_o}\ . \tag{2.20}$$

Then, the converter operating points can be extracted from equations (2.15) and (2.19):

$$V_o=\frac{V_{in}}{(1-D)}\ , \tag{2.21}$$

$$I_o=\frac{V_o}{R_o}=I_L(1-D)\ . \tag{2.22}$$

The duty ratio *D* increases with the increase of the voltage step-up ratio, and for applications requiring high-voltage step-up ratio it becomes a challenge to maintain high efficiency with a large duty ratio. Parasitic ringing in practical circuits also induces additional voltage stresses and necessitates the use of switches with high blocking voltage rating, leading to more losses [13]. Introducing a coupled inductor provides a solution to these problems, reducing the necessary duty ratio for a given step-up voltage ratio. It reduces the voltage across the switch as well, making a coupled-inductor boost converter

more efficient than the conventional boost converter, when a proper inductor design is applied.

2.2 COUPLED INDUCTOR CONCEPT

The construction and principle of a coupled inductor is very simple, as shown in Figure 2.4: two wires are wound around the magnetic core in opposite directions and, due to Lenz's law, produce the same voltage polarity [14].

Figure 2.4 - Two coils magnetically coupled, wound around a magnetic core.

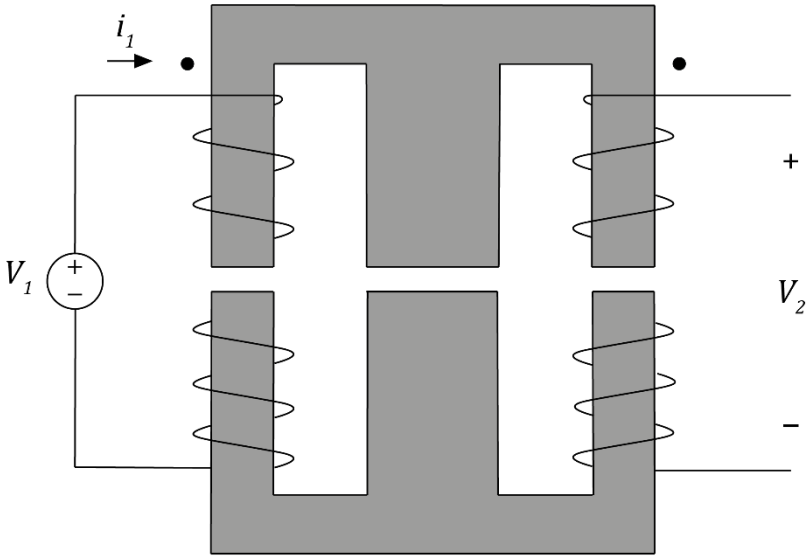

Source: Elaborated by the author.

This component is quite similar to a transformer, however, while the transformer has the main objective of transferring power, the coupled inductor has the purpose of storing energy. A variable magnetic field, generated by the current flowing in the main coil, will induce a current in the opposite direction in the coupled coil. A dot notation is used to specify the direction of windings around the core - points at the same ends of the coupled inductor (Figure 2.4) mean that the coils are wound in the direction of each other. But if the dots are on opposite sides the coils will be wound in the same directions (either clockwise or counterclockwise). Coupled inductors have become popular elements in research of dc-dc converters. The possibility of adjusting the static gain by the turns ratio of the coupled inductor, the requirement of low-voltage switching devices, and the opportunity to recycle the energy stored in the leakage inductor, or using it to provide

soft-switching features in some semiconductor devices, are commonly mentioned advantages of these converts in the literature [15].

But the use of couple inductor technique also has its limitations: even if the static gain can be adjusted by the turns ratio and, in theory, this ratio could be as high as desired, its increase implies an increase in the voltage on the output diode. This voltage increase can make the construction of the magnetic device unfeasible due to its constructive aspects. Furthermore, with this type of technique, the input current becomes discontinuous, requiring the use of input filters in some applications, such as photovoltaic systems. Another very relevant disadvantage of coupled inductor is the fact that its leakage inductance causes loss of duty cycle and resonates with the parasitic capacitance of the output diode after the on-state switch, making it necessary to add a clamp circuit to limit the reverse voltage on this diode [8].

A coupled inductor can be ideally modeled in the same way as an ideal transformer, except for the secondary winding current direction, since in this component the magnetizing current i_{Lm} is equal to the primary winding current i_1 plus the reflected secondary winding current i_2 to the primary, as stated in:

$$i_{Lm} = i_1 + ni_2, \tag{2.23}$$

in which n is the transformation ratio stated as:

$$n = \sqrt{L_2/L_1}. \tag{2.24}$$

The ideal electrical model of coupled inductor is shown in Figure 2.5. Due to the existing magnetic coupling between inductors L_1 and L_2 that share the same core and form the coupled inductor, the voltages in the windings are also directly related by the transformation ratio:

$$v_{L2} = nv_{L1} \tag{2.25}$$

Figure 2.5 – Coupled-inductor equivalent: ideal electrical model.

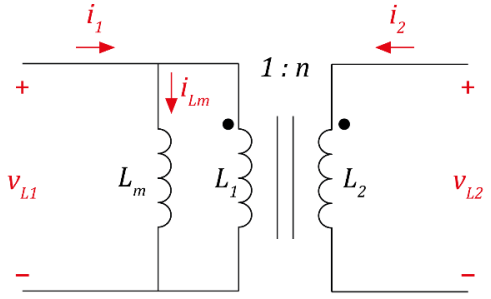

Source: Elaborated by the author.

Coupled inductors can be represented by voltage or current dependent sources. By the principle of power conservation, considering (2.25), it can be determined that $i_1 = ni_2$. Therefore, the coupled inductor can be modeled as illustrated in Figure 2.6, where n is the turns ratio from the primary to the secondary side and is calculated as (2.24) or $n = n_2/n_1$, and considering the leakage inductance much smaller than the magnetizing inductance, neglecting it.

Figure 2.6 – Coupled-inductor equivalent: dependent-source model.

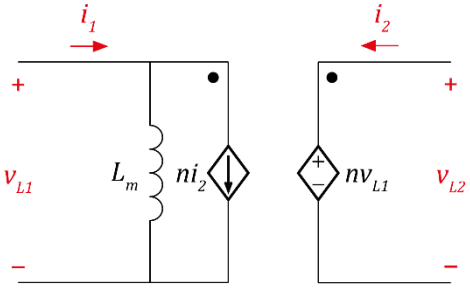

Source: Elaborated by the author.

2.3 VOLTAGE MULTIPLIER CELLS

In addition to the use of coupled inductors, there are also numerous structures that employ capacitors combined with diodes, characterizing voltage multiplier cells [8]. In these cases, the voltage conversion ratio depends on the circuit configuration as well as the number of cells utilized. The multiplication technique occurs when one or more cells, typically composed of diodes and capacitors, are added to a specific topology in order to increase the voltage boost. An example of this technique is the voltage multiplier cells incorporated into a Boost converter, as shown in Figure 2.7. This structure added only one cell for simplicity in converter analysis, and it comprises an inductor, a diode, and two capacitors. However, it is known that the converter's performance improves with the addition of a higher number of cells. Nevertheless, this leads to a significant increase in the required components, thereby becoming a major drawback of the configuration. This converter is advantageous when compared to the classical Boost converter due to its wide range of duty cycle ratios over which it can efficiently operate. In comparison to other converters, it offers the advantages of having only one switch and lacking magnetic coupling [16].

Figure 2.7 – Boost converter with voltage multiplier cell.

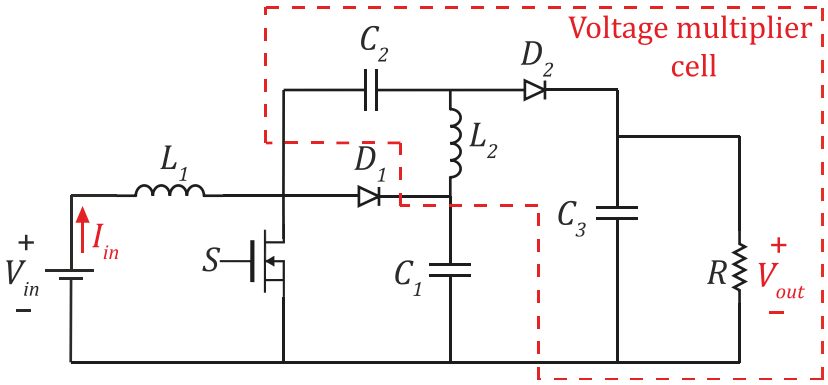

Source: Adapted from [16].

2.4 GAIN CELLS: INTEGRATION OF COUPLE INDUCTORS AND VOLTAGE MULTIPLIERS

According to [3], to meet the need for high values of transformation ratio in applications that demand high static gain, the use of techniques as cascading and voltage multipliers with coupled inductors has become frequent, with voltage multipliers having the advantage of eliminating the need for a voltage clamp on the output diode. In the voltage multiplier technique alone, the output voltage can be increased indefinitely by increasing the number of capacitor-diode pairs, but the converters then require a very high number of components, which implies an increase in cost and a reduction in efficiency.

The integration of voltage multipliers with coupled inductors provides new characteristics, keeping some of its original features and increasing the overall efficiency. As mentioned in Chapter 1, one of the advantages of this technique is the possibility of recycling the energy stored in the leakage inductor, a fact that allows increasing efficiency and avoiding overvoltage in active switches. Each converter to be studied is composed of a Boost converter, a gain cell and an output filter, as shown in Figure 2.8.

Figure 2.8 – Generalization of boost converters with gain cell.

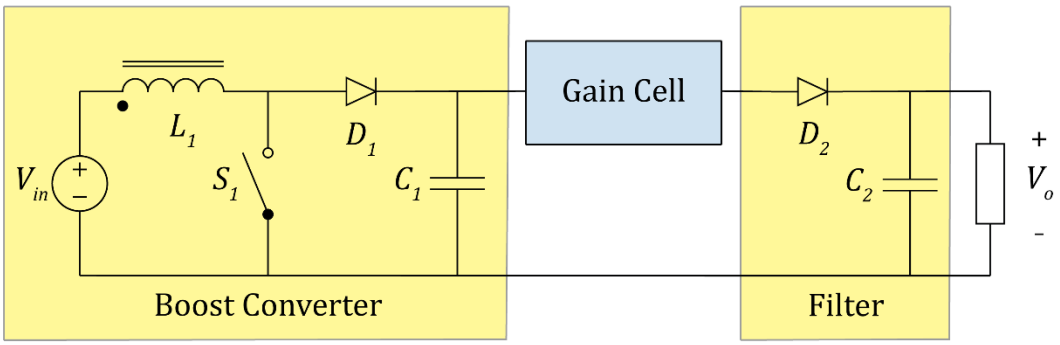

Source: Adapted from [3].

In gain cells, the secondary winding is joined to voltage multiplier circuits, which can generate high DC voltages from AC voltages. Therefore, due to (2.25), it is necessary that the voltage applied to the primary winding be alternated so that the voltage multiplication is carried out. Such a condition is naturally fulfilled by the operation of the conventional Boost converter.

2.5 HIGH STEP-UP BOOST-BASED CONVERTERS WITH GAIN CELLS: TOPOLOGICAL VARIATIONS

All topological variations of boost converters with gain cells have the same operating principle: static gain and external characteristics differing only in some figures of merit, such as input current and voltage and current in the capacitors [3]. In the following sections, the common aspects among the explored topological variations will be initially studied and, only afterwards, the peculiarities of each one will be analyzed.

The topologies that will be addressed in this study are illustrated in Figure 2.9. The variation of the topologies occurs due to the change of the gain cells, responsible for providing additional voltage gain to the Boost converter, as previously discussed, allowing to characterize it as a high-gain topology.

Figure 2.9 - Standard topological variations of dc-dc converters based on the Boost converter highlighting the adopted gain cells. (a) Ideal GC-I Converter; (b) Ideal GC-III Converter; (c) Ideal GC-V Converter.

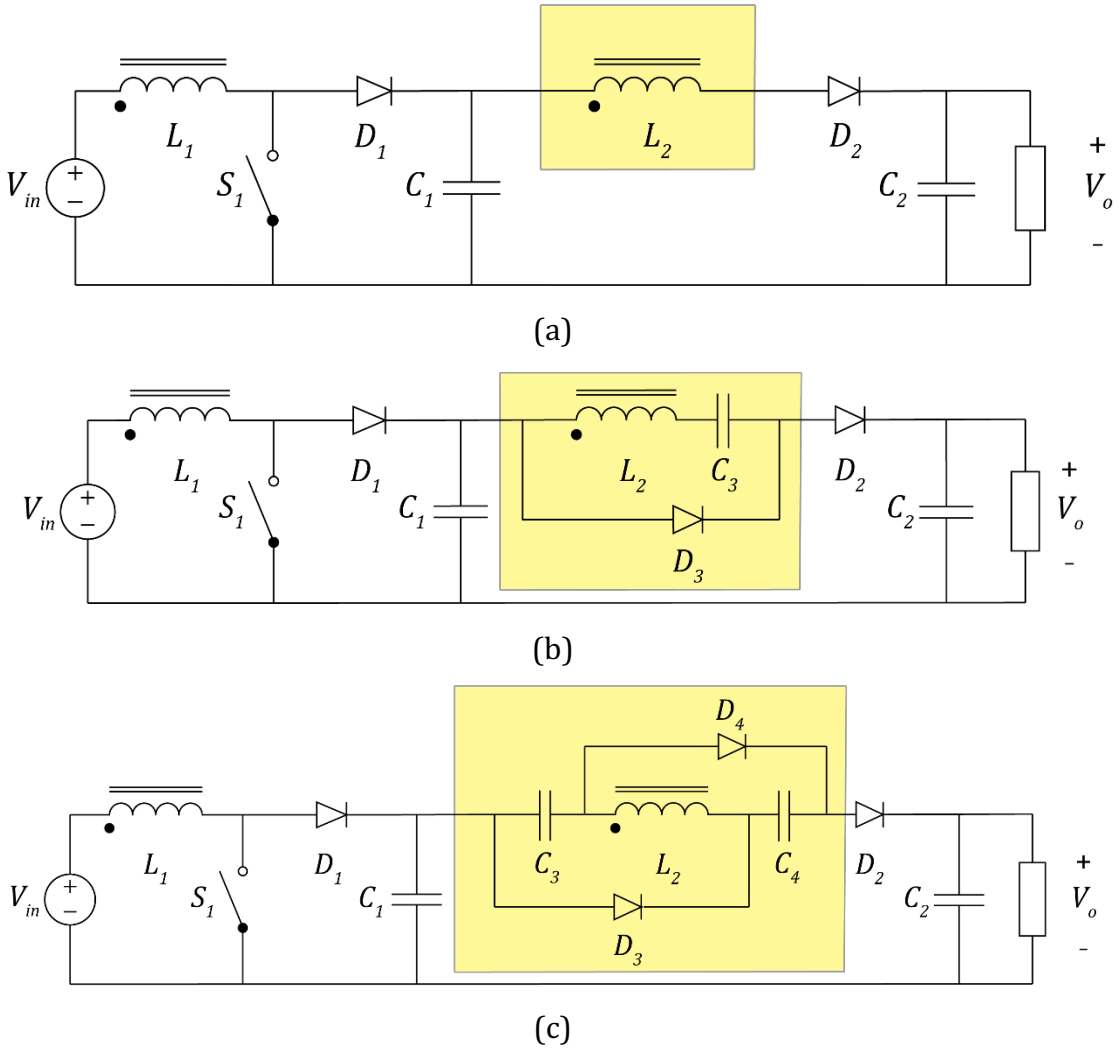

Source: Elaborated by the author.

The first converter, illustrated in Figure 2.9(a), consists of only one coupled inductor as a gain cell, without voltage multipliers. Such a cell is identified as Gain Cell I, the simplest configuration among the studied topologies. Figure 2.9(b) and Figure 2.9(c) show the Boost converter with Gain Cell III and Gain Cell V, respectively – in addition to the coupled inductor, voltage multiplier cells are used in these circuits: one cell in (b) and two cells in (c). As previously mentioned, this terminology (GC-I, GC-III and GC-V) was kept from [3]. These circuit models will be refined in the next chapter to account loss elements.

2.5.1 IDEAL GC-I CONVERTER

Modelling the circuits as ideal converters and using techniques to simplify their equations are an easy way to start the proposed study. For example, taking the converter of Figure 2.9(a) as the first circuit to be modelled, and substituting the Gain Cell I (GC-I) coupled inductor by its dependent-source model as shown in Figure 2.6(b), then the converter is now represented as the Figure 2.10. The operation stages for this converter are analyzed as follows.

Figure 2.10 - Boost converter with GC-I equivalent.

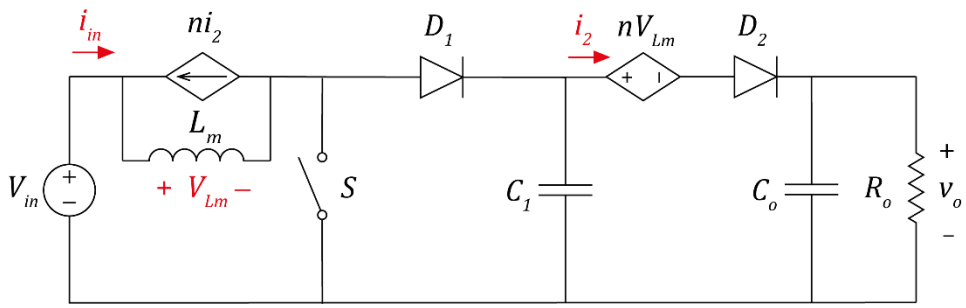

Source: Elaborated by the author.

1st Operating Stage

Over this stage, the switch S is turned ON, so the current in the magnetizing inductance L_m grows linearly as:

$$i_{L_m}(t) = i_{L_m}(t_0) + \frac{V_{in}}{L_m}(t - t_0). \tag{2.26}$$

As the the diode D_1 anode-cathode voltage is negative, it remains reverse biased and therefore blocked. Furthermore, due to the point-to-point configuration of the coupled inductor, the voltage across D_2 is also negative, so it also becomes reverse biased. This operating stage, which duration is DT, is represented in Figure 2.11. This stage ends when the power switch is turned off.

Figure 2.11 - First operating stage equivalent circuit.

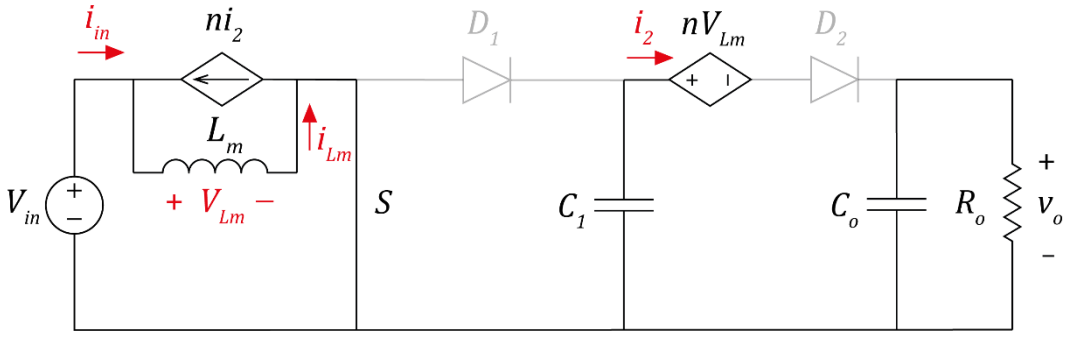

Source: Elaborated by the author.

2nd Operating Stage

When switch S blocks, the energy stored in L_m is transferred to the secondary winding of the coupled inductor, in a way that the diode D_2 becomes forward biased, enabling the transfer of this energy to the load ($R_o C_o$), as shown in Figure 2.12. The diode D_2 conduction allows the capacitor C_1 also delivering energy to the load, discharging itself briefly. However, the voltage drop across the terminals of C_1 directly polarizes the diode D_1, ending this operating stage.

Figure 2.12 - Second operating stage equivalent circuit.

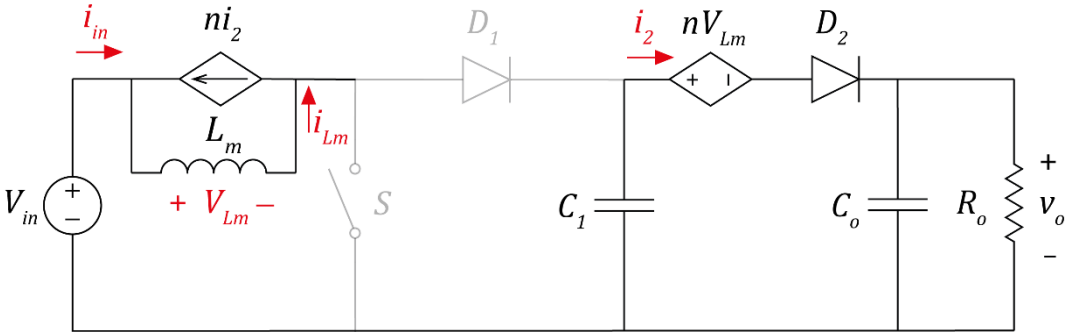

Source: Elaborated by the author.

3rd Operating Stage

When diode D_1 starts conducting, the third stage begins, in which there is the transfer of the energy stored in L_m and from the source V_{in} to the capacitor C_1 and to the load. The equivalent circuit of this stage is shown in Figure 2.13.

Figure 2.13 - Third operating stage equivalent circuit.

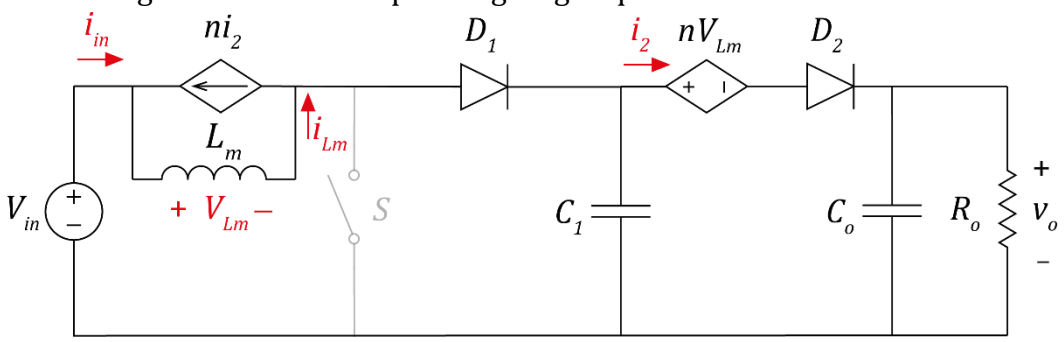

Source: Elaborated by the author.

Some simplifications, as already mentioned, will be considered to obtain simple but relatively accurate models of the ideal converters. In summary, the effect of leakage inductance will be disregarded at first, and the ideal transformer will be replaced by controlled current and voltage sources (coupled inductor dependent-source model shown before). Such simplifications will make each converter present only two operating stages (1st and 3rd), facilitating the obtainment of the referred models [3].

Converter Modeling

In [11] a simplification technique is proposed in which the capacitor C_1 is considered large enough because its voltage remains practically constant over a switching period. This assumption is acceptable as long as the voltage excursion across C_1 over a switching period is sufficiently small, making the duration of the 2nd stage negligible. Then, in [11] was proposed replacing C_1 by a constant voltage source, whose value is equivalent to the average value of the voltage applied to this element, given by:

$$V_{C_1} = \frac{1}{1-D} V_{in} \,, \tag{2.27}$$

where V_{in} is the input voltage and D is the duty cycle at the operating point. Thus, the ideal equivalent circuit of the first stage is now represented by the circuit in Figure 2.14 (a), and its duration is defined by DT. Therefore, the stage has the ideal equivalent circuit shown in Figure 2.14 (b), whose duration interval is equal to $(1 - D)T$.

Figure 2.14 - GC-I Equivalent circuit: (a) 1st Operating stage; (b) 2nd Operating stage.

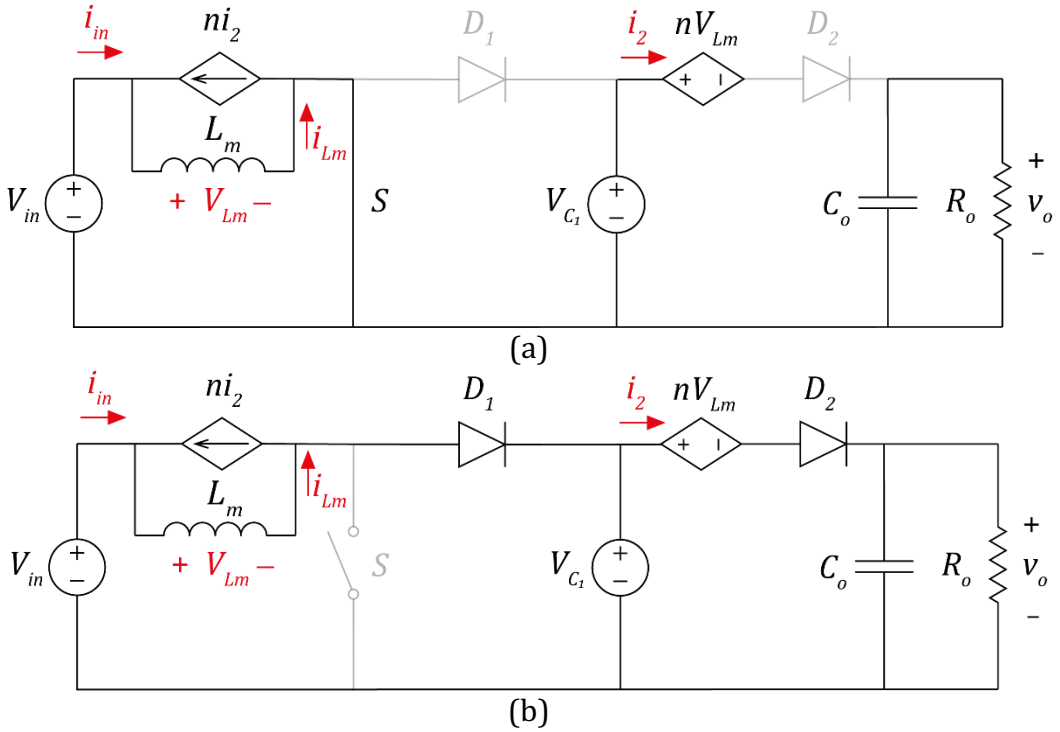

Source: Elaborated by the author.

In the first operating stage, switch S is turned on and diodes D_1 and D_2 are blocked. The equivalent circuit of this stage is shown in Figure 2.14 (a) and its operating range is DT. Through the analysis of the equivalent circuit, it can be obtained:

$$V_{L_m} = V_{in}\,, \tag{2.28}$$

$$i_{C_o} = -\frac{v_o}{R_o}\,. \tag{2.29}$$

Furthermore, it can be stated that the current i_2 is zero in this step and since the input current i_{in} is equal to the sum of the magnetizing inductor current of the controlled current source, i_{L_m} and ni_2, respectively, (2.31) is obtained.

$$i_{in} = i_{L_m} + ni_2\,, \tag{2.30}$$

$$i_{in} = i_{L_m}\,. \tag{2.31}$$

By deriving equations (2.28) and (2.29), one can obtain the voltage state equations for V_{Lm} and the current i_{C_o}:

$$\frac{di_{L_m}}{dt} = \frac{V_{in}}{L_m}\,, \tag{2.32}$$

$$\frac{dv_o}{dt} = -\frac{v_o}{R_o C_o}. \tag{2.33}$$

In the second operating stage, diodes D_1 and D_2 start conducting and switch S is turned off, so it does not conduct current. The equivalent circuit of this stage is shown in Figure 2.14(b). Analyzing the 2nd stage equivalent circuit, it is possible to apply Kirchhoff's laws in the available loops:

$$-V_{in} + V_{L_m} + V_{C_1} = 0\,, \tag{2.34}$$

$$-V_{C_1} + nV_{L_m} + v_o = 0\,. \tag{2.35}$$

Isolating V_{C_1} from (2.34) and substituting in (2.35) results in:

$$V_{L_m} = \frac{V_{in} - v_o}{(1+n)}. \tag{2.36}$$

Applying Kirchhoff's node law:

$$i_{C_o} = i_2 - \frac{v_o}{R_o}. \tag{2.37}$$

From (2.36) and (2.37), (2.39) and (2.40) are achieved, respectively:

$$\frac{di_{L_m}}{dt} = \frac{V_{in} - v_o}{L_m(1+n)}\,, \tag{2.39}$$

$$\frac{dv_o}{dt} = \frac{i_{L_m}}{C_o(1+n)} - \frac{v_o}{R_o C_o}. \tag{2.40}$$

With the state equations, the quasi-instantaneous average values of the quantities of interest in a switching period can be calculated. Thus, carrying out the weighting according to the operating time of each stage, one obtains, respectively:

$$\frac{d\langle i_{L_m}\rangle}{dt} = \frac{\langle v_{in}\rangle . d}{L_m} + \frac{(\langle v_{in}\rangle - \langle v_o\rangle)d'}{L_m(1+n)}, \tag{2.41}$$

$$\frac{d\langle v_o\rangle}{dt} = -\frac{\langle v_o\rangle . d}{R_o C_o} + \left[\frac{\langle i_{L_m}\rangle . d'}{C_o(1+n)} - \frac{\langle v_o\rangle . d'}{R_o C_o}\right], \tag{2.42}$$

where $d' = 1 - d$. Simplifying these equations:

$$\frac{d\langle i_{L_m}\rangle}{dt} = \frac{\langle v_{in}\rangle(1+nd) - \langle v_o\rangle d'}{L_m(1+n)}\,, \tag{2.43}$$

$$\frac{d\langle v_o\rangle}{dt} = \frac{\langle i_{L_m}\rangle}{C_o(1+n)} . d' - \frac{\langle v_o\rangle}{R_o C_o}\,. \tag{2.44}$$

Knowing that the average equations obtained are the result of the product of magnitudes that vary over time, the models extracted from them are non-linear. Thus, since the Laplace Transform must be applied to obtain the transfer functions, it is necessary to linearize the system by applying small perturbations at the operating point of the quantities of interest:

$$\langle i_{L_m} \rangle = I_{L_m} + \hat{\imath}_{L_m}, \tag{2.46}$$

$$\langle v_o \rangle = V_o + \hat{v}_o, \tag{2.47}$$

$$\langle v_{in} \rangle = V_{in} + \hat{v}_{in}, \tag{2.48}$$

$$\langle d \rangle = D + \hat{d}, \tag{2.49}$$

$$\langle d' \rangle = D' - \hat{d}. \tag{2.50}$$

The perturbation $\hat{v}_{in}$ of (2.48) is null because the voltage source V_{in} is constant, then it does not change as a function of time, therefore, it is not necessary to represent a perturbation for this quantity. Inserting the perturbations (2.46), (2.47), (2.49), and (2.50) in (2.43), results in:

$$\frac{d\langle I_{L_m}+\hat{\imath}_{L_m}\rangle}{dt} = \frac{V_{in}\left(1+nD+n\hat{d}\right)-(V_o+\hat{v}_o)(D\prime+\hat{d})}{L_m(1+n)} . \tag{2.51}$$

Rearranging it and simplifying each term, (2.52) is obtained:

$$\frac{d\langle I_{L_m}\rangle}{dt} + \frac{d\langle \hat{\imath}_{L_m}\rangle}{dt} = \frac{V_{in}(1+nD)-V_oD'+(nV_{in}+V_o)\hat{d}-D'\hat{v}_o+\hat{v}_o\hat{d}}{L_m(1+n)} . \tag{2.52}$$

The second-order term in (2.52) can be neglected, as it tends to a very small value, since the perturbations are considered significantly small compared to the respective values of the magnitudes at the operating point, then:

$$\frac{d\langle I_{L_m}\rangle}{dt} + \frac{d\langle \hat{\imath}_{L_m}\rangle}{dt} = \frac{V_{in}(1+nD)-V_oD'+(nV_{in}+V_o)\hat{d}-D'\hat{v}_o}{L_m(1+n)} . \tag{2.53}$$

Splitting (2.53) in two equations, one of zero order and the other one of first order, it is obtained:

$$\frac{d\langle I_{L_m}\rangle}{dt} = \frac{V_{in}(1+nD)-V_oD'}{L_m(1+n)} = 0 , \tag{2.54}$$

$$\frac{d\langle \hat{\imath}_{L_m} \rangle}{dt} = \frac{(nV_{in}+V_o)\hat{d}-D\prime\hat{v}_o}{L_m(1+n)} \quad . \tag{2.55}$$

Following the same procedures to obtain the equations for v_o, results in the zero and first order equations bellow:

$$\frac{d\langle V_o \rangle}{dt} = \frac{I_{L_m}R_oD\prime-V_o(1+n)}{R_oC_o(1+n)} = 0 \quad , \tag{2.56}$$

$$\frac{d\langle \hat{v}_o \rangle}{dt} = \frac{-I_{L_m}R_o\hat{d}+R_oD\prime\hat{\imath}_{L_m}-\hat{v}_o(1+n)}{R_oC_o(1+n)} \quad . \tag{2.57}$$

From (2.54) and (2.56) it is obtained the converter operation points:

$$V_o = \frac{V_{in}(1+nD)}{(1-D)} \quad , \tag{2.58}$$

$$I_o = \frac{V_o}{R_o} = \frac{I_{L_m}(1-D)}{(1+n)} \quad . \tag{2.59}$$

The desired transfer function to finalize the converter modeling, which relates the output voltage $\hat{v}_o$ with the duty cycle $\hat{d}$, is:

$$G_v(s) = \frac{\hat{v}_o}{\hat{d}} \, . \tag{2.60}$$

Applying the Laplace transform in (2.55) and (2.57) results in:

$$sL_m(1+n)\hat{\imath}_{L_m} = (nV_{in}+V_o)\hat{d} - (1-D)\hat{v}_o \quad , \tag{2.61}$$

$$sR_oC_o(1+n)\hat{v}_o = -I_{L_m}R_o\hat{d} + R_o(1-D)\hat{\imath}_{L_m} - (1+n)\hat{v}_o \, . \tag{2.62}$$

Thus, isolating $\hat{\imath}_{Lm}$ from (2.62) and substituting in (2.61), the transfer function G_{v_I} (s) is obtained:

$$G_{v_I}(s) = \frac{\hat{v}_o}{\hat{d}} = \frac{-\frac{sI_o}{C_o(1-D)} + \frac{(nV_{in}+V_o)(1-D)}{L_mC_o(1+n)^2}}{s^2 + \frac{s}{R_oC_o} + \frac{(1-D)^2}{L_mC_o(1+n)^2}} \quad . \tag{2.63}$$

Where $G_{v_I}(s)$ is the transfer function relating the output voltage $\hat{v}_o$ with the duty cycle $\hat{d}$ for the ideal boost converter with gain cell I. The other two types of ideal gain-cell converters are going to be addressed in the next sections.

2.5.2 IDEAL GC-III CONVERTER

The methodology presented in the previous section can also be applied to the other two converters herein studied. The Boost converter with Gain Cell III (GC-III), is shown in Figure 2.9 (b). Replacing the coupled inductor by its dependent-source model and considering all assumptions previously stated, the circuit in Figure 2.9 (b) can be replaced by the one shown in Figure 2.15.

Figure 2.15 - Boost converter with GC-III equivalent.

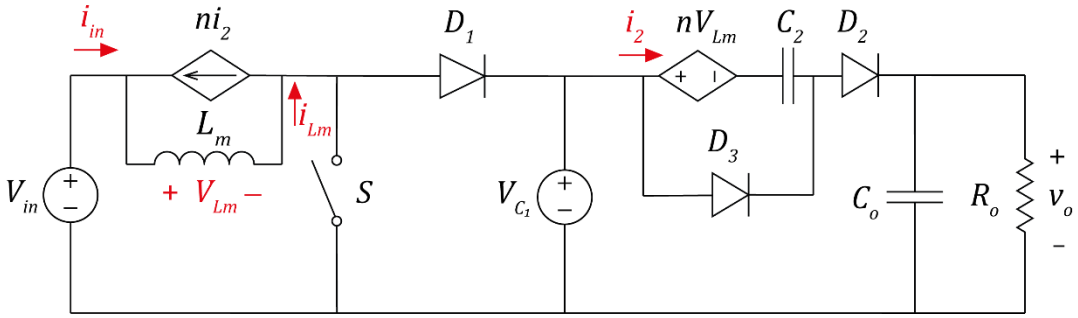

Source: Elaborated by the author.

1st Operating Stage

During this stage, switch S is ON, as well as diode D_3, while diodes D_1 and D_2 are blocked. The equivalent circuit of this operation stage is shown in Figure 2.16(a), and its duration interval is dT. Analyzing the circuit, using Kirchhoff's voltage law, results in:

$$V_{L_m} = V_{in}\,, \tag{2.64}$$

$$nV_{L_m} - V_{C_2} = 0\,. \tag{2.65}$$

Substituting (2.64) in (2.65) obtains:

$$V_{C_2} = nV_{in}\,. \tag{2.66}$$

Deriving (2.64) results in:

$$\frac{di_{L_m}}{dt} = \frac{V_{in}}{L_m}\,. \tag{2.67}$$

2nd Operating Stage

Diodes D_1 and D_2 are switched on in this stage, while switch S and diode D_3 are blocked. The equivalent circuit of this step is shown in Figure 2.16(b) and its duration interval can be approximated by $(1-d)T$. Applying Kirchhoff's law in the loops of the converter 2nd stage equivalent circuit obtains (2.68) and (2.69). Substituting V_{C_2} from (2.66) and V_{C_1} from (2.68) results V_{L_m} as (2.70).

Figure 2.16 - GC-III Equivalent circuit: (a) 1st Operating stage; (b) 2nd Operation stage.

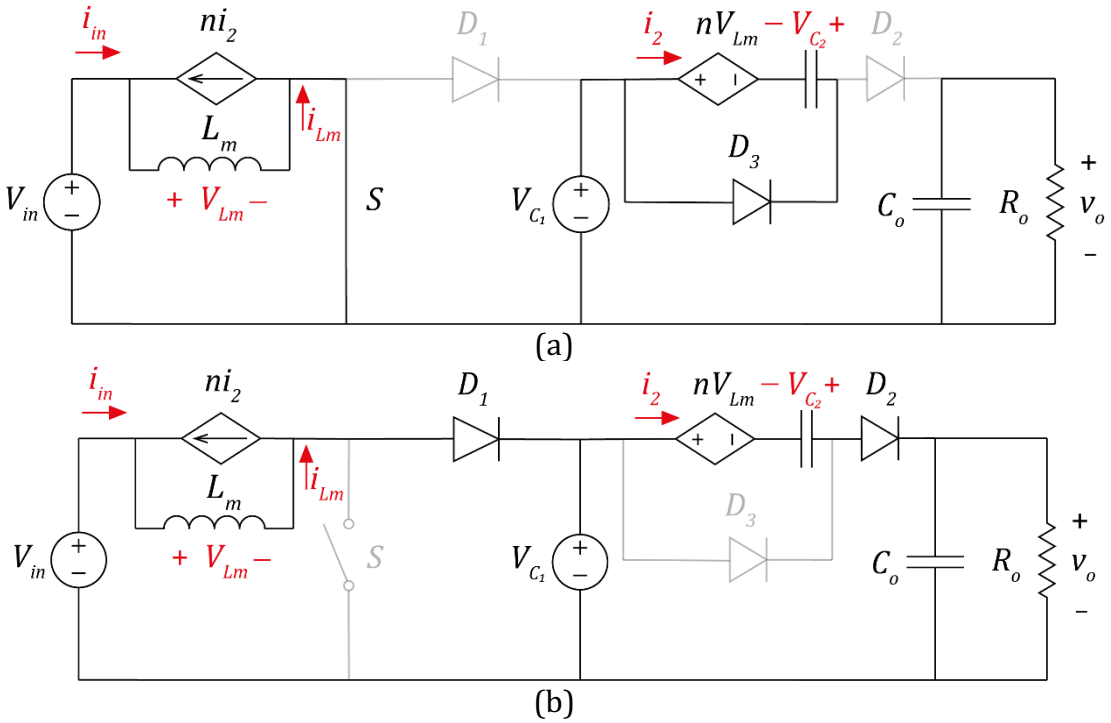

Source: Elaborated by the author.

$$-V_{in} + V_{L_m} + V_{C_1} = 0\,, \tag{2.68}$$

$$-V_{C_1} + nV_{L_m} - V_{C_2} + v_o = 0\,, \tag{2.69}$$

$$V_{L_m} = \frac{V_{in}(1+n) - v_o}{(1+n)}\,. \tag{2.70}$$

Converter Modeling

Deriving (2.70) results in:

$$\frac{di_{L_m}}{dt} = \frac{V_{in}(1+n)-v_o}{L_m(1+n)}. \tag{2.71}$$

Calculating the quasi-instantaneous average value of the derivative of the inductor L_m current, one obtains:

$$\frac{d\langle i_{L_m}\rangle}{dt} = \frac{\langle v_{in}\rangle.d}{L_m} + \frac{(\langle v_{in}\rangle(1+n)-\langle v_o\rangle).d'}{L_m(1+n)}. \tag{2.72}$$

Simplifying this equation results in:

$$\frac{d\langle i_{L_m}\rangle}{dt} = \frac{\langle v_{in}\rangle(1+n)-\langle v_o\rangle d\prime}{L_m(1+n)}. \tag{2.73}$$

Applying the disturbances of (2.46), (2.47), (2.49) and (2.50) in (2.73) to linearize:

$$\frac{d\langle I_{L_m} + \hat{\imath}_{L_m}\rangle}{dt} = \frac{V_{in}(1+n) - (V_o + \hat{v}_o)(D' + \hat{d})}{L_m(1+n)} \tag{2.74}$$

and after simplifying the resulting equation and splitting it in two terms of zero and first orders, one obtain:

$$\frac{d\langle I_{L_m}\rangle}{dt} = \frac{V_{in}(1+n)-V_oD\prime}{L_m(1+n)} = 0, \tag{2.75}$$

$$\frac{d\langle \hat{\imath}_{L_m}\rangle}{dt} = \frac{V_o\hat{d}-D\prime\hat{v}_o}{L_m(1+n)}. \tag{2.76}$$

The procedure realized for the GC-I model is the same followed for the GC-III, resulting in (2.77) and (2.78). With these equations it is possible to obtain the converter operation points with (2.79) and (2.80).

$$\frac{d\langle V_o\rangle}{dt} = \frac{I_{L_m}R_oD\prime-V_o(1+n)}{R_oC_o(1+n)} = 0, \tag{2.77}$$

$$\frac{d\langle \hat{v}_o\rangle}{dt} = \frac{-I_{L_m}R_o\hat{d}+R_oD\prime\hat{\imath}_{L_m}-\hat{v}_o(1+n)}{R_oC_o(1+n)}, \tag{2.78}$$

$$V_o = \frac{V_{in}(1+n)}{(1-D)}, \tag{2.79}$$

$$I_o = \frac{V_o}{R_o} = \frac{I_{L_m}(1-D)}{(1+n)}. \tag{2.80}$$

In this case, the desired transfer function is expressed by (2.60), obtained by applying the Laplace transform in (2.76) and (2.78), obtaining (2.81) and (2.82).

$$sL_m(1+n)\hat{\imath}_{L_m} = V_o\hat{d} - (1-D)\hat{v}_o\,, \tag{2.81}$$

$$sR_oC_o(1+n)\hat{v}_o = -I_{L_m}R_o\hat{d} + R_o(1-D)\hat{\imath}_{L_m} - (1+n)\hat{v}_o\,. \tag{2.82}$$

Isolating $\hat{\imath}_L$ from (2.82) and substituting the result in (2.81), it is obtained:

$$G_{v_{III}}(s) = \frac{\hat{v}_o}{\hat{d}} = \frac{-\dfrac{sI_o}{C_o(1-D)} + \dfrac{V_o(1-D)}{L_mC_o(1+n)^2}}{s^2 + \dfrac{s}{R_oC_o} + \dfrac{(1-D)^2}{L_mC_o(1+n)^2}}. \tag{2.83}$$

Where $G_{v_{III}}(s)$ is the transfer function relating the output voltage $\hat{v}_o$ with the duty cycle $\hat{d}$ for the ideal boost converter with gain cell III.

2.5.3 IDEAL GC-V CONVERTER

The Boost converter with Gain Cell V (GC-V) has a coupled inductor and two voltage multiplier cells in its configuration, as shown in Figure 2.9(c). Representing the coupled inductor as its dependent-source model and considering the same hypothesis of previous sections results in the equivalent circuit of Figure 2.17. As follows, the operating stages of the converter are analyzed, keeping the analysis procedure of the other previously addressed converters.

Figure 2.17 - Boost converter with GC-V equivalent.

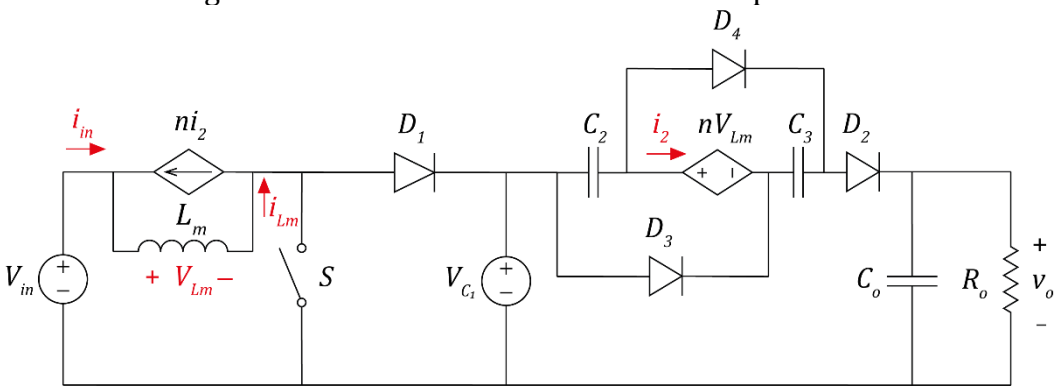

Source: Elaborated by the author.

1st Operating Stage

Switch S is ON, as are diodes D_3 and D_4, while diodes D_1 and D_2 are blocked during this operation stage. Figure 2.18(a) presents the equivalent circuit of this stage, whose operating range is dT, and from its analysis is obtained:

$$V_{L_m} = V_{in}\,, \tag{2.84}$$

$$i_{C_o} = -\frac{v_o}{R_o}. \tag{2.85}$$

Applying Kirchhoff's voltage law over the gain cell, results in (2.86). The equation (2.87) is obtained substituting (2.84) in (2.86).

$$V_{C_2} = V_{C_3} = \mathrm{n}V_{L_m}, \tag{2.86}$$

$$V_{C_2} = V_{C_3} = \mathrm{n}V_{in}. \tag{2.87}$$

Deriving (2.84) results in:

$$\frac{di_{L_m}}{dt} = \frac{V_{in}}{L_m}. \tag{2.88}$$

2nd Operating Stage

During this stage, diodes D_1 and D_2 are switched ON and switch S is turned off, while diodes D_3 and D_4 are also blocked. The equivalent circuit of this operation stage is shown in Figure 2.18(b) and its operating time interval is approximately $(1-d)T$. Analyzing the circuit using Kirchhoff's laws results in:

$$-V_{in} + V_{L_m} + V_{C_1} = 0, \tag{2.89}$$

$$-V_{C_1} - V_{C_2} + nV_{L_m} - V_{C_3} + v_O = 0. \tag{2.90}$$

The voltage V_{L_m} equation represented by (2.91) is obtained replacing V_{C_1} from (2.89) and (2.87) in (2.90) and deriving (2.91) results in (2.92). It is important to keep in mind that the i_{C_o} equation is defined by (2.37).

$$V_{L_m} = \frac{V_{in}(1+2n) - v_O}{(1+n)}, \tag{2.91}$$

$$\frac{di_{L_m}}{dt} = \frac{V_{in}(1+2n) - v_O}{L_m(1+n)}. \tag{2.92}$$

Figure 2.18 - GC-V Equivalent circuit: (a) 1st Operating stage; (b) 2nd Operating stage.

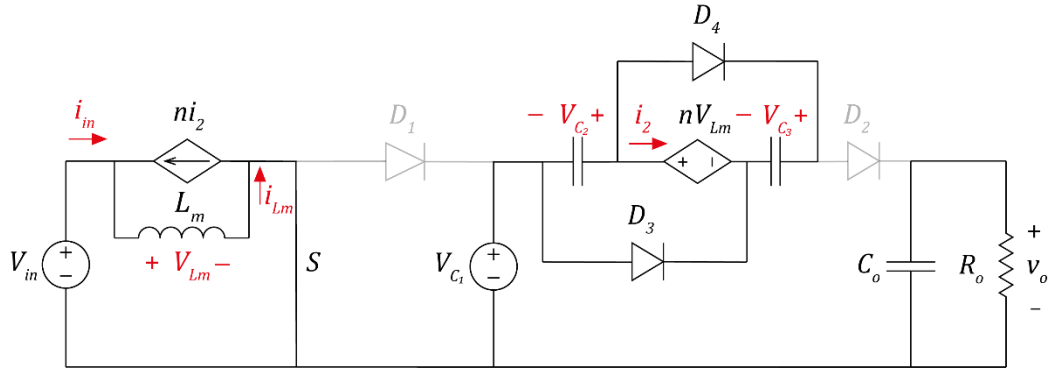

Source: Elaborated by the author.

Converter Modeling

Following the already exposed methodology, the quasi-instantaneous average values of interest are:

$$\frac{d\langle i_{L_m}\rangle}{dt} = \frac{\langle v_{in}\rangle . d}{L_m} + \frac{(\langle v_{in}\rangle(1+2n)-\langle v_o\rangle).d'}{L_m(1+n)}. \tag{2.93}$$

Simplifying (2.93) results in (2.94), and after applying the disturbances of (2.46), (2.47), (2.49), (2.50) in (2.93) and spliting this result in two different terms:

$$\frac{d\langle i_{L_m}\rangle}{dt} = \frac{\langle v_{in}\rangle(1+n+nd\prime)-\langle v_o\rangle d\prime}{L_m(1+n)}, \tag{2.94}$$

$$\frac{d\langle I_{L_m}\rangle}{dt} = \frac{V_{in}(1+n+nD)-V_o D\prime}{L_m(1+n)} = 0, \tag{2.95}$$

$$\frac{d\langle \hat{\imath}_{L_m}\rangle}{dt} = \frac{(V_o - nV_{in})\hat{d} - D\prime\hat{v}_o}{L_m(1+n)}. \tag{2.96}$$

The voltage equations for v_o, (2.97) and (2.98), are obtained following the same methodology previously addressed, and the operation points defined by (2.99) and (2.100) are obtained from (2.95) and (2.97).

$$\frac{d\langle V_o\rangle}{dt} = \frac{I_{Lm}R_oD\prime - V_o(1+n)}{R_oC_o(1+n)} = 0\,, \tag{2.97}$$

$$\frac{d\langle \hat{v}_o\rangle}{dt} = \frac{-I_{Lm}R_o\hat{d} + R_oD\prime\hat{\imath}_{L_1} - \hat{v}_o(1+n)}{R_oC_o(1+n)}\,, \tag{2.98}$$

$$V_o = \frac{V_{in}(1+n+nD)}{(1-D)}\,, \tag{2.99}$$

$$I_o = \frac{V_o}{R_o} = \frac{I_{Lm}(1-D)}{(1+n)}\,. \tag{2.100}$$

The transfer function is expressed by (2.60). It is obtained by applying the Laplace transform in (2.96):

$$sL_1(1+n)\hat{\imath}_{L_1} = (V_o - nV_{in})\hat{d} - (1-D)\hat{v}_o\,. \tag{2.101}$$

Isolating $\hat{\imath}_{L_1}$ from (2.62) and substituting it in (2.101) results in:

$$G_{v_V}(s) = \frac{\hat{v}_o}{\hat{d}} = \frac{-\dfrac{sI_o}{C_o(1-D)} + \dfrac{(V_o - nV_{in})(1-D)}{L_1C_o(1+n)^2}}{s^2 + \dfrac{s}{R_oC_o} + \dfrac{(1-D)^2}{L_1C_o(1+n)^2}}\,, \tag{2.102}$$

where $G_{v_V}(s)$ is the transfer function relating the output voltage $\hat{v}_o$ with the duty cycle $\hat{d}$ for the ideal boost converter with gain cell V.

2.6 CHAPTER CONCLUSIONS

In this chapter, each composing part of high-gain step-up boost converter with coupled inductor gain cell was addressed to conceptualize the elements studied in this thesis. It was not considered any parasitic component, given an overview in an ideal perspective. The modeling of ideal converters with gain cells was addressed through the simplest method and widely discussed in the circuit analysis literature. Next, the parasitic components in dc-dc converters will be introduced, addressing the main types of losses and their effects on dynamic modeling. To conclude this chapter, Figure 2.19 shows the effect of these parasitic elements in the frequency response of the studied converters. As can be noted, adding losses to the converter, as series resistances, affects greatly the damping of the system, but this behavior is not accounted by the ideal model, which will be improved in the next chapter.

Figure 2.19 – Ideal (blue line) *versus* Lossy (red line) Gain-Cell Boost Converters Bode Diagrams: (a) GC-I (b) GC-III (c) GC-V.

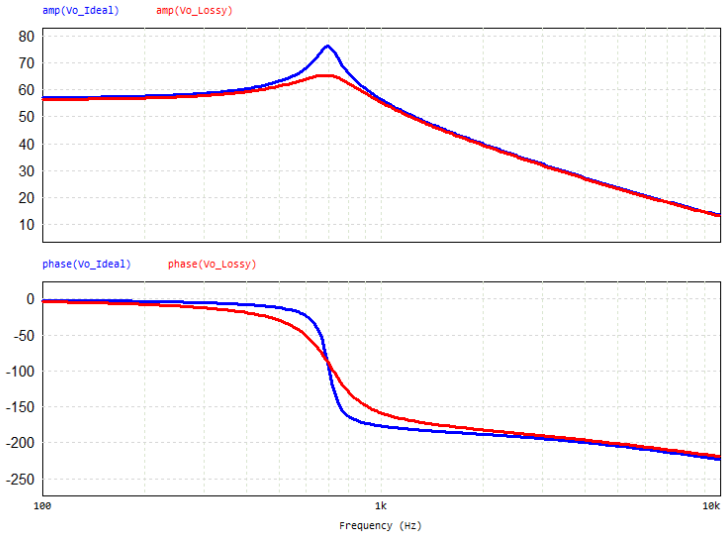

(a)

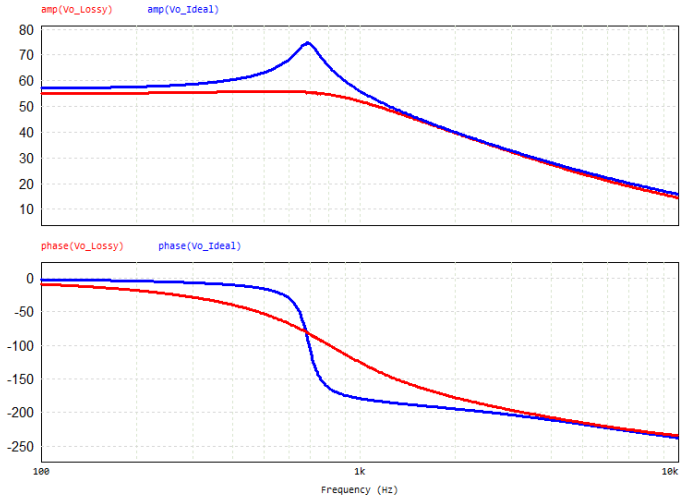

(b)

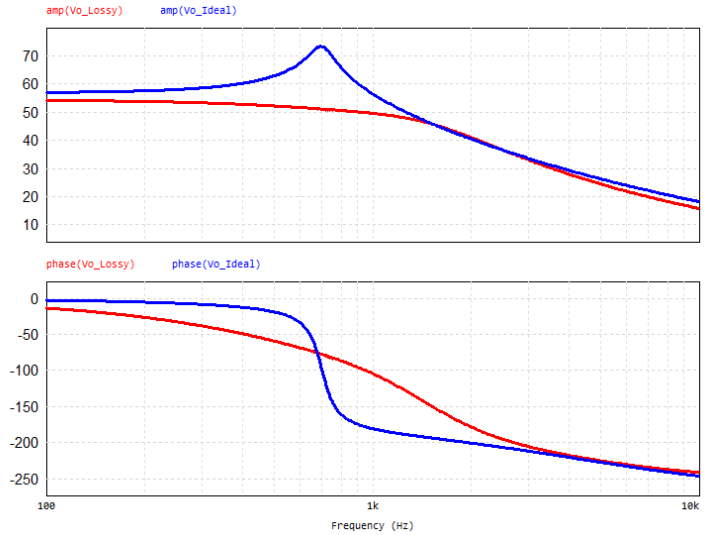

(c)

Source: Elaborated by the author.

3 LOSS MODEL FOR DC-DC CONVERTERS: NON-NEGLIGIBLE PARASITIC COMPONENTS

The performance of a conventional boost converter is limited due to higher on state resistance leading to conduction losses in the switch and diode, losses in the inductor series resistance and the equivalent series resistance (ESR) of the output capacitor. Loss models are widely used to analyze and optimize the power converters before using them into real operation, but commonly the literature addresses only conduction losses, missing, for example, the switching losses, which takes a relevant part in the high frequency system losses [17].

In this work, the adopted loss model includes losses in switches, diodes, coupled inductors and capacitors. These losses are represented as resistive parasitic components while modelling the boost-based converters, and the equations are going to be shown in the next sections of this chapter. Including these loss parameters increase the mathematical effort to represent the converters but it also provides models that are more accurate, making easier to define simpler control strategies leading to a more cost-effective and robust project.

3.1 MOSFET LOSSES

Semiconductor losses in the boost converter are related to switching losses and conduction losses. Therefore, losses in MOSFETs (P_S) can be represented as the following equation, with conduction losses as P_{cond} and switching losses as P_{com}:

$$P_S = P_{cond} + P_{switch} \tag{3.1}$$

3.1.1 CONDUCTION LOSSES

The conduction losses are caused the voltage drops presented at the terminals of the switches during the conduction state. Considering the use of a MOSFET, the conduction losses are given by:

$$P_{cond} = {I_{S1rms}}^2 r_{ds}. \tag{3.2}$$

The resistive component r_{ds} corresponds to the resistance between the drain and source terminals of the switch in operation, and I_{S1rms} represents the switch-current RMS value. For the boost converter, I_{S1rms} is given by:

$$I_{S1rms} = (M-1)I_o, \tag{3.3}$$

which M is the static gain and I_o is the output current of the converter.

3.1.2 SWITCHING LOSSES

The equation commonly used and accepted in the literature to estimate the switching losses in MOSFETs is:

$$P_{switch} = \frac{1}{2} I_{S1p} V_{S1p} \left(t_{on} + t_{off}\right) f_s \tag{3.4}$$

The quantities t_{on} and t_{off} are, respectively, the switching times for entering conduction and blocking. V_{S1p} is the switch voltage and f_s is the switching frequency. Some studies use a simplified version of this equation, as in [8], because the converter operates with *ZVS* (*Zero-Voltage Switching*) when the MOSFET starts conducting, proposing a reduced formula as follows:

$$P_{switch} = \tfrac{1}{2} I_{S1p} V_{S1p} t_{off} f_s. \tag{3.5}$$

The t_{off} time is given by:

$$t_{off} = \frac{Q_{sw}}{I_g}, \tag{3.6}$$

$$I_g = \frac{V_{gs} - V_P}{R_g}. \tag{3.7}$$

The quantity Q_{sw} is the switching gate charge, I_g is the gate current, V_{gs} is the gate-source voltage, V_P is the gate plateau voltage and R_g represents the gate resistor.

3.2 DIODE LOSSES

Diodes can be modeled with reasonable accuracy by a conducting resistance (r_D) in series with a voltage source (v_D), as shown in Figure 3.1.

Figure 3.1 – Diode model including conduction losses.

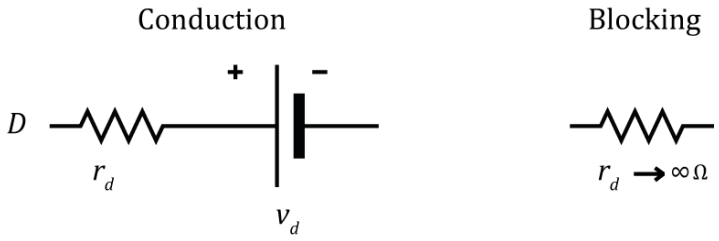

Source: Elaborated by the author.

Diode conduction losses are mathematically represented by:

$$P_D = {I_{Drms}}^2 r_T + I_{Davg} V_T \tag{3.8}$$

In diodes, the transition between the forward and reverse conditions is called recovery. Forward recovery is when a diode goes from the OFF state to the ON state; reverse recovery is when a diode goes from the ON state to the OFF state. These transitions are the switching losses in this kind of semiconductor device. Commonly, forward recovery losses are negligible; but reverse recovery losses can be a non-negligible portion of losses present in diodes in high frequency circuits.

In addition, switching losses are strongly dependent on diode working conditions, reverse voltage, the inductance and a number of external factors, like the active switch and how the switch is driven. Therefore, often a separate analysis is only possible on real circuits, because during the design phase leakage inductances are not well known. Thus, the analysis should be performed mostly on prototypes. In addition, in this type of operation (*Zero-Current Switching* or *ZCS*) the current flowing through the diode during the switching transition is null, so in this particular configuration the switching losses are indeed negligible, because there is no power dissipation when the diode is changing from the ON state to the OFF state or vice-versa.

3.3 CAPACITOR LOSSES

Since the losses related to diodes and switches have already been dealt with in order to estimate the losses associated with each of these components, it is also necessary to deal with the losses of the converter capacitors. This is fundamental to complete the investigation about the efficiency of the converter.

When dealing with capacitors, the main source of losses for this type of application of dc-dc converters is also related to the series resistance of the device (R_{C-ESR}). Thus, average loss related to capacitor series resistance (P_{C-ESR}) can be determined using the regular concept of power dissipation, in which I_{Crms} is the capacitor current rms value, as the following equation:

$$P_{C-ESR} = R_{C-ESR}.{I_{Crms}}^2 \tag{3.9}$$

3.4 COUPLED INDUCTOR LOSSES

Two types of parasitic components can define the inductor losses of the boost converter: the copper losses, due to the wire resistance, and the core losses, due to hysteresis and eddy currents in the magnetic core. Figure 3.2 presents a model for the copper losses of the inductor, showing an ideal inductor L is associated in series with the parasitic resistance r_L.

Figure 3.2 – Inductor model with the cooper losses represented by a parasitic resistance.

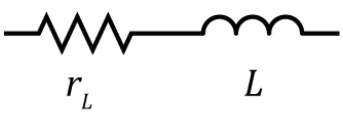

Source: Elaborated by the author.

The core losses can be negligible in this study because they do not represent great influence in the converter dynamics. As this kind of loss is defined mostly by the variation of the magnetic field (ΔB) and, for the type of operation in study, ΔB is constant, the core losses are neglected [8].

In addition, high-gain dc-dc converters with coupled inductor are highly influenced by the leakage inductance. In a physical magnetic device, part of the flux generated by a winding does not flow in the core, being instead dispersed into the air around the winding, and these leakage paths can be represented by leakage inductances. Although it is not particularly a coupled-inductor loss – it causes a duty cycle loss that must be compensated – the leakage inductance adds an extra pole in high frequencies, which barely affects the asymptotes of the Bode diagram, but the damping factor becomes directly dependent on this inductance. As higher its value, greater is the damping of the system [10]. This

relationship between the leakage inductance and damping can also be represented as series resistances, as can be seen in the following section.

3.5 INTERPRETATION OF THE LEAKAGE INDUCTANCE AS AN EXTRA-LOSS ELEMENT

As previously mentioned, the influence of the leakage inductor on the static gain of basic gain-cell converters is commonly neglected. To assess such influence, the approximations illustrated in Figure 3.3, regarding de couple-inductor boost converter, will be considered, since more rigorous analyzes become impractical. Also, more detailed about the operating principle of the Boost converter and its power stage equations are presented in Appendix A and Appendix D, respectively. The transient steps were disregarded, and it was considered that the current in the magnetizing inductor L_m does not present ripple.

As the current ripple in the inductor L_m is zero, it is obtained:

$$I_{Lm} = [M - (a - b)n]I_o = \frac{(1 + bn)}{1 - D} I_o \ , \tag{3.21}$$

where M is the static gain, I_o is the output current, n is the turns ratio, D is the duty cycle, and the parameters a and b are related to the gain cell configuration and were defined in [9], where were performed the static analysis of these converters, assuming different values for each gain cell, as shown in Table 3.1.

Table 3.1 – Parameters a and b each gain cell.

Gain Cell	***a***	***b***
I	0	1
III	1	1
V	2	1

Source: Adapted from [9].

Substituting (3.21) in (D.9):

$$D_x = \frac{2(1 - D)}{(1 + bn)} \ . \tag{3.22}$$

Similarly, substituting (3.21) in (D.14) it is obtained the peak value of the leakage inductor current:

$$I_{Lkp} = \frac{[M - (1 - an)]I_o}{D} \ , \tag{3.23}$$

Figure 3.3 – Approximated voltage and current wave forms for the Boost converter magnetizing inductor L_m and leakage inductor L_k.

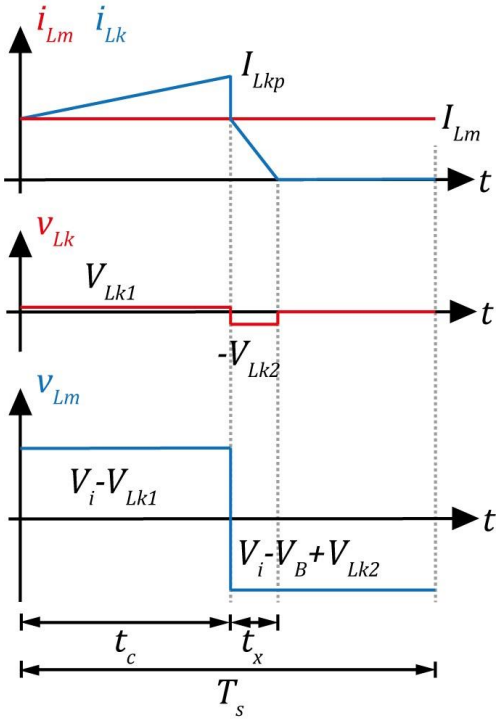

Source: Adapted from [9].

$$I_n = I_{Lm} - \frac{2I_o}{1 - D} \ . \tag{3.24}$$

Accounting the leakage inductor volt-ampere ratio, as seen in Appendix D, it can be found:

$$V_{Lk1} = L_k \frac{(I_{Lkp} - I_{Lm})}{DT} \ , \tag{3.25}$$

$$V_{Lk2} = L_k \frac{I_{Lm}}{D_x T} \ . \tag{3.26}$$

Substituting (3.22), (3.23), and (3.24)) in (3.25) and (3.26):

$$V_{Lk1} = \frac{2an}{D^2} L_k f_s I_o \tag{3.27}$$

$$V_{Lk2} = \frac{(1 + bn)}{2(1 - D)^2} L_k f_s I_o \ . \tag{3.28}$$

According to [9], the output voltage of basic gain cell converters is given by:

$$V_o = V_B + aV_a + bV_b \ . \tag{3.29}$$

For the Boost converter:

$$V_B = \frac{V_i}{1-D} \ , \tag{3.30}$$

$$V_a = n(V_i - V_{Lk1}) \ , \tag{3.31}$$

$$V_b = n(V_B - V_i - V_{Lk2}) \ . \tag{3.32}$$

Substituting (3.27), (3.28), (3.30), (3.31) and (3.32) in (3.29), it is obtained:

$$M = \frac{V_o}{V_i} = \frac{1 + an - (a-b)nD}{1-D} - \frac{L_k I_o}{V_i}\left[2\left(\frac{an}{D}\right)^2 + \frac{bn}{2}\left(\frac{1+bn}{1-D}\right)^2 - \frac{(1+bn)}{(1-D)^2}\right] , \tag{3.33}$$

Or:

$$M = \frac{V_o}{V_i} = \frac{\frac{1 + an - (a-b)nD}{1-D}}{1 + \frac{L_k f_s}{R_o}\left[2\left(\frac{an}{D}\right)^2 + \frac{bn}{2}\left(\frac{1+bn}{1-D}\right)^2 - \frac{(1+bn)}{(1-D)^2}\right]} \ . \tag{3.34}$$

From (3.34) it is comprehensible that the leakage inductance affects the static gain – as higher its value, lower is the converter static gain. As previously mentioned, this inductance also adds an extra pole in high frequencies, which affects directly the damping of the system, increasing the damping as its value increases. Typically, the parasitic resistances are the elements responsible for introducing additional damping in power converters, and since the leakage inductance causes a similar effect in the coupled-inductor converter because of the duty cycle loss, in [10] was proposed the modeling of the leakage inductance effect by means of variable resistances placed in series with the windings of the coupled inductor. The effect of this modeling technique in the converter static gain can be seen in the next section.

3.5.1 MODELING COUPLED-INDUCTOR LEAKAGE INDUCTANCE LOSS EFFECT AS SERIES RESISTANCES

The GC-I Boost converter average model, considering the primary and the secondary coupled-inductor leakage inductance resistances as R_{Lk1} and R_{Lk2}, respectively, is shown in Figure 3.4.

Figure 3.4 – Large-signal average model of GC-I Boost Converter considering the parasitic components R_{Lk1} and R_{Lk2}.

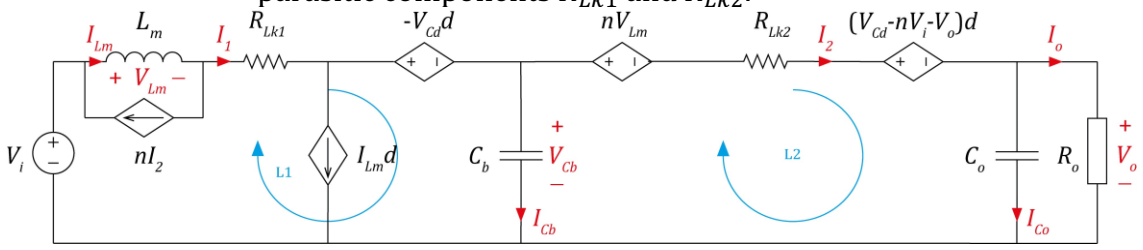

Source: Adapted from [3].

Analyzing the L1 loop, it is concluded that:

$$V_{Cb} = \frac{V_i - I_1 R_{Lk1}}{1 - D} \ . \tag{3.35}$$

From L2 loop, it is noticed that:

$$V_o = V_{Cb} - I_2 R_{Lk2} - nV_{Lm} - D(V_{Cb} - nV_i - V_o) \ . \tag{3.36}$$

Also, it is known that:

$$V_{Lm} = 0 \ , \tag{3.37}$$

$$I_1 = M \frac{V_o}{R_o} \ , \tag{3.38}$$

$$I_2 = \frac{V_o}{R_o} \ . \tag{3.39}$$

Substituting (3.35), (3.37), (3.38) and (3.39) in (3.36):

$$M_{GCI} = \frac{V_o}{V_i} = \frac{\frac{1+nD}{1-D}}{1 + \frac{R_{Lk1}}{R_o}\left[\frac{1+nD}{(1-D)^2}\right] + \frac{R_{Lk2}}{R_o}\left[\frac{1}{(1-D)}\right]} \ . \tag{3.40}$$

Extending the same analysis to the Boost converters with the other gain cells, it can be concluded that the static gain with leakage-inductance losses for GC-III can be expressed by:

$$M_{GCIII} = \frac{V_o}{V_i} = \frac{\frac{1+n}{1-D}}{1 + \frac{R_{Lk1}}{R_o}\left[\frac{1+n}{(1-D)^2}\right] + \frac{R_{Lk2}}{R_o}\left[\frac{1}{(1-D)}\right]} \tag{3.41}$$

Analogously, for GC-V:

$$M_{GCV} = \frac{V_o}{V_i} = \frac{\frac{1+n+nD}{1-D}}{1 + \frac{R_{Lk1}}{R_o}\left[\frac{1+n+nD}{(1-D)^2}\right] + \frac{R_{Lk2}}{R_o}\left[\frac{1}{(1-D)}\right]} \tag{3.42}$$

Generalizing the equation, the generic static gain of the boost converter with gain cell can be mathematically described by:

$$M = \frac{V_o}{V_i} = \frac{\frac{1 + an - (a-b)nD}{1-D}}{1 + \frac{R_{Lk1}}{R_o}\left[\frac{1 + an - (a-b)nD}{(1-D)^2}\right] + \frac{R_{Lk2}}{R_o}\left[\frac{1}{(1-D)}\right]}. \quad (3.43)$$

Therefore, due to the similarity of the expressions, it is possible to equate (3.34) to (3.43), obtaining:

$$R_{Lk1}\left[\frac{1 + an - (a-b)nD}{(1-D)^2}\right] + R_{Lk2}\left[\frac{1}{(1-D)}\right] = L_k f_s\left[2\left(\frac{an}{D}\right)^2 + + \frac{bn}{2}\left(\frac{1+bn}{1-D}\right)^2 - \frac{(1+bn)}{(1-D)^2}\right]. \quad (3.44)$$

Since (3.44) contains two unknown variables (R_{Lk1} and R_{Lk2}) to be determined, two assumptions can be considered:

Assumption 1: Considered losses only in the primary winding and then $R_{Lk2} = 0$

$$R_{Lk1} = \frac{L_k f_s\left[2\left(\frac{an}{D}\right)^2 + \frac{bn}{2}\left(\frac{1+bn}{1-D}\right)^2 - \frac{(1+bn)}{(1-D)^2}\right]}{\left[\frac{1 + an - (a-b)nD}{(1-D)^2}\right]}. \quad (3.45)$$

Assumption 2: Considering losses distributed in both windings and then $R_{Lk2} = n^2 R_{Lk1}$

$$R_{Lk1} = \frac{L_k f_s\left[2\left(\frac{an}{D}\right)^2 + \frac{bn}{2}\left(\frac{1+bn}{1-D}\right)^2 - \frac{(1+bn)}{(1-D)^2}\right]}{\left[\frac{1 + an - (a-b)nD}{(1-D)^2}\right] + n^2\left[\frac{1}{1-D}\right]}. \quad (3.46)$$

In the modeling of lossy converters in the next section, the effect of adding these parasitic resistive components to the circuit loops is demonstrated. It was adopted the assumption of losses in both windings (3.46). It is important to notice that all the couple-inductor losses shown in the previous sections are modeled as equivalent resistors R_1 and R_2 combining the series resistances representing the copper losses and leakage inductance losses. As series resistances, R_1 and R_2 are a sum of their values R_1 for the primary winding, and R_2 for the secondary winding.

3.6 LOSSY BOOST CONVERTER WITH GC-I

In this section, the boost dc–dc converter is a practical converter considering the parasitic elements like ESR and on state voltage drops. In addition, the dependent-source model of coupled inductor seen in the previous chapter is applied, including the loss model resistors R_1 and R_2. An equivalent circuit with all these considerations of the GC-I Boost converter is shown in Figure 3.5. In this analysis was decided to do not account the capacitor as a voltage source, once it is trying to achieve more realistic model. But overall, the modeling approach is similar to the method used in Chapter 2, including the considerations made to analyze the converter operation only over two operating stages, as follows.

Figure 3.5– Circuit diagram of the Lossy GC-I Boost Converter.

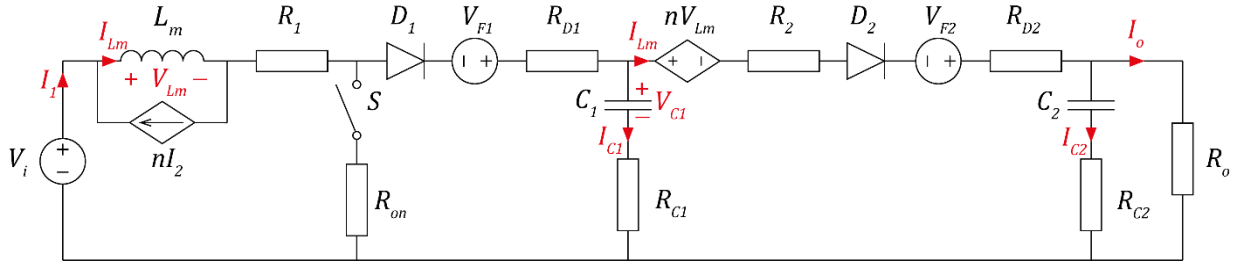

Source: Elaborated by the author.

Figure 3.6 – First operating stage equivalent circuit.

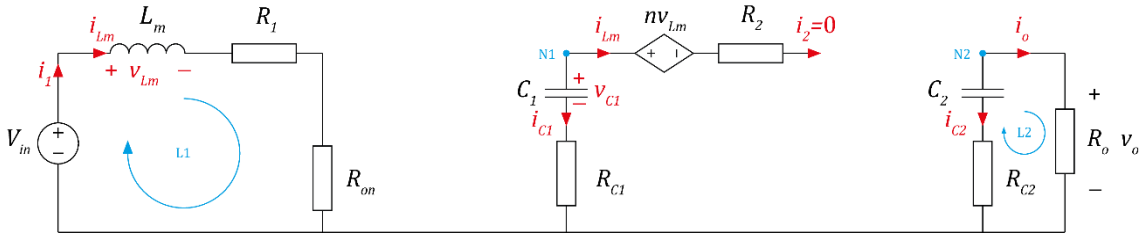

Source: Elaborated by the author.

1st Operating Stage

Over this stage, the switch S is commanded to conduct, and as the diodes D_1 and D_2 anode-cathode voltages are negative, they remain reverse biased and therefore blocked. Applying Kirchhoff's laws in the Figure 3.6 circuit diagram, it is obtained the following equations:

Loop 1 (L1):

$$-V_{in} + v_{Lm} + i_{Lm}(R_1 + R_{on}) = 0\,. \tag{3.47}$$

Node 1 (N1):

$$i_{C1} = 0\,. \tag{3.48}$$

Node 2 (N2)

$$i_{C2} = -\frac{v_o}{R_o}. \tag{3.49}$$

Loop 2 (L2):

$$-\,i_{C2}R_{C2} - v_{C2} + \,v_o = 0\,. \tag{3.50}$$

It is important to notice that during this operating stage, the secondary current i_2 is equals to zero, as shown in the Figure 3.6, and so it is the capacitor C_1 current i_{C1}.

To express the state equations in terms of the inductor current, i_{Lm}, and capacitor voltages, v_{C1} and v_{C2}, requires stating the following definitions:

$$i_{C1} = C_1 \frac{dv_{C1}}{dt}\,, \tag{3.51}$$

$$i_{C2} = C_2 \frac{dv_{C2}}{dt}\,, \tag{3.52}$$

$$v_{Lm} = L_m \frac{di_{Lm}}{dt}\,. \tag{3.53}$$

Therefore, substituting (3.51), (3.52) and (3.53) in equations (3.47), (3.48), (3.49) and (3.50), and solving a linear system with these four equations, results in:

$$\frac{di_{Lm}}{dt} = \frac{(-R_1 - R_{on})i_{Lm} + V_{in}}{L_m}\,, \tag{3.54}$$

$$\frac{dv_{C1}}{dt} = 0\,, \tag{3.55}$$

$$\frac{dv_{C2}}{dt} = -\frac{v_{C2}}{(R_{C2} + R_o)C_2}\,, \tag{3.56}$$

$$v_o = \frac{v_{C2} \cdot R_o}{R_{C2} + R_o}\,. \tag{3.57}$$

2nd Operating Stage

In the 2nd operation stage, diodes D_1 and D_2 start conducting and switch *S* is turned off, so it does not conduct current. The equivalent circuit of this stage is shown in Figure

3.7. Analyzing the 2nd stage equivalent circuit, it is possible to apply the Kirchhoff's laws as previously done in the first stage.

Figure 3.7 – Second operating stage equivalent circuit.

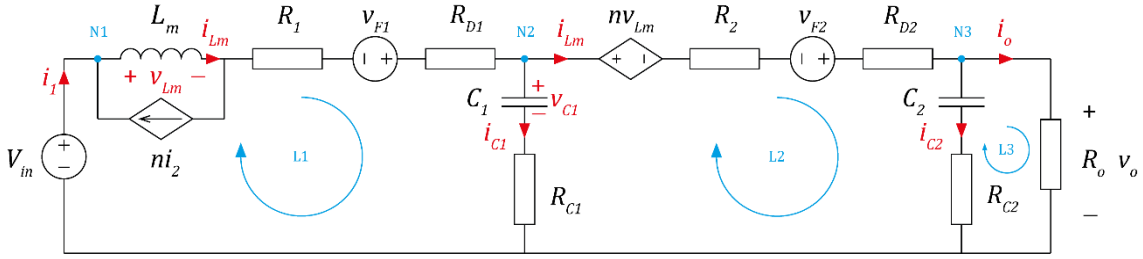

Source: Elaborated by the author.

Loop 1 (L1):

$$-V_{in} + v_{Lm} + i_1(R_1 + R_{D1}) + V_{F1} + v_{C1} + i_{C1}R_{C1} = 0 \tag{3.58}$$

Node 1 (N1): notice that the secondary current i_2 is no longer zero:

$$i_{Lm} - i_1 = ni_2. \tag{3.59}$$

Node 2 (N2):

$$i_{C1} = i_1 - i_2. \tag{3.60}$$

Loop 2 (L2):

$$-i_{C1}R_{C1} - v_{C1} + nv_{Lm} + i_2(R_2 + R_{D2}) + V_{F2} + v_{C2} + i_{C2}R_{C2} = 0. \tag{3.61}$$

Node 3 (N3):

$$i_{C2} = i_2 - \frac{v_o}{R_o}. \tag{3.62}$$

Loop 3 (L3):

$$-i_{C2}R_{C2} - v_{C2} + v_o = 0\,. \tag{3.63}$$

Using the definitions stated in (3.51), (3.52) and (3.53) to solve a linear system with equations (3.58), (3.59), (3.60), (3.61), (3.62) and (3.63), also considering that the diode forward voltages are both equal to each other, $V_{F1} = V_{F2}$=V_{Df}, the second operating stage state equations are:

$$\frac{di_{Lm}}{dt} = ((((-R_{C1}i_{Lm} + (-R_1 - R_{D1})i_{Lm} - V_{Df} + V_{in} - v_{C1})R_{C2} + ((-2V_{Df} + V_{in} - v_{C2})n + (-R_1 - R_2 - R_{D1} - R_{D2})i_{Lm} - 2V_{Df} - 2V_{Df} + V_{in} - v_{C2})R_{C1} - (R_1 + R_{D1})(V_{Df} - v_{C1} + v_{C2})n - (R_2 + R_{D2})((R_1 + R_{D1})i_{Lm} + V_{Df} - V_{in} + v_{C1}))R_o - 2(((V_{Df} - V_{in}/2)n + (R_1/2 + R_2/2 + R_{D1}/2 + R_{D2}/2)i_{Lm} + V_{Df} - V_{in}/2)R_{C1} + ((R_1 + R_{D1})(V_{Df} - v_{C1})n)/2 + ((R_2 + \tag{3.64}$$

$$R_{D2})((R_1 + R_{D1})i_{Lm} + V_{Df} - V_{in} + v_{C1}))/2)R_{C2}))/((((R_{C2} + (n^2 + 2n + 1)R_{C1} + (R_1 + R_{D1})n^2 + R_2 + R_{D2})R_o + ((n+1)^2R_{C1} + (R_1 + R_{D1})n^2R_2 + R_{D2})R_{C2})L_m))$$

$$\frac{dv_{C1}}{dt} = (-(R_{C2} + R_o)(V_{Df} - V_{in} + v_{C1})n^2 + (((-R_1 - R_{D1})i_{Lm} + V_{in} - 2v_{C1} + v_{C2})R_o + R_{C2}((-R_1 - R_{D1})i_{Lm} + V_{in} - 2v_{C1}))n + (i_{Lm}R_{C2} + (R_2 + R_{D2})i_{Lm} + V_{Df} - v_{C1} + v_{C2})R_o + ((R_2 + R_{D2})i_{Lm} + V_{Df} - v_{C1})R_{C2})/(((R_{C2} + R_o)(R_1 + R_{D1} + R_{C1})n^2 + 2R_{C1}(R_{C2} + R_o)n + (R_{C1} + R_2 + R_{C2} + R_{D2})R_o + R_{C2}(R_{C1} + R_2 + R_{D2}))C_1) \tag{3.65}$$

$$\frac{dv_{C1}}{dt} = (((i_{Lm}R_1 + i_{Lm}R_{D1} + i_{Lm}R_{C1} + V_{Df} - V_{in} + v_{C1})n + R_{C1}i_{Lm} - V_{Df} + v_{C1} - v_{C2})R_o - v_{C2}((R_1 + R_{D1} + R_{C1})n^2 + 2R_{C1}n + R_{C1} + R_2 + R_{D2}))/((((R_1 + R_{D1} + R_{C1})n^2 + 2R_{C1}n + R_{C1} + R_2 + R_{C2} + R_{D2})R_o + ((R_1 + R_{D1} + R_{C1})n^2 + 2R_{C1}n + R_{C1} + R_2 + R_{D2})R_{C2})C_2) \tag{3.66}$$

The output voltage during the second operating stage is expressed as:

$$v_o = (R_o(v_{C2}(R_1 + R_{D1} + R_{C1})n^2 + ((i_{Lm}R_1 + i_{Lm}R_{D1} + i_{Lm}R_{C1} + V_{Df} - V_{in} + v_{C1})R_{C2} + 2R_{C1}v_{C2})n + R_{C2}(i_{Lm}R_{C1} - V_{Df} + v_{C1}) + v_{C2}(R_{C1} + R_2 + R_{D2})))/((R_{C2} + R_o)(R_1 + R_{D1} + R_{C1})n^2 + 2R_{C1}(R_{C2} + R_o)n + (R_{C1} + R_2 + R_o + R_{D2})R_{C2} + R_o(R_{C1} + R_2 + R_{D2})) \tag{3.67}$$

The complexity of the equations has increase since the lossy model has more elements to account than the ideal model from Chapter 2. The methodology used in the previous chapter to obtain the average model and the transfer functions is very useful with simpler equations as seen before, but to account so many elements as considered in this model, it could become very complicated to use it. So, it was chosen the state space methodology to deal with the lossy models presented in this study, since this method is widely used in converters modelling. A review about state space averaging technique is presented in Appendix B. Thus, the state equations from the first operating stage, after multiplied by the duty cycle d, can be written as:

$$\frac{d}{dt}\begin{bmatrix} i_{Lm} \\ v_{C1} \\ v_{C2} \end{bmatrix} = \begin{bmatrix} \frac{(-R_1 - R_{on})d}{L_m} & 0 & 0 \\ 0 & 0 & 0 \\ 0 & 0 & -\frac{d}{(R_{C2} + R_o)C_2} \end{bmatrix}\begin{bmatrix} i_{Lm} \\ v_{C1} \\ v_{C2} \end{bmatrix} + \begin{bmatrix} \frac{d}{L_m} & 0 \\ 0 & 0 \\ 0 & 0 \end{bmatrix}\begin{bmatrix} V_{in} \\ V_{Df} \end{bmatrix}, \tag{3.68}$$

$$[v_o] = \begin{bmatrix} 0 & 0 & \dfrac{R_o d}{R_{C2} + R_o} \end{bmatrix} \begin{bmatrix} i_{Lm} \\ v_{C1} \\ v_{C2} \end{bmatrix} + [0 \quad 0] \begin{bmatrix} V_{in} \\ V_{Df} \end{bmatrix}. \tag{3.69}$$

Analogously, the second operating stage equations are multiplied by $(1 - d)$ and rewritten as:

$$\frac{d}{dt} \begin{bmatrix} i_{Lm} \\ v_{C1} \\ v_{C2} \end{bmatrix} = \begin{bmatrix} A & B & C \\ D & E & F \\ G & H & I \end{bmatrix} \begin{bmatrix} i_{Lm} \\ v_{C1} \\ v_{C2} \end{bmatrix} + \begin{bmatrix} J & K \\ L & M \\ N & O \end{bmatrix} \begin{bmatrix} V_{in} \\ V_{Df} \end{bmatrix} \begin{bmatrix} V_{in} \\ V_{Df} \end{bmatrix}, \tag{3.70}$$

$$[v_o] = [P \quad Q \quad R] \begin{bmatrix} i_{Lm} \\ v_{C1} \\ v_{C2} \end{bmatrix} + [S \quad T] \begin{bmatrix} V_{in} \\ V_{Df} \end{bmatrix}, \tag{3.71}$$

Where:

$$A = ((((-R_{C1} - R_1 - R_{D1})R_{C2} + (-R_1 - R_2 - R_{D1} - R_{D2})R_{C1} - (R_1 + R_{D1})(R_2 + R_{D2}))R_o - 2R_{C2}((R_1/2 + R_2/2 + R_{D1}/2 + R_{D2}/2)R_{C1} + ((R_1 + R_{D1})(R_2 + R_{D2}))/2))(1 - d))/(L_m((R_{C2} + (n^2 + 2n + 1)R_{C1} + (R_1 + R_{D1})n^2 + R_2 + R_{D2})R_o + R_{C2}((n + 1)^2 R_{C1} + (R_1 + R_{D1})n^2 + R_2 + R_{D2}))) \tag{3.72}$$

$$B = (((-R_{C2} + (R_1 + R_{D1})n - R_2 - R_{D2})R_o - 2R_{C2}(-((R_1 + R_{D1})n)/2 + R_2/2 + R_{D2}/2))(1 - d))/(L_m((R_{C2} + (n^2 + 2n + 1)R_{C1} + (R_1 + R_{D1})n^2 + R_2 + R_{D2})R_o + R_{C2}((n + 1)^2 R_{C1} + (R_1 + R_{D1})n^2 + R_2 + R_{D2}))) \tag{3.73}$$

$$C = (((-n - 1)R_{C1} - (R_1 + R_{D1})n)R_o(1 - d))/(L_m((R_{C2} + (n^2 + 2n + 1)R_{C1} + (R_1 + R_{D1})n^2 + R_2 + R_{D2})R_o + R_{C2}((n + 1)^2 R_{C1} + (R_1 + R_{D1})n^2 + R_2 + R_{D2}))) \tag{3.74}$$

$$D = ((((-R_1 - R_{D1})R_o + R_{C2}(-R_1 - R_{D1}))n + (R_{C2}(R_2 + R_{D2}))(1 - d))/(C_1((R_{C2} + R_o)(R_1 + R_{D1} + R_{C1})n^2 + 2R_{C1}(R_{C2} + R_o)n + (R_{C1} + R_2 + R_{C2} + R_{D2})R_o + R_{C2}(R_{C1} + R_2 + R_{D2}))) \tag{3.75}$$

$$E = (-(R_{C2} + R_o)n^2 + (-2R_o - 2R_{C2})n - R_o - R_{C2})(1 - d))/(C_1((R_{C2} + R_o)(R_1 + R_{D1} + R_{C1})n^2 + 2R_{C1}(R_{C2} + R_o)n + (R_{C1} + R_2 + R_{C2} + R_{D2})R_o + R_{C2}(R_{C1} + R_2 + R_{D2}))) \tag{3.76}$$

$$F = ((R_o n + R_o)(1 - d))/(C_1((R_{C2} + R_o)(R_1 + R_{D1} + R_{C1})n^2 + 2R_{C1}(R_{C2} + R_o)n + (R_{C1} + R_2 + R_{C2} + R_{D2})R_o + R_{C2}(R_{C1} + R_2 + R_{D2}))) \tag{3.77}$$

$$G = (((R_1 + R_{D1} + R_{C1})n + R_{C1})R_o(1 - d))/(C_2(((R_1 + R_{D1} + R_{C1})n^2 + 2R_{C1}n + R_{C1} + R_2 + R_{C2} + R_{D2})R_o + R_{C2}((R_1 + R_{D1} + R_{C1})n^2 + 2R_{C1}n + R_{C1} + R_2 + R_{D2}))) \tag{3.78}$$

$$H = ((n + 1)R_o(1 - d))/\,)/(C_2(((R_1 + R_{D1} + R_{C1})n^2 + 2R_{C1}n + R_{C1} + R_2 + R_{C2} + R_{D2})R_o + R_{C2}((R_1 + R_{D1} + R_{C1})n^2 + 2R_{C1} + R_{C1} + R_2 + R_{D2}))) \tag{3.79}$$

$$I = \big((-R_o - (R_1 + R_{D1} + R_{C1})n^2 - 2R_{C1}n - R_{C1} - R_2 - R_{D2})(1-d)\big) \\ /(C_2(((R_1 + R_{D1} + R_{C1})n^2 + 2R_{C1}n + R_{C1} + R_2 + R_{C2} + R_{D2})R_o + \\ R_{C2}((R_1 + R_{D1} + R_{C1})n^2 + 2R_{C1} + R_{C1} + R_2 + R_{D2}))) \tag{3.80}$$

$$J = (((R_{C2} + (n+1)R_{C1} + R_2 + R_{D2})R_o - 2R_{C2}((-n/2 - 1/2)R_{C1} - \\ R_2/2 - R_{D2}/2))(1-d))/(L_m((R_{C2} + (n^2 + 2n + 1)R_{C1} + (R_1 + R_{D1})n^2 \\ + R_2 + R_{D2})R_o + R_{C2}((n+1)^2 R_{C1} + (R_1 + R_{D1})n^2 + R_2 + R_{D2}))) \tag{3.81}$$

$$K = (\big((-R_{C2} + (-2n-2)R_{C1} - (R_1 + R_{D1})n - R_2 - R_{D2}\big)R_o - 2R_{C2}((n \\ +1)R_{C1} + ((R_1 + R_{D1})n)/2 + R_2/2 + R_{D2}/2))(1-d))/(L_m((R_{C2} + (n^2 \\ +2n+1)R_{C1} + (R_1 + R_{D1})n^2 + R_2 + R_{D2})R_o + R_{C2}((n+1)^2 R_{C1} + (R_1 + \\ R_{D1})n^2 + R_2 + R_{D2}))) \tag{3.82}$$

$$L = (\big((R_{C2} + R_o)n^2 + (R_{C2} + R_o)n\big)(1-d))/(C_1((R_{C2} + R_o)(R_1 + R_{D1} \\ + R_{C1})n^2 + 2R_{C1}(R_{C2} + R_o)n + (R_{C1} + R_2 + R_{C2} + R_{D2})R_o + R_{C2}(R_{C1} + \\ R_2 + R_{D2}))) \tag{3.83}$$

$$M = ((-(R_{C2} + R_o)n^2 + R_o + R_{C2})(1-d))/(C_1((R_{C2} + R_o)(R_1 + R_{D1} \\ + R_{C1})n^2 + 2R_{C1}(R_{C2} + R_o)n + (R_{C1} + R_2 + R_{C2} + R_{D2})R_o + R_{C2}(R_{C1} + \\ R_2 + R_{D2}))) \tag{3.84}$$

$$N = (nR_o(1-d))/(C_2(((R_1 + R_{D1} + R_{C1})n^2 + 2R_{C1}n + R_{C1} + R_2 + R_{C2} \\ + R_{D2})R_o + R_{C2}((R_1 + R_{D1} + R_{C1})n^2 + 2R_{C1}n + R_{C1} + R_2 + R_{D2}))) \tag{3.85}$$

$$O = ((n-1)R_o(1-d))\ /(C_2(((R_1 + R_{D1} + R_{C1})n^2 + 2R_{C1}n + R_{C1} + R_2 \\ + R_{C2} + R_{D2})R_o + R_{C2}((R_1 + R_{D1} + R_{C1})n^2 + 2R_{C1}n + R_{C1} + R_2 + R_{D2}))) \tag{3.86}$$

$$P = (((R_1 + R_{D1} + R_{C1})R_{C2}n + R_{C2}R_{C1})R_o(1-d))/((R_{C2} + R_o)(R_1 + \\ R_{D1} + R_{C1})n^2 + 2R_{C1}(R_{C2} + R_o)n + (R_{C1} + R_2 + R_o + R_{D2})R_{C2} + \\ R_o(R_{C1} + R_2 + R_{D2}))) \tag{3.87}$$

$$Q = ((R_{C2}n + R_{C2})R_o(1-d))/))/((R_{C2} + R_o)(R_1 + R_{D1} + R_{C1})n^2 + \\ 2R_{C1}(R_{C2} + R_o)n + (R_{C1} + R_2 + R_o + R_{D2})R_{C2} + R_o(R_{C1} + R_2 + R_{D2}))) \tag{3.88}$$

$$R = (((R_1 + R_{D1} + R_{C1})n^2 + 2R_{C1}n + R_{C1} + R_2 + R_{D2})R_o(1-d))/ \\ ((R_{C2} + R_o)(R_1 + R_{D1} + R_{C1})n^2 + 2R_{C1}(R_{C2} + R_o)n + (R_{C1} + R_2 + R_o + \\ R_{D2})R_{C2} + R_o(R_{C1} + R_2 + R_{D2}))) \tag{3.89}$$

$$S = (-R_{C2}nR_o(1-d))/((R_{C2} + R_o)(R_1 + R_{D1} + R_{C1})n^2 + 2R_{C1}(R_{C2} + \\ R_o)n + (R_{C1} + R_2 + R_o + R_{D2})R_{C2} + R_o(R_{C1} + R_2 + R_{D2}))) \tag{3.90}$$

$$T = ((R_{C2}n - R_{C2})R_o(1-d))/((R_{C2} + R_o)(R_1 + R_{D1} + R_{C1})n^2 + \\ 2R_{C1}(R_{C2} + R_o)n + (R_{C1} + R_2 + R_o + R_{D2})R_{C2} + R_o(R_{C1} + R_2 + R_{D2}))). \tag{3.91}$$

Summing and simplifying the matrices from both stages results in the large-signal average model:

$$\frac{d}{dt}\begin{bmatrix}\langle i_{Lm}\rangle\\ \langle v_{C1}\rangle\\ \langle v_{C2}\rangle\end{bmatrix}=\begin{bmatrix}X\\ Y\\ Z\end{bmatrix}, \tag{3.92}$$

Where:

$$X=(((((R_{C1}-R_{on}+R_{D1})\langle i_{Lm}\rangle+V_{Df}+V_{C1})d+(-R_{C1}-R_1)\langle i_{Lm}\rangle- V_{Df}+V_{in}-\langle v_{C1}\rangle)R_{C2}+(-(\langle i_{Lm}\rangle(R_1+R_{on})-V_{in})(R_1+R_{D1}+R_{C1})n^2 +(-2R_{C1}(R_1+R_{on})\langle i_{Lm}\rangle+(2V_{Df}+V_{in}+\langle v_{C2}\rangle)R_{C1}+(R_1+R_{D1})(V_{Df}- \langle v_{C1}\rangle+\langle v_{C2}\rangle))n+((R_{D2}-R_{on}+R_2+R_{D1})R_{C1}-(R_{on}-R_{D1})(R_2+ R_{D2}))\langle i_{Lm}\rangle+(2V_{Df}+\langle v_{C2}\rangle)R_{C1}+(V_{Df}+\langle v_{C1}\rangle)(R_2+R_{D2}))d+(-2V_{Df} +V_{in}-\langle v_{C2}\rangle)R_{C1}-(R_1+R_{D1})(V_{Df}-\langle v_{C1}\rangle+\langle v_{C2}\rangle))n+((-R_1-R_2- R_{D1}-R_{D2})R_{C1}-(R_{on}-R_{D1})(R_2+R_{D2}))\langle i_{Lm}\rangle+(-2V_{Df}+V_{in}- \langle v_{C2}\rangle)R_{C1}-(V_{Df}-V_{in}+\langle v_{C1}\rangle)(R_2+R_{D2})R_o+((-(\langle i_{Lm}\rangle(R_1+R_{on})- V_{in})(R_1+R_{D1}+R_{C1})n^2+(-2R_{C1}(R_1+R_{on})\langle i_{Lm}\rangle+(2V_{Df}+V_{in})R_{C1}+ (R_1+R_{D1})(V_{Df}-\langle v_{C1}\rangle))n+((R_{D2}-R_{on}+R_2+R_{D1})R_{C1}-(R_{on}- R_{D1})(R_2+R_{D2}))\langle i_{Lm}\rangle+2R_{C1}V_{Df}+(V_{Df}+\langle v_{C1}\rangle)(R_2+R_{D2}))d+((V_{in} -2V_{Df})R_{C1}-(R_1+R_{D1})(V_{Df}-\langle v_{C1}\rangle))n+((-R_1-R_2R_{D1}-R_{D2})R_{C1} -(R_1+R_{D1})(R_2+R_{D2}))\langle i_{Lm}\rangle+(V_{in}-2V_{Df})R_{C1}-(V_{Df}-V_{in}+ \langle v_{C1}\rangle)(R_2+R_{D2}))R_{C2})/(L_m(((R_1+R_{D1}+R_{C1})n^2+2R_{C1}n+R_{C1}+R_2+ R_{C2}+R_{D2})R_o+R_{C2}+R_{D2}((R_1+R_{D1}+R_{C1})n^2+2R_{C1}n+R_{C1}+R_2+ R_{D2})) \tag{3.93}$$

$$Y=-((-1+d)(-R_{C2}+R_o)(V_{Df}-V_{in}+\langle v_{C1}\rangle)n^2+(((-R_1- R_{D1})\langle i_{Lm}\rangle+V_{in}-2\langle v_{C1}\rangle+\langle v_{C2}\rangle)R_o+R_{C2}((-R_1-R_{D1})\langle i_{Lm}\rangle+V_{in}- 2\langle v_{C1}\rangle))n+(\langle i_{Lm}\rangle R_{C2}+(R_2+R_{D2})\langle i_{Lm}\rangle+V_{Df}-\langle v_{C1}\rangle+\langle v_{C2}\rangle)R_o+ R_{C2}((R_2+R_{D2})\langle i_{Lm}\rangle+V_{Df}-\langle v_{C1}\rangle)))/(C_1((R_{C2}+R_o)(R_1+R_{D1}+ R_{C1})n^2+2R_{C1}(R_{C2}+R_o)n+(R_{C1}+R_2+R_{C2}+R_{D2})R_o+ R_{C2}(R_{C1}+R_2+R_{D2}))) \tag{3.94}$$

$$Z=(-((R_{C1}\langle i_{Lm}\rangle+(R_1+R_{D1})\langle i_{Lm}\rangle-V_{in}+\langle v_{C1}\rangle+V_{Df})n+R_{C1}\langle i_{Lm}\rangle- V_{Df}+\langle v_{C1}\rangle-\langle v_{C2}\rangle)(-1+d){R_o}^2+(-\langle v_{C2}\rangle(R_1+R_{D1}+R_{C1})n^2+(- (-1+d)\big(R_{C1}\langle i_{Lm}\rangle+(R_1+R_{D1})\langle i_{Lm}\rangle-V_{in}+\langle v_{C1}\rangle+V_{Df}\big)R_{C2}- 2R_{C1}\langle v_{C2}\rangle)n+(-\langle i_{Lm}\rangle(-1+d)R_{C1}+(V_{Df}-\langle v_{C1}\rangle)d-V_{Df}+\langle v_{C1}\rangle- \langle v_{C2}\rangle)R_{C2}-\langle v_{C2}\rangle(R_{C1}+R_2+R_{D2}))R_o-((R_1+R_{D1}+R_{C1})n^2+2R_{C1}n+ R_{C1}+R_2+R_{D2})R_{C2}\langle v_{C2}\rangle)/((R_{C2}+R_o)(C_2(((R_1+R_{D1}+R_{C1})n^2+2R_{C1}n +R_{C1}+R_2+R_{C2}+R_{D2})R_o+R_{C2}((R_1+R_{D1}+R_{C1})n^2+2R_{C1}n+R_{C1}+ R_2+R_{D2}))). \tag{3.95}$$

The models extracted from the average equations are non-linear, since they are obtained as a result of the product of magnitudes that vary over time. As seen previously, it is necessary to linearize the system to obtain the transfer functions. In Chapter 2 the linearization was achieved through the perturbation technique, very useful with smaller models. Since this model deals with much longer equations, the Expanded Taylor Series

technique was chosen to linearize this model, and a brief review about this methodology is presented in Appendix C.

Using Taylor Series to obtain the small-signal model of this converter, first it takes (3.93), (3.94) and (3.95) as vector-valued functions obtained from the large-signal average model. Using these vector-valued functions, it is possible to obtain the Jacobian matrices $A_J$and B_J:

$$\boldsymbol{A_J} = \begin{bmatrix} Aaj & Baj & Caj \\ Daj & Eaj & Faj \\ Gaj & Haj & Iaj \end{bmatrix}, \tag{3.96}$$

$$\boldsymbol{B_J} = \begin{bmatrix} Abj & Bbj & Cbj \\ Dbj & Ebj & Fbj \\ Gbj & Hbj & Ibj \end{bmatrix}, \tag{3.97}$$

where:

$$Aaj = ((((R_{C1} - R_{on} + R_{D1})d - R_{C1} - R_1 - R_{D1})R_{C2} + (-(R_1 + R_{on})(R_1 + R_{D1} + R_{C1})n^2 - 2R_{C1}(R_1 + R_{on})n + (R_{D2} - R_{on} + R_2 + R_{D1})R_{C1} - (R_{on} - R_{D1})(R_2 + R_{D2}))d + (-R_1 - R_2 - R_{D1} - R_{D2})R_{C1} - (R_1 + R_{D1})(R_2 + R_{D2}))R_o + R_{C2}((-(R_1 + R_{on})((R_1 + R_{D1} + R_{C1})n^2 - 2R_{C1}(R_1 + R_{on})n + (R_{D2} - R_{on} + R_2 + R_{D1})R_{C1} - (R_{on} - R_{D1})(R_2 + R_{D2}))d + (-R_1 - R_2 - R_{D1} - R_{D2})R_{C1} - (R_1 + R_{D1})(R_2 + R_{D2})))/(L_m(((R_1 + R_{D1} + R_{C1})n^2 + 2R_{C1}n + R_{C1} + R_2 + R_{C2} + R_{D2})R_o + R_{C2} + R_{D2}((R_1 + R_{D1} + R_{C1})n^2 + 2R_{C1}n + R_{C1} + R_2 + R_{D2})) \tag{3.98}$$

$$Baj = (((-1 + d)R_{C2} + ((-R_1 - R_{D1})n + R_{D2} + R_2)d + (R_1 + R_{D1})n - R_2 - R_{D2})R_o + R_{C2}(((-R_1 - R_{D1})n + R_{D2} + R_2)d + (R_1 + R_{D1})n - R_2 - R_{D2}))/(L_m(((R_1 + R_{D1} + R_{C1})n^2 + 2R_{C1}n + R_{C1} + R_2 + R_{C2} + R_{D2})R_o + R_{C2} + R_{D2}((R_1 + R_{D1} + R_{C1})n^2 + 2R_{C1}n + R_{C1} + R_2 + R_{D2}))) \tag{3.99}$$

$$Caj = ((((R_1 + R_{D1} + R_{C1})n + R_{C1})d(-R_{C1} - R_1 - R_{D1})n - R_{C1})R_o)/(L_m(((R_1 + R_{D1} + R_{C1})n^2 + 2R_{C1}n + R_{C1} + R_2 + R_{C2} + R_{D2})R_o + R_{C2} + R_{D2}((R_1 + R_{D1} + R_{C1})n^2 + 2R_{C1}n + R_{C1} + R_2 + R_{D2}))) \tag{3.100}$$

$$Daj = -((-1 + d)(((-R_1 - R_{D1})R_o + R_{C2}(-R_1 - R_{D1}))n + (R_{C2} + R_2 + R_{D2})R_o + R_{C2}(R_2 + R_{D2})))/(C_1((R_{C2} + R_o)(R_1 + R_{D1} + R_{C1})n^2 + 2R_{C1}(R_{C2} + R_o)n + (R_{C1} + R_2 + R_{C2} + R_{D2})R_o + R_{C2}(R_{C1} + R_2 + R_{D2}))) \tag{3.101}$$

$$Eaj = (-(-1 + d)(((-R_1 - R_{D1})R_o + R_{C2}(-R_1 - R_{D1}))n + (R_{C2} + R_2 + R_{D2})R_o + R_{C2}(R_2 + R_{D2})))/(C_1((R_{C2} + R_o)(R_1 + R_{D1} + R_{C1})n^2 + 2R_{C1}(R_{C2} + R_o)n + (R_{C1} + R_2 + R_{C2} + R_{D2})R_o + R_{C2}(R_{C1} + R_2 + R_{D2}))) \tag{3.102}$$

$$Faj = (-(-1 + d)(R_o n + R_o))/(C_1((R_{C2} + R_o)(R_1 + R_{D1} + R_{C1})n^2 + 2R_{C1}(R_{C2} + R_o)n + (R_{C1} + R_2 + R_{C2} + R_{D2})R_o + R_{C2}(R_{C1} + R_2 + R_{D2}))) \tag{3.103}$$

$$Gaj = (-(-1+d)((R_1+R_{D1}+R_{C1})n+R_{C1}){R_o}^2 + (-(-1+d)(R_1+R_{D1}+R_{C1})R_{C2}n - (-1+d)R_{C1}R_{C2})R_o)/((R_{C2}+R_o)(R_1+R_{D1}+R_{C1})n^2 + 2R_{C1}(R_{C2}+R_o)n + (R_{C1}+R_2+R_o+R_{D2})R_{C2} + R_o(R_{C1}+R_2+R_{D2}))) \quad (3.104)$$

$$Haj = (-(-1+d)(n+1){R_o}^2 + (-(-1+d)R_{C2}n + (1-d)R_{C2})R_o)/((R_{C2}+R_o)(R_1+R_{D1}+R_{C1})n^2 + 2R_{C1}(R_{C2}+R_o)n + (R_{C1}+R_2+R_o+R_{D2})R_{C2} + R_o(R_{C1}+R_2+R_{D2}))) \quad (3.105)$$

$$Iaj = ((-1+d){R_o}^2 + (-(R_1+R_{D1}+R_{C1})n^2 - 2R_{C1}n - R_{C2} - R_{C1} - R_2 - R_{D2})R_o - R_{C2}((R_1+R_{D1}+R_{C1})n^2 + 2R_{C1}n + R_{C1} + R_2 + R_{D2}))/((R_{C2}+R_o)(R_1+R_{D1}+R_{C1})n^2 + 2R_{C1}(R_{C2}+R_o)n + (R_{C1}+R_2+R_o+R_{D2})R_{C2} + R_o(R_{C1}+R_2+R_{D2}))) \quad (3.106)$$

$$Abj = (((2.894232639R_{C1} - 2.894232639R_{on} + 2.894232639R_{D1} + V_{Df} + 35.40548852)R_{C2} - (R_1+R_{D1}+R_{C1})(2.894232639R_1 + 2.894232639R_{on} - V_{in})n^2 + (-5.788465278R_{C1}(R_1+R_{on}) + (2V_{Df} + V_{in} + 169.8992782)R_{C1} + (R_1+R_{D1})(V_{Df}+134.4937897))n + 2.894232639(R_{D2} - R_{on} + R_2 + R_{D1})R_{C1} - 2.894232639(R_{on} - R_{D1})(R_2+R_{D2}) + (2V_{Df} + 169.8992782)R_{C1} + (V_{Df} + 35.40548852)(R_2+R_{D2}))R_o + R_{C2}(-(R_1+R_{D1}+R_{C1})(2.894232639R_1 + 2.894232639R_{on} - V_{in})n^2 + (-5.788465278R_{C1}(R_1+R_{on}) + (2V_{Df}+V_{in})R_{C1} + (R_1+R_{D1})(V_{Df} - 35.40548852))n + 2.894232639(R_{D2} - R_{on} + R_2 + R_{D1})R_{C1} - 2.894232639(R_{on} - R_{D1})(R_2+R_{D2}) + 2R_{C1}V_{Df} + (V_{Df} + 35.40548852)(R_2+R_{D2})))/(L_m(((R_1+R_{D1}+R_{C1})n^2 + 2R_{C1}n + R_{C1} + R_2 + R_{C2} + R_{D2})R_o + R_{C2} + R_{D2}((R_1+R_{D1}+R_{C1})n^2 + 2R_{C1}n + R_{C1} + R_2 + R_{D2}))) \quad (3.107)$$

$$Bbj = ((R_{C2} + ((R_1+R_{D1}+R_{C1})n^2 + R_{C1}n)d + R_{C1}n + R_{C1} + R_2 + R_{D2})R_o + R_{C2}(((R_1+R_{D1}+R_{C1})n^2 + R_{C1}n)d + R_{C1}n + R_{C1} + R_2 + R_{D2}))/(L_m(((R_1+R_{D1}+R_{C1})n^2 + 2R_{C1}n + R_{C1} + R_2 + R_{C2} + R_{D2})R_o + R_{C2} + R_{D2}((R_1+R_{D1}+R_{C1})n^2 + 2R_{C1}n + R_{C1} + R_2 + R_{D2}))) \quad (3.108)$$

$$Cbj = (((-1+d)R_{C2} + ((2R_{C1}+R_1+R_{D1})n + 2R_{C1} + R_2 + R_{D2})d + (-2R_{C1} - R_1 - R_{D1})n - 2R_{C1} - R_2 - R_{D2})R_o + R_{C2}(((2R_{C1}+R_1+R_{D1})n + 2R_{C1} + R_2 + R_{D2})d(-2R_{C1} - R_1 - R_{D1})n - 2R_{C1} - R_2 - R_{D2}))/(L_m(((R_1+R_{D1}+R_{C1})n^2 + 2R_{C1}n + R_{C1} + R_2 + R_{C2} + R_{D2})R_o + R_{C2} + R_{D2}((R_1+R_{D1}+R_{C1})n^2 + 2R_{C1}n + R_{C1} + R_2 + R_{D2}))) \quad (3.109)$$

$$Dbj = -(-(R_{C2}+R_o)(V_{Df} - V_{in} + 35.40548853)n^2 + ((-2.894232639R_1 - 2.894232639R_{D1} + V_{in} + 99.08830116)R_o + R_{C2}(-2.894232639R_1 - 2.894232639R_{D1} + V_{in} - 70.81087704))n + (2.894232639R_{C2} + 2.894232639R_2 + 2.894232639R_{D2} + V_{Df} + 134.4937897)R_o + R_{C2}(2.894232639R_2 + 2.894232639R_{D2} + V_{Df} - 35.40548853))/(C_1((R_{C2}+R_o)(R_1+R_{D1}+R_{C1})n^2 + 2R_{C1}(R_{C2}+R_o)n + (R_{C1}+R_2+R_{C2}+R_{D2})R_o + R_{C2}(R_{C1}+R_2+R_{D2}))) \quad (3.110)$$

$$Ebj = (-(-1+d)((R_{C2}+R_o)n^2+(R_{C2}+R_o)n))/(C_1((R_{C2}+R_o)(R_1+R_{D1}+R_{C1})n^2+2R_{C1}(R_{C2}+R_o)n+(R_{C1}+R_2+R_{C2}+R_{D2})R_o+R_{C2}(R_{C1}+R_2+R_{D2}))) \quad (3.111)$$

$$Fbj = (-(-1+d)(-(R_{C2}+R_o))n^2+R_o+R_{C2}))/(C_1((R_{C2}+R_o)(R_1+R_{D1}+R_{C1})n^2+2R_{C1}(R_{C2}+R_o)n+(R_{C1}+R_2+R_{C2}+R_{D2})R_o+R_{C2}(R_{C1}+R_2+R_{D2}))) \quad (3.112)$$

$$Gbj = (-((2.894232639R_{C1}+2.894232639R_1+2.894232639R_{D1}-V_{in}+35.4054885+V_{Df})n+2.894232639R_{C1}-V_{Df}-134.4937897){R_o}^2+(-(2.894232639R_{C1}+2.894232639R_1+2.894232639R_{D1}-V_{in}+35.4054885+V_{Df})R_{C2}n+(V_{Df}-2.894232639R_{C1}-35.4054885)R_{C2})R_o)/((R_{C2}+R_o)(R_1+R_{D1}+R_{C1})n^2+2R_{C1}(R_{C2}+R_o)n+(R_{C1}+R_2+R_o+R_{D2})R_{C2}+R_o(R_{C1}+R_2+R_{D2}))) \quad (3.113)$$

$$Hbj = ((-1+d)n{R_o}^2+(-1+d)R_{C2}nR_o)/((R_{C2}+R_o)(R_1+R_{D1}+R_{C1})n^2+2R_{C1}(R_{C2}+R_o)n+(R_{C1}+R_2+R_o+R_{D2})R_{C2}+R_o(R_{C1}+R_2+R_{D2}))) \quad (3.114)$$

$$Ibj = (-(-1+d)(n-1){R_o}^2+(-(-1+d)R_{C2}n+(-1+\mathrm{d})R_{C2})R_o)/((R_{C2}+R_o)(R_1+R_{D1}+R_{C1})n^2+2R_{C1}(R_{C2}+R_o)n+(R_{C1}+R_2+R_o+R_{D2})R_{C2}+R_o(R_{C1}+R_2+R_{D2}))). \quad (3.115)$$

So, to develop a linearized model it is necessary to consider the converter operating point in which our model is going to be valid. This model can represent the converter in linear behavior around this point and with very small variations of it, and that is why this technique is called small-signal model. The converter operating point can be obtained from equations (3.93), (3.94) and (3.95), from the large-signal model, equals to zero. This is an equilibrium point of the converter, and then it is known that the system is going to vary linearly around it. Sufficiently small variations in our model are going to be represented as $\Delta i_{Lm}, \Delta v_{C1}, \Delta v_{C2}, \Delta d, \Delta V_{in}$, and ΔV_{Df}. Then, the Small-signal model is:

$$\frac{d}{dt}\begin{bmatrix}\Delta i_{Lm}\\ \Delta v_{C1}\\ \Delta v_{C2}\end{bmatrix} = \begin{bmatrix}Aaj & Baj & Caj\\ Daj & Eaj & Faj\\ Gaj & Haj & Iaj\end{bmatrix}\begin{bmatrix}\Delta i_{Lm}\\ \Delta v_{C1}\\ \Delta v_{C2}\end{bmatrix} + \begin{bmatrix}Abj & Bbj & Cbj\\ Dbj & Ebj & Fbj\\ Gbj & Hbj & Ibj\end{bmatrix}\begin{bmatrix}\Delta d\\ \Delta V_{in}\\ \Delta V_{Df}\end{bmatrix}. \quad (3.116)$$

Substituting the following values to better exemplify this technique: $V_{in} = 35$ V, $I_o = 0{,}5075$ A, $D = 0.5, n = 4, L_m = 100$ µH, $R_1 = 0.1\ \Omega, R_2 = 0.1\ \Omega$, $R_{on} = 0.1\ \Omega, C_1 = 5$ µF, $C_2 = 5$ µF, $R_{C1} = 0.1\ \Omega, R_{C2} = 0.1\ \Omega, V_{Df} = 0.7\ V, R_{D1} = 0.1\ \Omega, R_{D2} = 0.1\ \Omega$, it is obtained as operating points: $I_{Lm} = 5.07$ A, $V_{C1} = 68.08$ V and $V_{C2} = 203.06$ V.

Also, substituting the assumed values and the operating points in (3.116), the resulting small-signal model is:

$$\frac{d}{dt}\begin{bmatrix}\Delta i_{Lm}\\ \Delta v_{C1}\\ \Delta v_{C2}\end{bmatrix}=\begin{bmatrix}-1091.66\Delta i_{Lm}+416.68\Delta v_{C1}-1083.06\Delta v_{C2}+679693.35\Delta d+5666.64\Delta V_{in}-1749.98\Delta V_{Df}\\ -8333.78\Delta i_{Lm}-416668.40\Delta v_{C1}+83312.85\Delta v_{C2}+0.0105\Delta d+33334.72\Delta V_{in}-250001.04\Delta V_{Df}\\ 21661.34\Delta i_{Lm}+83312.85\Delta v_{C1}-17158.28\Delta v_{C2}-203015.69\Delta d-66650.28\Delta V_{in}+49987.71\Delta V_{Df}\end{bmatrix} \quad (3.117)$$

Finally, as detailed in Appendix C, the transfer function can be extracted from the small-signal model solving the following equation:

$$\overrightarrow{Y(s)}=\boldsymbol{C}(s\boldsymbol{I}-\boldsymbol{A}_J)^{-1}\boldsymbol{B}_J\overrightarrow{U(s)}+\boldsymbol{D}\overrightarrow{U(s)}, \quad (3.118)$$

where the matrices **I**, **C** and **D**, in this case, are considered as:

$$\boldsymbol{I}=\begin{bmatrix}1 & 0 & 0\\ 0 & 1 & 0\\ 0 & 0 & 1\end{bmatrix}, \quad (3.119)$$

$$\boldsymbol{C}=[0 \quad 0 \quad 1], \quad (3.120)$$

$$\boldsymbol{D}=[0 \quad 0 \quad 0]. \quad (3.121)$$

Still assuming the same values used in the small-signal model example, the resulting transfer function is:

$$\frac{\Delta v_o}{\Delta d}=\frac{-203015.69s^3-7.03\times10^{10}s^2+5.49\times10^{15}s+6.08\times10^{18}}{s^4+436010.0049s^3+1.18\times10^9s^2+9.33\times10^{12}s+9.34\times10^{15}}. \quad (3.122)$$

The equation (3.122) was validated through PSIM simulation, and the Bode Plot is shown in Figure 3.8, in which the red line is the simulated dynamic behavior of Boost Converter with GC-I (such as in Figure 3.5) and the blue line is the Bode plot of the transfer function (3.122), obtained from the small-signal model of (3.117).

Figure 3.8 – Bode Plot of Boost Converter with GC-I compared to the Transfer Function obtained from its Small-signal Model.

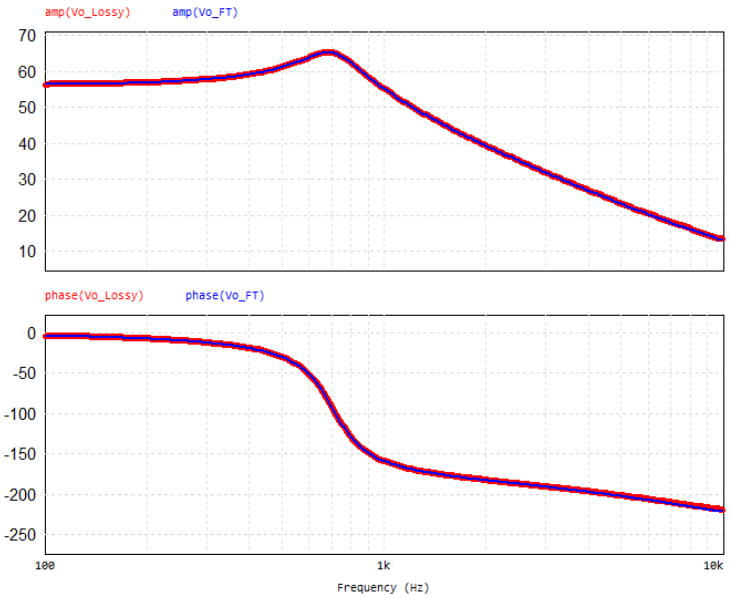

Source: Elaborated by the author.

3.7 OTHER LOSSY BOOST CONVERTERS WITH GAIN CELLS

As seen in the previous section, when the parasitic components are added to the converters models, the level of difficulty rises to represent them through readable equations. Even though the mathematical aspects of the modeling do not change so much – such as the electric circuit analysis and averaging modeling techniques –, the equations lengths are complicated to follow.

So, for the next converters analyzed in this study, most of these long equations resulted from their analysis are going to be hidden from this document – keeping in mind that the procedure to obtain their transfer functions are the same shown in the previous section with a simpler converter topology.

Lossy Boost Converter with GC-III

The methodology presented in the previous section can also be applied to the other two converters studied. The lossy Boost converter with Gain Cell III (GC-III) is shown in Figure 3.11(a), with the coupled inductor replaced by its ideal electrical model and

considering all the other assumptions previously stated, as well as the parasitic components added – diodes forward voltages and all other equivalent series resistances.

During the first operating stage represented in Figure 3.11(b), the switch S is ON, as well as diode D_3, while diodes D_1 and D_2 are blocked. Its duration interval is dT. Analyzing the circuit, using Kirchhoff's voltage law, results in:

Loop 1:

$$-V_i + V_{Lm} + I_1(R_1 + R_{on}) = 0\,. \tag{3.123}$$

Loop 2:

$$V_{Df} - I_2(R_{D3} + R_{C3} + R_2) + V_{C3} - nV_{Lm} = 0\,. \tag{3.124}$$

Loop 3:

$$-I_{C2}R_{C2} - V_{C2} + I_oR_o = 0\,. \tag{3.125}$$

Node 1:

$$I_{Lm} = I_1 + nI_2\,. \tag{3.126}$$

Node 2:

$$I_{C3} = I_2\,. \tag{3.127}$$

Node 3:

$$I_{C2} = -I_o\,. \tag{3.128}$$

Also:

$$I_{C1} = 0\,, \tag{3.129}$$

$$I_{C2} = C_2\frac{dV_{C2}}{dt}\,, \tag{3.130}$$

$$I_{C3} = -C_3\frac{dV_{C3}}{dt}\,, \tag{3.131}$$

$$V_{Lm} = L_m\frac{di_{Lm}}{dt}\,. \tag{3.132}$$

Figure 3.9 – (a) Circuit diagram of the Lossy GC-III Boost Converter. (b) First operating Stage; (c) Second operating stage.

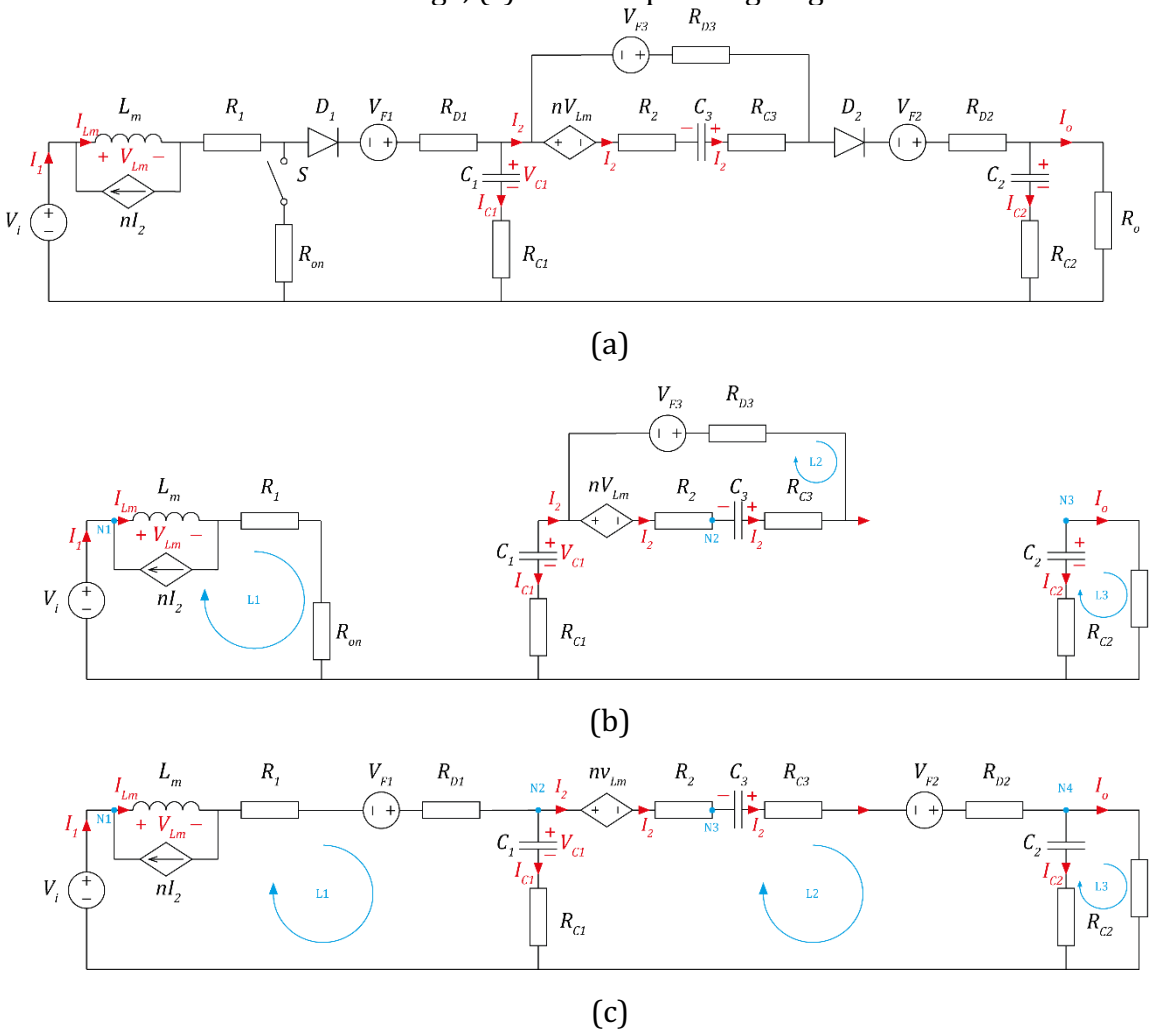

Source: Elaborated by the author.

Solving the system with all the equations obtained results in:

$$\frac{dV_{C1}}{dt} = 0\,, \tag{3.133}$$

$$\frac{dV_{C2}}{dt} = -\frac{V_{C2}}{(R_{C2}+R_o)C_2}, \tag{3.134}$$

$$\frac{dV_{C3}}{dt} = \frac{\left((-R_1-R_{on})I_{Lm}+V_i\right)n - V_{C3} - V_{F3}\ ,}{((R_1+R_{on})n^2+R_2+R_{C3}+R_{D3})C_3} \tag{3.135}$$

$$\frac{di_{Lm}}{dt} = (-I_{Lm}(R_{D3}+R_{C3}+R_2)(R_1+R_{on}) + n(V_{C3}+V_{F3})R_{on} + n(V_{C3} + V_{F3})R_1 + V_i(R_{D3}+R_{C3}+R_2))/(L_m((R_1n^2 + R_{on}n^2 + R_2 + R_{C3}) + R_{D3}). \tag{3.136}$$

Figure 3.11(b) shows the second operating stage, in which the duration interval can be approximated by $(1-d)T$. Applying Kirchhoff's law to the equivalent circuit:

Loop 1:

$$-V_i + V_{Lm} + I_1(R_1 + R_{D1}) + V_{Df} + V_{C1} + (I_1 - I_2)R_{C1} = 0\,. \tag{3.137}$$

Loop 2:

$$(I_2 - I_1)R_{C1} - V_{C1} + nV_{Lm} + I_2(R_2 + R_{C3} + R_{D2}) - V_{C3} + V_{Df} + V_{C2} + (I_2 - I_o)R_{C2} = 0\,. \tag{3.138}$$

Loop 3:

$$(I_2 - I_o)R_{C2} - V_{C2} + I_o R_o = 0\,. \tag{3.139}$$

Node 1:

$$I_{Lm} = I_1 + nI_2\,. \tag{3.140}$$

Node 2:

$$I_{C1} = I_1 - I_2\,. \tag{3.141}$$

Node 3:

$$I_{C3} = I_2\,. \tag{3.142}$$

Node 4:

$$I_{C2} = I_2 - I_o\,. \tag{3.143}$$

Also:

$$I_{C1} = C_1 \frac{dV_{C1}}{dt}, \tag{3.144}$$

$$I_{C2} = C_2 \frac{dV_{C2}}{dt}, \tag{3.145}$$

$$I_{C3} = -C_3 \frac{dV_{C3}}{dt}, \tag{3.146}$$

$$V_{Lm} = L_m \frac{di_{Lm}}{dt}. \tag{3.147}$$

Solving the system with all the equations obtained, results in:

$$di_{Lm} = (((-I_{Lm}R_{C1} + (-R_{D1} - R_1)I_{Lm} - V_{C1} - V_{F1} + V_i)R_{C2} + ((-V_{C2} + V_{C3} - V_{F1} - V_{F2} + V_i)n + (-R_{C3} - R_{D1} - R_{D2} - R_1 - R_2)I_{Lm} - V_{C2} + V_{C3} - V_{F1} - V_{F2} + V_i)R_{C1} + (R_1 + R_{D1})(V_{C1} - V_{C2} + V_{C3} - V_{F2})n - (R_2 + R_{C3} + R_{D2})((R_1 + R_{D1})I_{Lm} + V_{C1} + V_{F1} - V_i))R_o + R_{C2}(((V_{C3} - V_{F1} - V_{F2} + V_i)n + (-R_{C3} - R_{D1} - R_{D2} - R_1 - R_2)I_{Lm} + V_{C3} - V_{F1} - V_{F2} + V_i)R_{C1} + (R_1 + R_{D1})(V_{C1} - V_{C2} + V_{C3} - V_{F2})n - (R_2 + R_{C3} + R_{D2})((R_1 + R_{D1})I_{Lm} + V_{C1} + V_{F1} - V_i)))/(((R_{C2} + (n^2 + 2n + 1)R_{C1} + (R_1 + R_{D1})n^2 + R_{C3} + R_{D2} + R_2)R_o + ((n + 1)^2R_{C1} + (R_1 + R_{D1})n^2 + R_{C3} + R_{D2} + R_2)R_{C2})L_m) \quad (3.148)$$

$$dV_{C1} = (-(R_{C2} + R_o)(V_{C1} + V_{F1} - V_i)n^2 + (((-R_{D1} - R_1)I_{Lm} - 2V_{C1} + V_{C2} - V_{C3} - V_{F1} + V_{F2} + V_i)R_o - R_{C2}((R_1 + R_{D1})I_{Lm} + 2V_{C1} + V_{C3} + V_{F1} - V_{F2} - V_i))n + (I_{Lm}R_{C2} + (R_2 + R_{C3} + R_{D2})I_{Lm} - V_{C1} + V_{C2} - V_{C3} + V_{F2})R_o + R_{C2}((R_2 + R_{C3} + R_{D2})I_{Lm} - V_{C1} + V_{C2} - V_{C3} + V_{F2}))/(((R_{C2} + R_o)(R_1 + R_{C1} + R_{D1})n^2 + 2R_{C1}(R_{C2} + R_o)n + (R_{C3} + R_{D2} + R_2 + R_{C1} + R_{C2})R_o + R_{C2}(R_{D2} + R_2 + R_{C1} + R_{C3}))C_1) \quad (3.149)$$

$$dV_{C2} = (((I_{Lm}R_{C1} + (R_1 + R_{D1})I_{Lm} + V_{C1} + V_{F1} - V_i)n + I_{Lm}R_{C1} + V_{C1} - V_{C2} + V_{C3} - V_{F2})R_o - ((R_1 + R_{C1} + R_{D1})n^2 + 2R_{C1}n + R_{C3} + R_{D2} + R_2 + R_{C1})V_{C2})/((((R_1 + R_{C1} + R_{D1})n^2 + 2R_{C1}n + R_{C3} + R_{D2} + R_2 + R_{C1} + R_{C2})R_o + ((R_1 + R_{C1} + R_{D1})n^2 + 2R_{C1}n + R_{C3} + R_{D2} + R_2 + R_{C1})R_{C2})C_2) \quad (3.150)$$

$$dV_{C3} = ((((-I_{Lm}R_{C1} + (-R_{D1} - R_1)I_{Lm} - V_{C1} - V_{F1} + V_i)n - I_{Lm}R_{C1} - V_{C1} + V_{C2} - V_{C3} + V_{F2})R_o - R_{C2}((I_{Lm}R_{C1} + (R_1 + R_{D1})I_{Lm} + V_{C1} + V_{F1} - V_i)n + I_{Lm}R_{C1} + V_{C1} - V_{C2} + V_{C3} - V_{F2}))/((((R_1 + R_{C1} + R_{D1})n^2 + 2R_{C1}n + R_{C3} + R_{D2} + R_2 + R_{C1} + R_{C2})R_o + ((R_1 + R_{C1} + R_{D1})n^2 + 2R_{C1}n + R_{C3} + R_{D2} + R_2 + R_{C1})R_{C2})C_3). \quad (3.151)$$

The procedure to obtain the average large-signal model and the small-signal model using the equations from the analysis of both operating stages is exactly the same from the previous section. The models equations, as mentioned before, are very long and complicated to follow, so considering the parameters already used, the transfer function can be obtained:

$$\frac{\Delta v_o}{\Delta d} = (-308327.81s^{11} - 3.59 \times 10^{11}s^{10} - 1.37 \times 10^{17}s^9 - 1.63 \times 10^{22}s^8 + 4.07 \times 10^{26}s^7 + 1.84 \times 10^{31}s^6 + 3.69 \times 10^{34}s^5 + 3.66 \times 10^{38}s^4 + 3.02 \times 10^{41}s^3 + 9.69 \times 10^{43}s^2 + 1.38 \times 10^{46}s + 7.46 \times 10^{47})/(s^{12} + 1.26 \times 10^6s^{11} + 5.40 \times 10^{11}s^{10} + 8.26 \times 10^{16}s^9 + 1.80 \times 10^{21}s^8 + 1.29 \times 10^{25}s^7 + 8.01 \times 10^{28}s^6 + 2.50 \times 10^{32}s^5 + 7.91 \times 10^{35}s^4 + 5.82 \times 10^{38}s^3 + 1.78 \times 10^{41}s^2 + 2.50 \times 10^{43}s + 1.32 \times 10^{45}) \quad (3.152)$$

The equation (3.152) was also validated through PSIM simulation, and the Bode Plot is shown in Figure 3.10, in which the red line is the simulated dynamic behavior of

Boost Converter with GC-III (such as in Figure 3.9(a)) and the blue line is the Bode plot of the transfer function (3.152), obtained from the small-signal model of this converter using the parameters previously stated.

Figure 3.10 – Bode Plot of Boost Converter with GC-III compared to the Transfer Function obtained from its Small-signal Model.

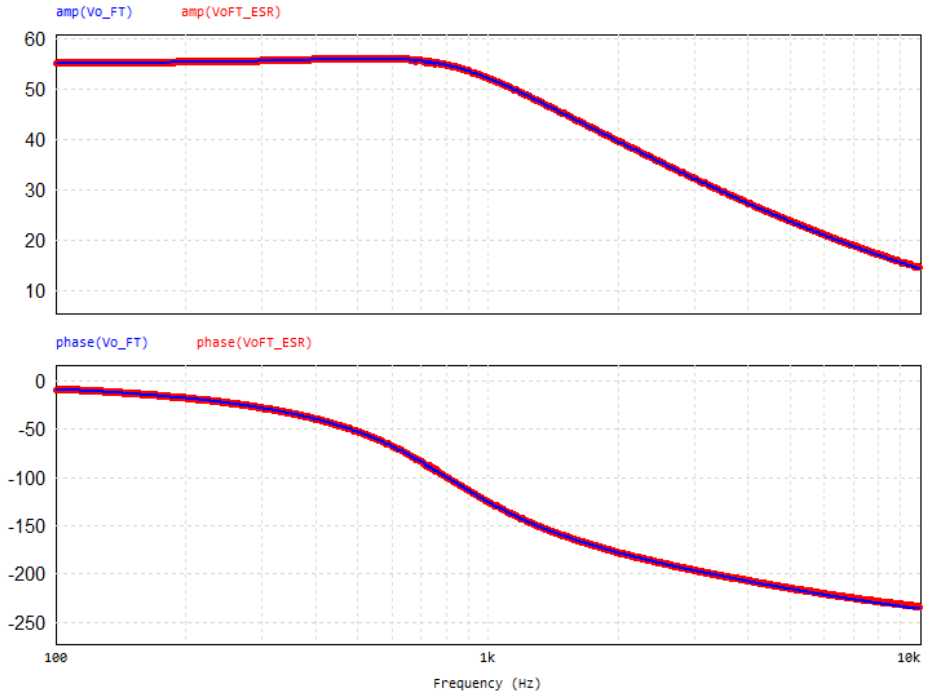

Source: Elaborated by the author.

Lossy Boost Converter with GC-V

The Boost converter with Gain Cell V, including its parasitic components, is represented in Figure 3.11(a), along with its operating stages. Figure 3.11(b) displays the equivalent circuit for the time interval dT and Figure 3.11(c) represents the equivalent circuit for the $1\text{-}dT$ time interval.

Figure 3.11 – (a) Circuit diagram of the Lossy GC-V Boost Converter. (b) First operating Stage. (c) Second operating stage.

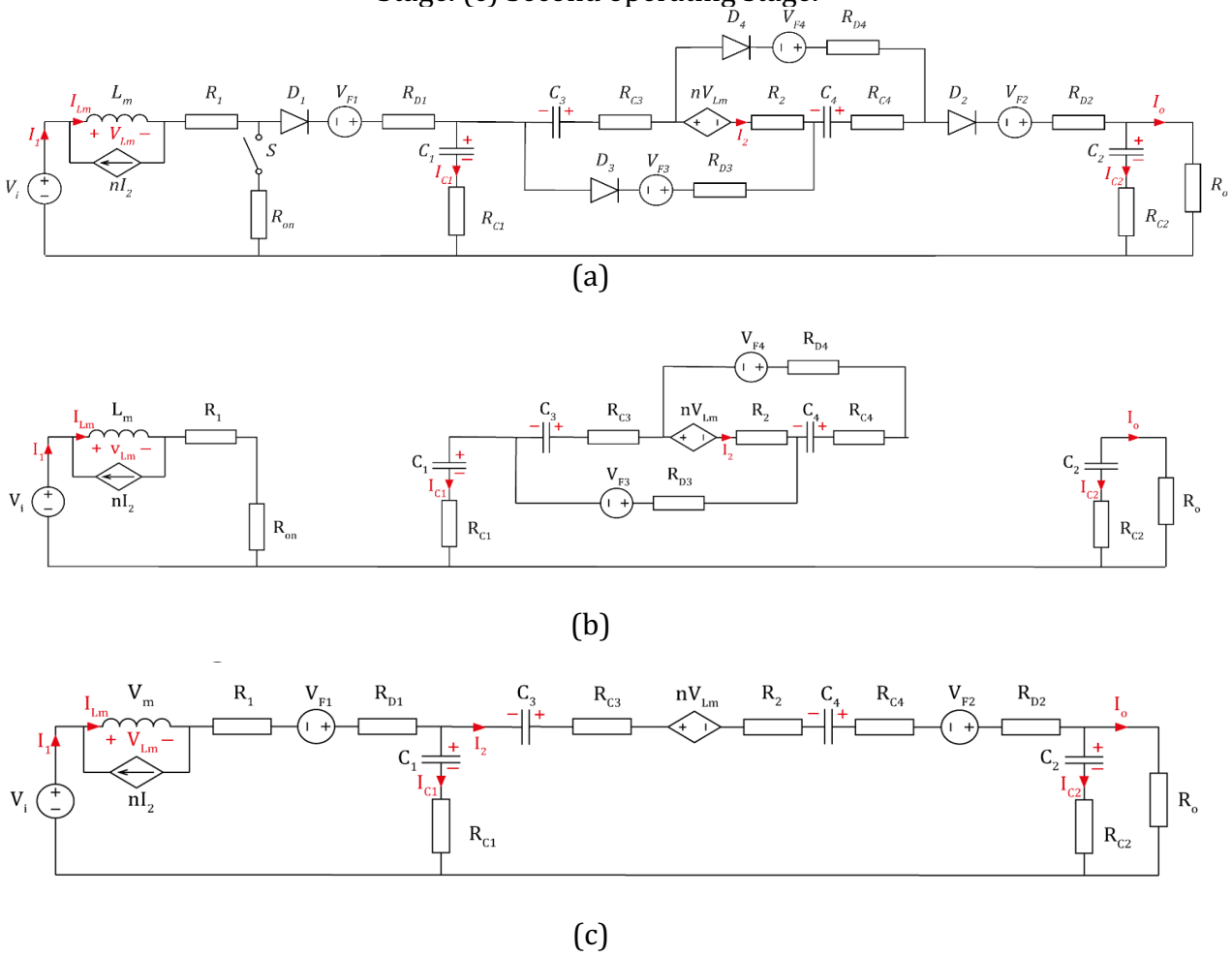

Source: Elaborated by the author.

The circuit analysis using Kirchhoff's laws was performed following the same methodology of the previous addressed converters and taking the same averaging techniques to obtain its large-signal and small-signal models. These models' equations are the longest among all converters studied, so adopting the same parameters, it is going to be addressed its transfer function directly:

$$\frac{\Delta v_o}{\Delta d} = (-408149s^{27} - 1.76 \times 10^{12}s^{26} - 3.37 \times 10^{18}s^{25} - 3.74 \times 10^{24}s^{24} - 3.83 \times 10^{41}s^{21} - 7.48 \times 10^{46}s^{20} - 8.15 \times 10^{51}s^{19} - 3.30 \times 10^{56}s^{18} + 9.41 \times 10^{60}s^{17} + 2.30 \times 10^{65}s^{16} + 1.45 \times 10^{69}s^{15} + 1.51 \times 10^{73}s^{14} + 5.38 \times 10^{76}s^{13} + 3.15 \times 10^{80}s^{12} + 7.19 \times 10^{83}s^{11} + 2.27 \times 10^{87}s^{10} + 3.05 \times 10^{90}s^{9} + 2.17 \times 10^{93}s^{8} + 9.57 \times 10^{95}s^{7} + 2.80 \times 10^{98}s^{6} + 5.68 \times 10^{100}s^{5} + 8.03 \times 10^{102}s^{4} + 7.79 \times 10^{104}s^{3} + 4.97 \times 10^{106}s^{2} + 1.88 \times 10^{108}s + 3.20 \times 10^{109})/(s^{28} + 4.45 \times 10^{6}s^{27} + 8.79 \times 10^{12}s^{26} + 1.01 \times 10^{19}s^{25} + 7.42 \times 10^{24}s^{24} + 3.63 \times 10^{30}s^{23} + 1.18 \times 10^{36}s^{22} + 2.49 \times 10^{41}s^{21} + 3.13 \times 10^{46}s^{20} + 1.92 \times 10^{51}s^{19} + 3.06 \times 10^{55}s^{18} + 3.78 \times 10^{59}s^{17} + 2.85 \times 10^{63}s^{16} + 1.94 \times 10^{67}s^{15} + 9.42 \times 10^{70}s^{14} + \quad (3.153)$$

$$3.96 \times 10^{74}s^{13} + 1.30 \times 10^{78}s^{12} + 3.26 \times 10^{81}s^{11} + 6.77 \times 10^{84}s^{10} + 7.54 \times 10^{87}s^{9} + 4.91 \times 10^{90}s^{8} + 2.05 \times 10^{93}s^{7} + 5.83 \times 10^{95}s^{6} + 1.15 \times 10^{98}s^{5} + 1.60 \times 10^{100}s^{4} + 1.54 \times 10^{102}s^{3} + 9.73 \times 10^{103}s^{2} + 3.65 \times 10^{105}s + 6.18 \times 10^{106})$$

As previously done to the other obtained transfer functions, the equation (3.153) was validated through PSIM simulation, and the Bode Plot is shown in Figure 3.12, in which the red line is the simulated dynamic behavior of Boost Converter with GC-V and the blue line is the Bode plot of the transfer function (3.153) obtained from the small-signal model of this converter using the parameters previously stated.

Figure 3.12 – Bode Plot of Boost Converter with GC-V compared to the Transfer Function obtained from its Small-signal Model.

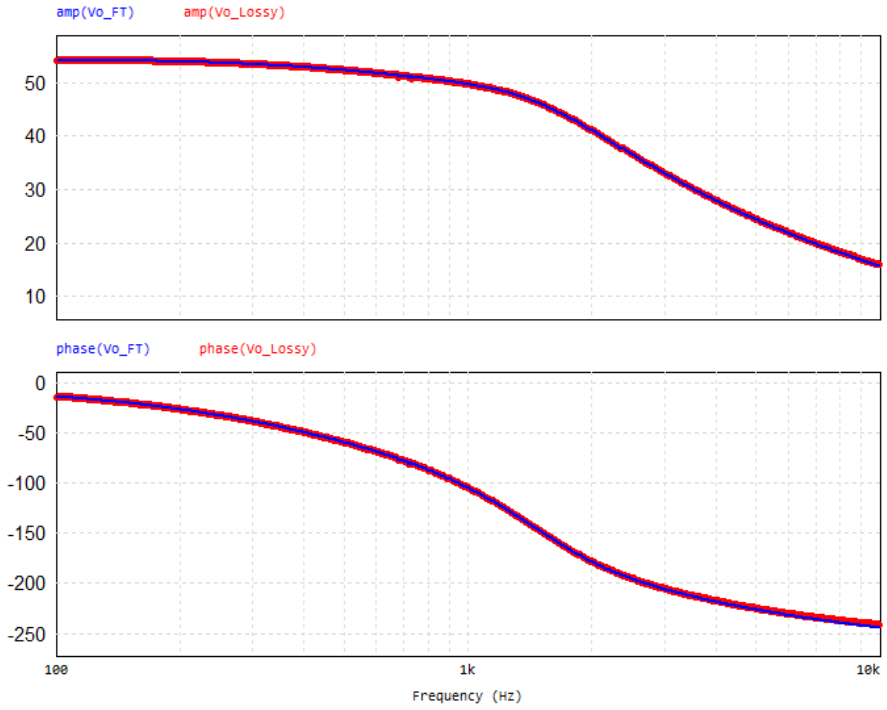

Source: Elaborated by the author.

3.8 CHAPTER CONCLUSIONS

In this chapter it was modeled the most relevant parasitic components in dc-dc converters and these elements were added to the Boost converters with gain cells type I, III and V as addressed in Chapter 2. The equations complexity got more difficult and other techniques were used to obtain average large-signal and small-signal models of these converters, which were validated through their transfers functions in PSIM simulations

as previously shown. In the next chapter, these models are going to be compared to a prototype to test how accurate they are. Besides the Bode Plots of these converters, the step responses of each gain cell configuration are also going to be evaluated to ensure their accuracy and check if the real response of this converter actually shows greater damping than the ideal model as it was seen in the lossy models frequency response.

4 PROTOTYPE OF GAIN-CELL BOOST CONVERTER: ANALYZING LOSSY MODEL ACCURACY

This chapter presents the test results of the gain-cell boost converter prototype, seeking the validation of the study developed and presented in the previous chapters. Both duty cycle step response and frequency response, through Bode diagrams, of each gain cell configuration were performed and evaluated comparing the obtained results with the lossy model simulations, conducted in PSIM software.

4.1 PROTOTYPE DEVELOPMENT

In order to verify the analysis conducted for the proposed converter, the prototype of Figure 4.1 was built and tested. The design specifications of the Boost converter with gain cell were chosen to meet the operating requirements specified in Table 4.1. The purpose of the prototype is for model validation and does not have an immediate practical application, even though the output power and switching frequency chosen values are commonly adopted in projects that work with microinverters for photovoltaic projects, one of the possible practical applications that uses high step-up converters.

Figure 4.1 – Prototype of a high-gain step-up Boost converter with coupled inductor gain cell (85 mm x 70 mm).

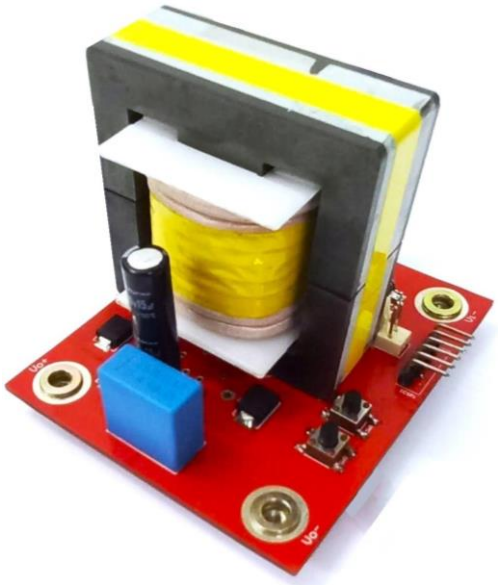

Source: Elaborated by the author.

Table 4.1 – Prototype specifications

Input Voltage	$V_i = 15{\sim}25$ V
Output Load	$R_o = 1$ kΩ
Maximum Output Voltage	$V_o = 400$ V
Maximum Output Power	$P_o = 150$ W
Switching frequency	$f_s = 100$ kHz

Source: Elaborated by the author.

The project followed the methodology presented in [5], which resulted in the components shown in Table 4.2. The equations considered in the project are presented in Appendix D. A single prototype was used to test the three gain cell configurations addressed in this study. As it is easily understandable by reading the previous chapters, the differentiation between the gain cells is due to the inclusion/exclusion of a few components (capacitors and diodes), which allowed this approach of using only one prototype. For example, to test the Boost converter with gain cell III on the same prototype as the Boost converter with gain cell V, it is necessary just to remove a capacitor (C_4) and a diode (D_4) from the board; then, to test the Boost converter with gain cell I in the sequence, just remove another capacitor (C_3) and another diode (D_3) from the prototype. The removed capacitors are substituted for short circuits and the removed diodes are left as open circuits.

Table 4.2– Power stage components.

S_1	IPB039N10N3GATMA1
D_1	TSP15H150SS1GCT-ND
D_2, D_3, D_4	MURS360-M3/57T
C_1	450QXW15MEFR8X30
C_2	B32672P4205K000
C_3, C_4	450QXW15MEFR8X30

Source: Elaborated by the author.

This approach requires that the power stage components used in the prototype must be the same for the three gain cells, meeting the three converters operating conditions simultaneously. Thus, it was thought to maintain the same value of output

voltage and output power, but with different input voltage and duty cycle for each converter. The static gain, consequentially, also vary for each gain cell, although it remained above 10 for all configurations, characterizing high-gain step-up converters. These performance-test strategies will be detailed in the next sections, when each converter test is described.

The components used, according to their datasheets, have properties with loss effects which were taken accountable. The MOSFET and capacitors equivalent series resistances and the diodes forward voltage extracted from the fabricant information are shown in Table 4.3. The diodes series resistances were not available in these semiconductors datasheets and were considered negligible, even though in the models developed in the past chapter they were considered – which makes easy to account them in future studies.

Table 4.3 – Accounted component losses.

S_1	$R_{on} = 4\ \text{m}\Omega$
$Diodes$	$V_{Df} \cong 0.7\ \text{V}$
C_1	$R_{C1} = 0.9\ \Omega$
C_2	$R_{C2} = 15\ \text{m}\Omega$
C_3, C_4	$R_{C3} = R_{C4} = 0.9\ \Omega$

Source: Elaborated by the author.

Unlike the other components, the coupled inductor needs to be designed and developed in laboratory. In this prototype, it was used a coupled inductor projected in [5] and its main parameters are shown in Table 4.4. These parameters were measured using the impedance analyzer Agilent 4294A 40Hz-110MHz. The coupled inductor windings were wound using the interleaving technique. This technique divides the windings into smaller sections, causing the magnetic field inside the windings to decrease. Since the leakage inductance depends on the square of the magnetic field, this technique allows obtaining a reduced leakage inductance compared to simpler technique. In the simpler way, the primary and secondary windings are wound in sequence - for example, all secondary windings first and then all primary windings. In this inductor with interleaving, first half of the secondary windings were wound, then the primary windings, and then the other half of the secondary windings.

Regarding losses of the coupled inductor, it is taken accountable the copper losses, as said in Chapter 3, as R_{L1} and R_{L2}, which were also measured using the impedance analyzer. The $R_{L1}$was the series resistance measured from the primary winding, and R_{L2} the series resistance measured from the secondary winding. These resistances can be added to the series resistances R_{Lk1} and R_{Lk2}, which are equivalent resistors to represent the loss effect of the leakage inductance of the primary and the secondary windings, respectively. If R_{L1} and R_{L2} are the same for all three gain cells, R_{Lk1} and R_{Lk2} vary depending on the configuration and can be obtained using the equation (3.46).

Table 4.4 – Coupled-inductor specification.

Core	E55/28/21 – N87
Primary	9 x 982/AWG41
Secondary	58 x 86/AWG41
Transformation Ratio	$n = 6.4$
Magnetizing Inductance	$L_m = 55$ µH
Leakage Inductance	$L_k = 0.29$ µH
Primary Resistance	$R_{L1} = 0.824$ mΩ
Secondary Resistance	$R_{L2} = 391.64$ mΩ

Source: Elaborated by the author.

The built prototype has buttons to increase/decrease the duty cycle value during the converter operation, thus allowing the duty cycle step response test. The microcontroller dsPIC33EP256MC502 operating with maximum clock frequency of 146,8 MHz. Furthermore, it is through microcontroller programming that it is possible to insert sine waves of different frequencies in the duty cycle signal for tracing the prototype's Bode diagram for the frequency response test.

The full schematic of the prototype is presented in Appendix E, showing the Boost converter with GC-V, the configuration with the most components among all three. For the other configurations addressed, GC-III and GC-I, some components just have to be removed, as previously mentioned. In the following sections the test results are shown; the prototype measurements were taken using the digital oscilloscope Agilent InfiniiVision DSO-X 4054A 500MHz.

The output voltage response of the experimental prototype from each gain cell experiment are presented in the following sections. The duty cycle was increased 1% to perform the step test – in GC-V case, from 0.4 to 0.404; in GC-III case 0.5 to 0.505; and GC-I from 0.6 to 0.606. As mentioned earlier, the first gain cell tested with the prototype was the GC-V because it was assumed that it could be easier to transitioning to the other gain cells afterwards by removing components. So, the test order is first GC-V, then GC-III and ending with the GC-I, and the results are also going to be shown in this sequence. The prototype results are verified with the PSIM simulations of each gain cell. It was employed the transfer function block, *H(s)*, simulated with a step block, as shown in Figure 4.2.

Figure 4.2 – PSIM duty cycle step response simulation using the transfer function block.

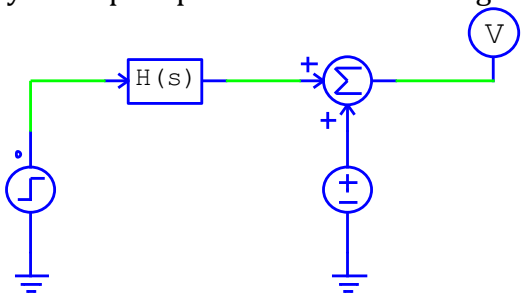

Source: Elaborated by the author.

Then, the frequency responses of the small-signal models of the simulated switching models', and the response of the measured control-to-output transfer function are presented. Using MPLAB software to modify the microcontroller programming, sine waves of different frequencies are added to the duty cycle signal for tracing the prototype's Bode diagram for the frequency response test. The prototype was tested in seventeen different frequencies, from 100 Hz to 5000 Hz. On each time, the amplitude and phase were measured and are displayed in the next sections, for each gain cell. The results were plotted into the Bode diagrams of the models transfer functions obtained with AC Sweep tool of PSIM software, as show in Figure 4.3, in which a sine wave signal was also added to the duty cycle.

Figure 4.3 – PSIM Transfer function block and the AC Sweep tool.

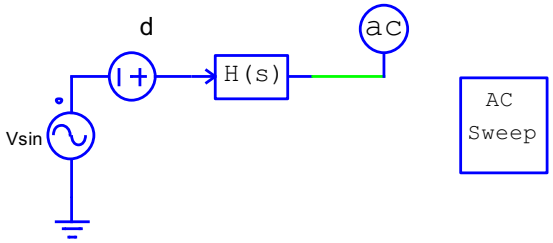

Source: Elaborated by the author.

4.2 GC-V EXPERIMENTAL RESULTS

The first prototype test was run with the converter connected to the GC-V. The project for this configuration with a duty cycle of 40%, following Appendix D equations and the parameters given in the previous section, expected to reach the maximum output voltage of 400 V with an input voltage close to 20 V and a static gain around 18. The results shown in Table 4.5 demonstrate very accurate projected values, with a static gain prediction error of only 6.4%.

Table 4.5 – GC-V prototype static gain test.

Duty cycle	$d = 0.4$
Output Voltage	$V_o = 400\ V$
Input Voltage	$V_i = 23.7\ V$
Static Gain	$M = 16.84$

Source: Elaborated by the author.

Then, the step response test had, as mentioned earlier, the duty cycle increased from 0.4 to 0.404 with an input voltage of 20 V, then resulting $V_o = 337$ V – it was chosen to do not perform with the maximum output voltage. Figure 4.4 shows the obtained wave form, printed from the oscilloscope screen and the transfer function of the lossy-model simulation plotted over it. The result was considered satisfactory since the model is very close to the prototype behavior, even with similar resonant peak. For a better understanding of the influence of losses in the step response, Figure 4.5 shows the lossless switching model of the Bost converter with gain cell V and the transfer function block with the lossy small-signal model previously tested. The comparation between the lossless

model and the lossy model transfer function is shown in Figure 4.6. It is clear the influence of losses in the damping factor, since the lossless response takes longer to settle, and also has a higher peak overshoot. Figure 4.6 also shows that the losses in fact do not have great influence in the rise time, and clearly the lossy model represents better the prototype than the lossless model. More detailed comparation is possible analyzing the frequency response, which was the following test performed.

Figure 4.4 – Duty cycle step response of the GC-V prototype (yellow) versus PSIM simulation (red) of the model transfer function.

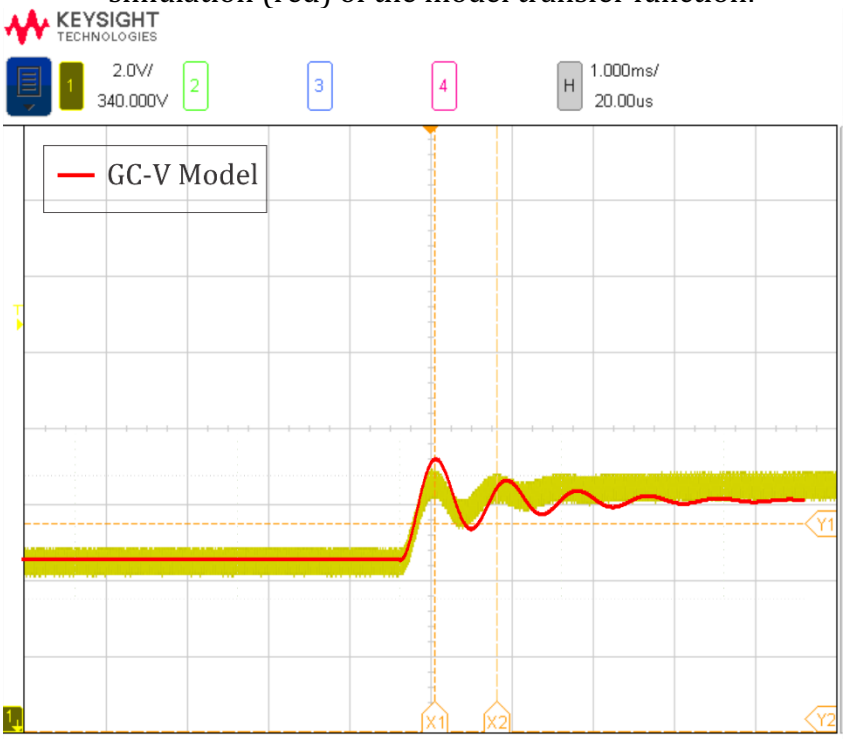

Source: Elaborated by the author.

Regarding the frequency response, as seen in Figure 4.7 the prototype and the lossy model have very similar asymptotic behavior, although the prototype presented a more damped response than the model. It was expected after analyzing the step response of this converter, since a smoother resonant peak often corresponds to a lower overshoot in the system's step response. This means that the system's response to a step input or disturbance will exhibit less oscillation before settling down to the final value – what was shown in Figure 4.4.

Figure 4.5 – Switching model of the lossless Boost converter with gain cell V and the transfer function block with the lossy small-signal model.

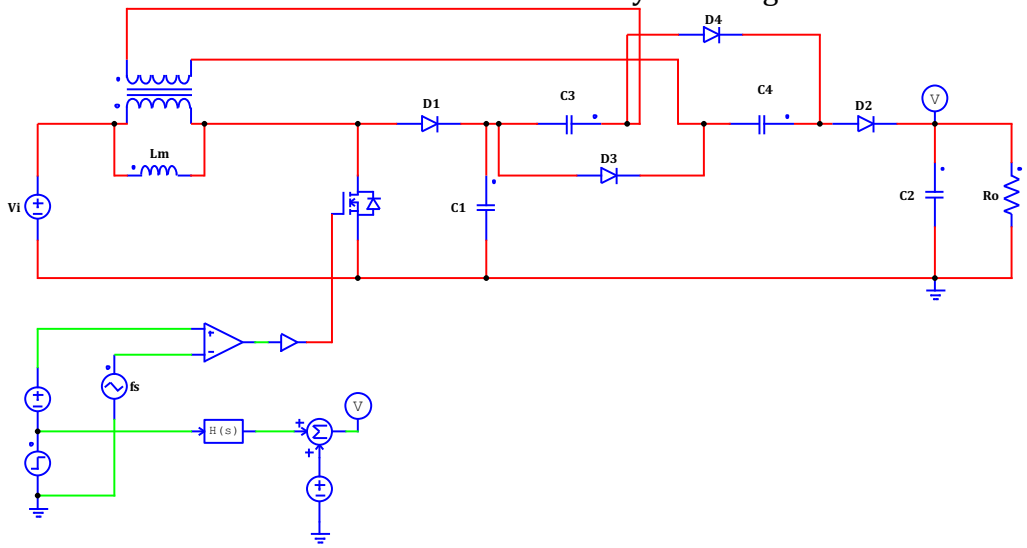

Source: Elaborated by the author.

Figure 4.6 – Duty cycle step response of the switching model of the lossless Boost converter with gain cell V (yellow line) and of the transfer function block with the lossy small-signal model (red line).

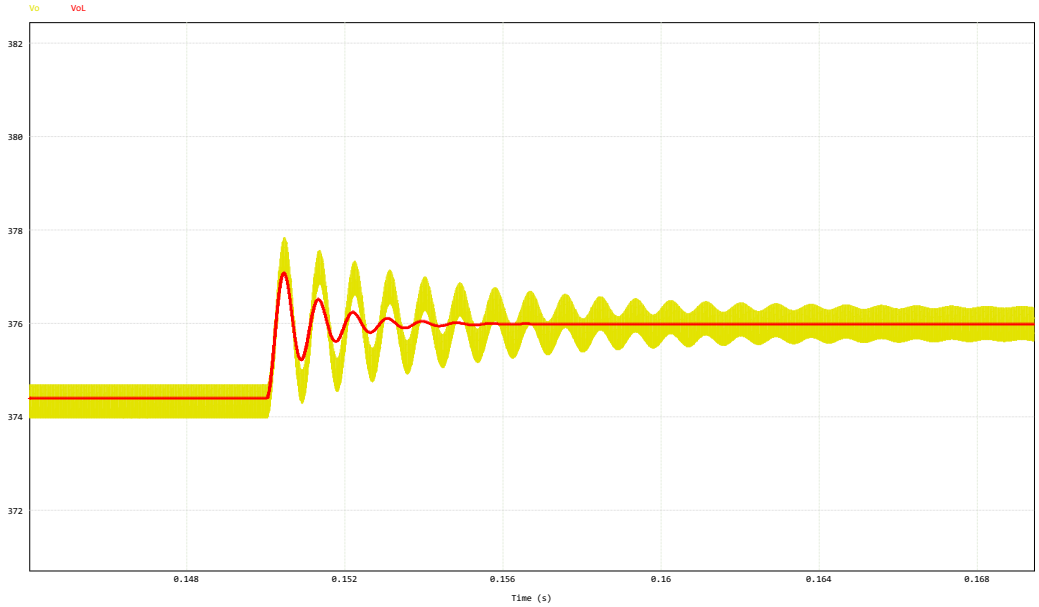

Source: Elaborated by the author.

Also, the smoother resonant peak in the Bode plot could be related to the presence of more or greater parasitic components, such as the already considered Equivalent Series Resistance (ESR), in the lossy model. Probably a better estimation of the coupled inductor losses, for example, would deliver a more accurate lossy model – keeping in mind that the high-frequency losses and core losses of the coupled inductor were not accounted and

could contribute to better results. Parasitic components like ESR can have a significant impact on the behavior of electronic circuits and systems, particularly in components like capacitors and inductors. ESR represents the real (resistive) part of the impedance of a capacitor or an inductor, and it can introduce damping and affect the resonance characteristics of the circuit. ESR causes energy to be dissipated as heat, which results in a gradual reduction in the amplitude of the resonant peak, and also it can introduce phase shifts in the circuit, which can lead to the suppression of sharp resonant behavior. Parasitic components can cause the resonant frequency to shift and spread out, resulting in a broader and smoother peak.

Figure 4.7 – GC-V Bode diagram simulated versus the data obtained from the prototype experiment.

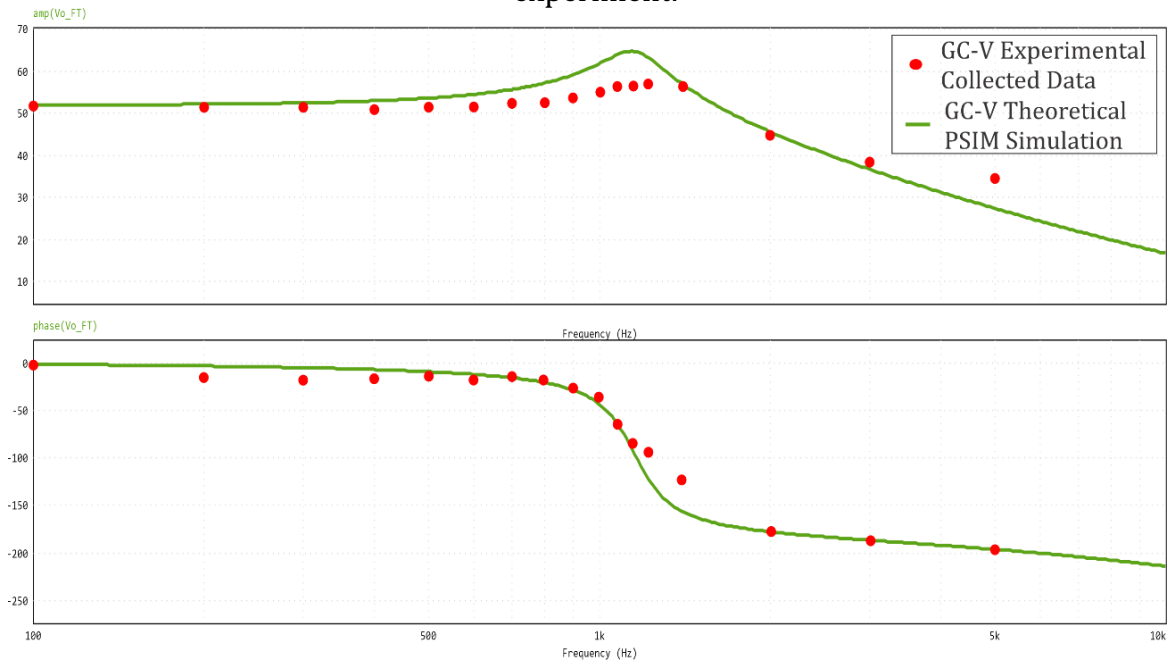

Source: Elaborated by the author.

The addition of parasitic components to the converter model added a much more complex response than the ideal model, as shown in the Figure 4.8. The pole-zero map comparing both lossy and ideal models shows that the model accounting parasitic components resulted in multiple poles and zeros in the left half-plane and one zero in the right half-plane over the real axis, while the lossless model shows just two symmetrical poles along the imaginary axis (conjugate complex poles) in the left half-plane and also one zero in the right half-plane over the real axis. Although a configuration with fewer poles and zeros may be more favorable in terms of predictability and control system

design than one with more poles and zeros, as seen in Figure 4.9, the lossy model represents the real behavior of the converter better than the ideal model, since it also shows a smoother resonant peak as previously discussed.

Figure 4.8 – Pole-zero map of GC-V lossy model (blue) versus ideal model (orange).

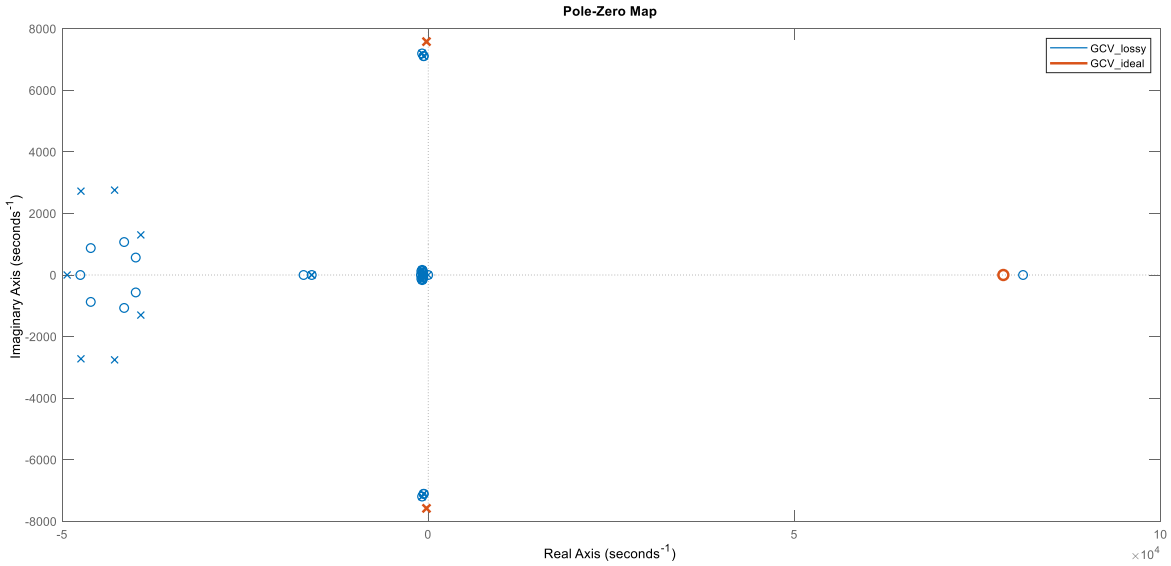

Source: Elaborated by the author.

Figure 4.9 – GC-V Bode diagram lossy model (blue) versus ideal model (orange).

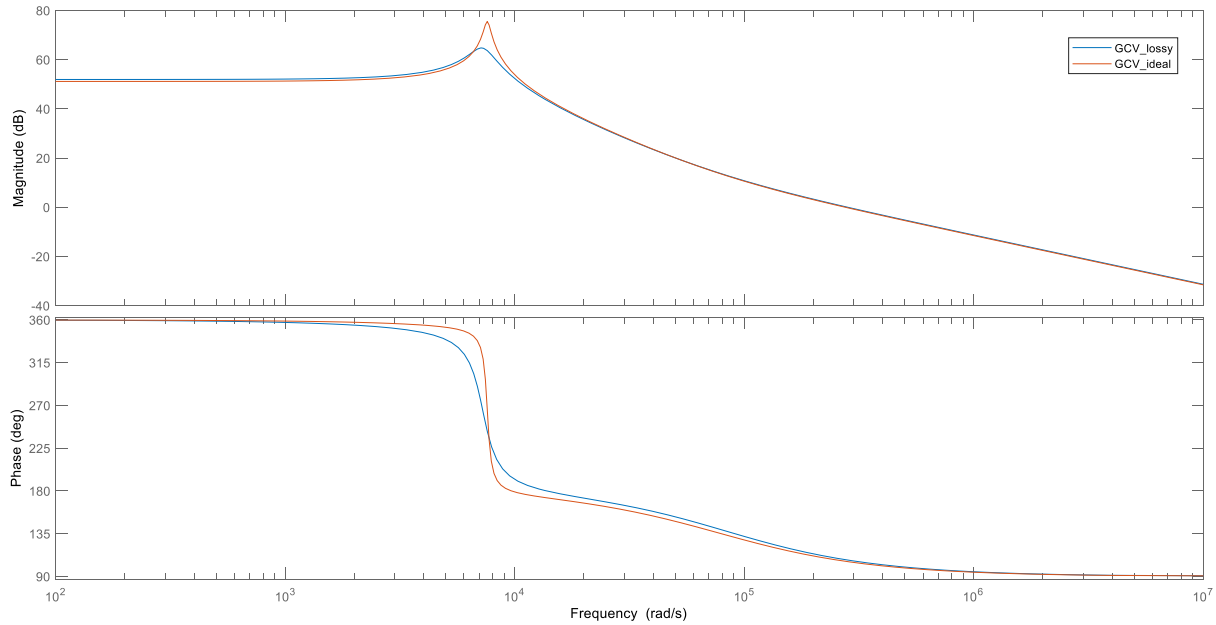

Source: Elaborated by the author.

4.3 GC-III EXPERIMENTAL RESULTS

The next prototype test was performed with the converter connected to the GC-III. The project for this configuration with a duty cycle of 50%, also following Appendix D equations and the parameters given in the previous section, expected to reach the maximum output voltage of 400 V with an input voltage of 27 V and a static gain of 14.8. The results shown in Table 4.6 demonstrated an even smaller static gain prediction error than the previous test, of only 2.09%.

Table 4.6 – GC-III prototype static gain test.

Duty cycle	$d = 0.5$
Output Voltage	$V_o = 400$ V
Input Voltage	$V_i = 27.6$ V
Static Gain	$M = 14.49$

Source: Elaborated by the author.

For the step response test the duty cycle increased from 0.5 to 0.505with with an input voltage of 23 V, then resulting $V_o = 335$ V – it was also chosen to do not perform with the maximum output voltage, yet an approximated output value to the V_o used in the GC-V response tests. The graphic result printed from the oscilloscope screen and the transfer function of the lossy-model simulation plotted over it are shown in Figure 4.10. The prototype reached the steady state value faster than the model, but by inspection it is possible to see that, again, the *rise time* is about the same for both, model and prototype, This results showed a great accuracy, with the model response very similar to the prototype response.

Figure 4.11 shows the lossless switching model of the Bost converter with gain cell III and the transfer function block with the lossy small-signal model already tested in this section. The comparation between the lossless model and the lossy model transfer function step responses is shown in Figure 4.12, and it makes clear that the lossy model is more accurate to represent the experimental response than the lossless model.

Figure 4.10 – Duty cycle step response of the GC-III prototype (yellow) versus PSIM simulation (red) of the model transfer function.

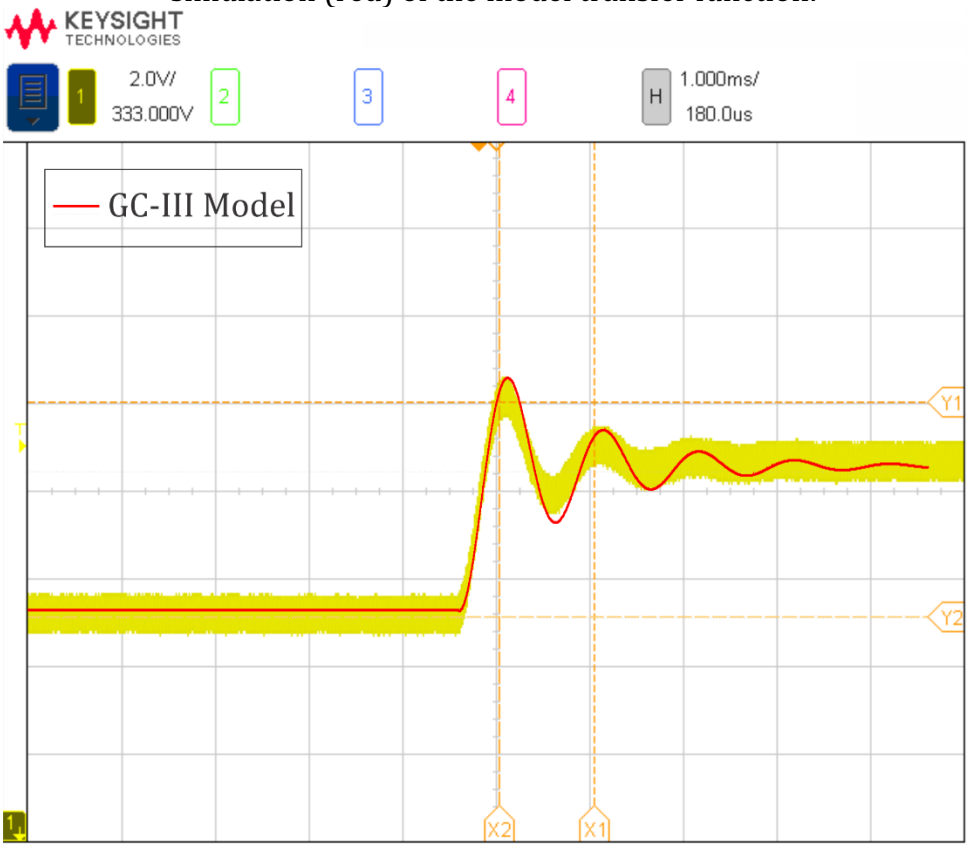

Source: Elaborated by the author.

Figure 4.11 – Switching model of the lossless Boost converter with gain cell III and the transfer function block with the lossy small-signal model

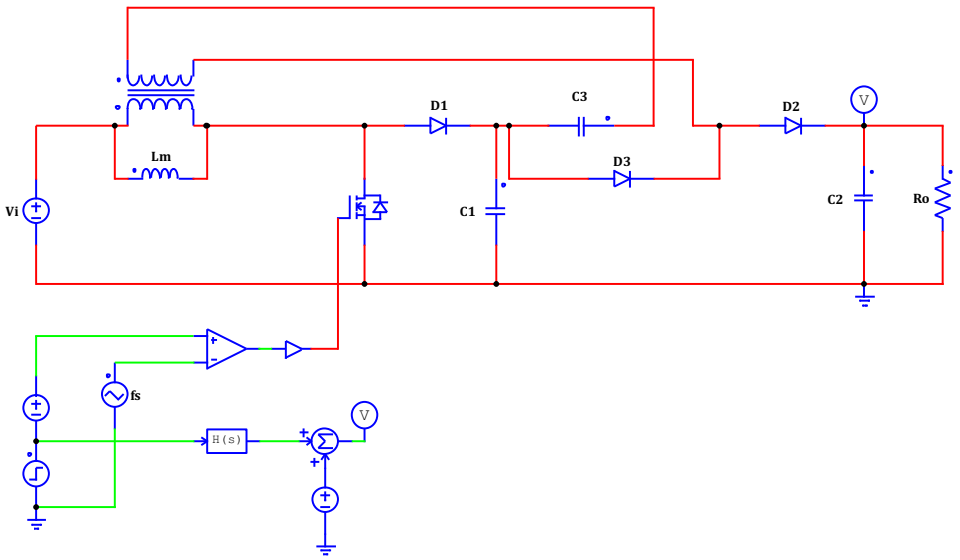

Source: Elaborated by the author.

Figure 4.12 – Duty cycle step response of the switching model of the lossless Boost converter with gain cell III (yellow line) and of the transfer function block with the lossy small-signal model (red line).

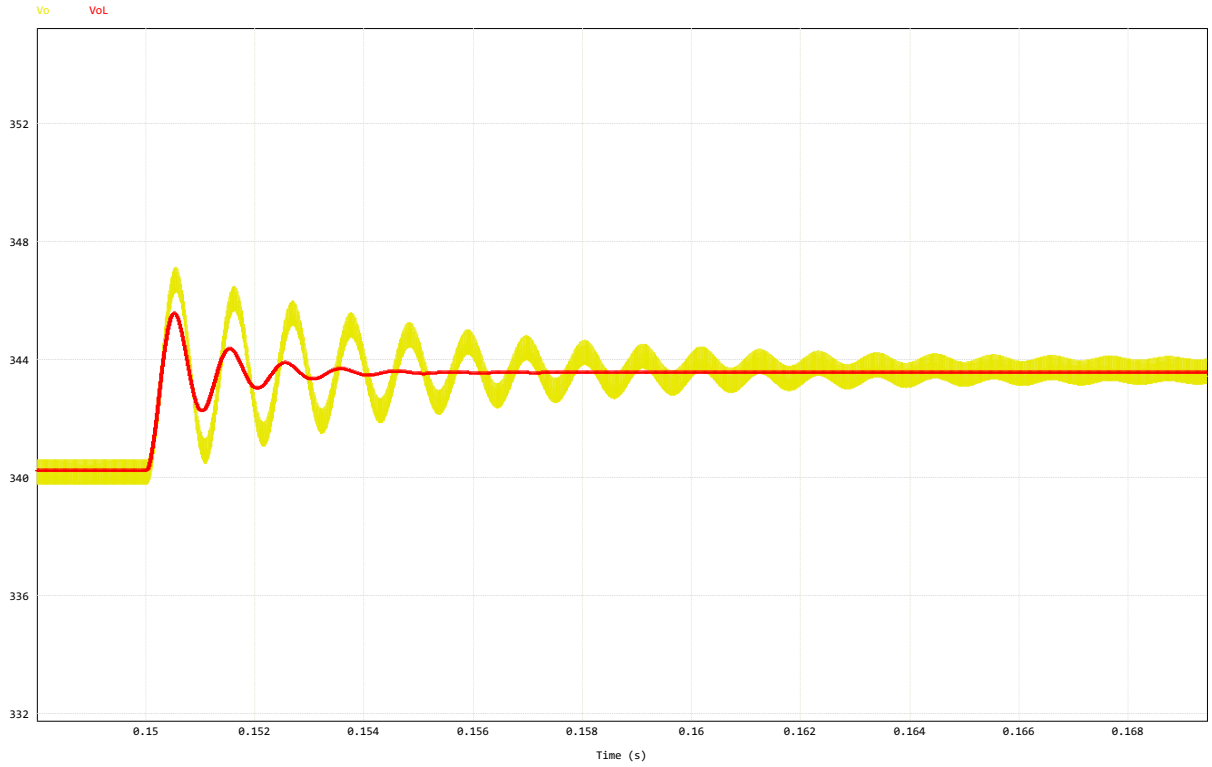

Source: Elaborated by the author.

Figure 4.13 – GC-III Bode diagram simulated versus the data obtained from the prototype experiment.

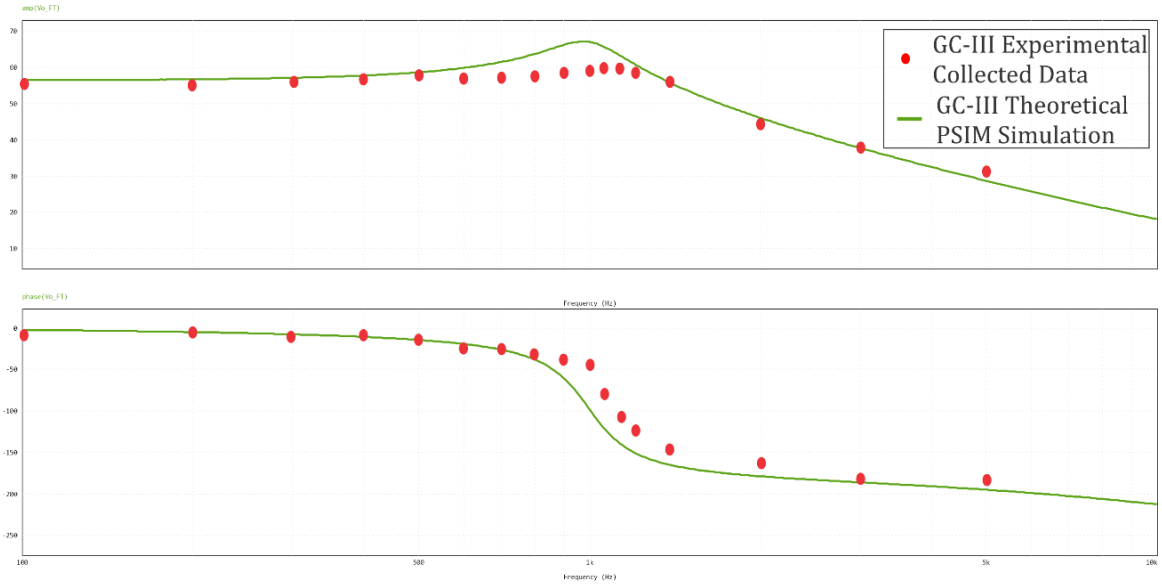

Source: Elaborated by the author.

Figure 4.13 shows the Bode plots of the prototype and the lossy model, displaying similar response to the GC-V result. The asymptotic behavior is very similar, with an attenuation in the resonant peak very likely because the losses estimation needs to be adjusted. The plot also shows that the prototype phase shift and resonant peak occur at higher frequencies than the model, and it indicates that the prototype has a slower response to changes in input frequency compared to the model. In other words, the prototype takes more time to reach its maximum phase shift and resonant peak compared to the model.

Figure 4.14 – GC-III Bode diagram lossy model (blue) versus ideal model (orange).

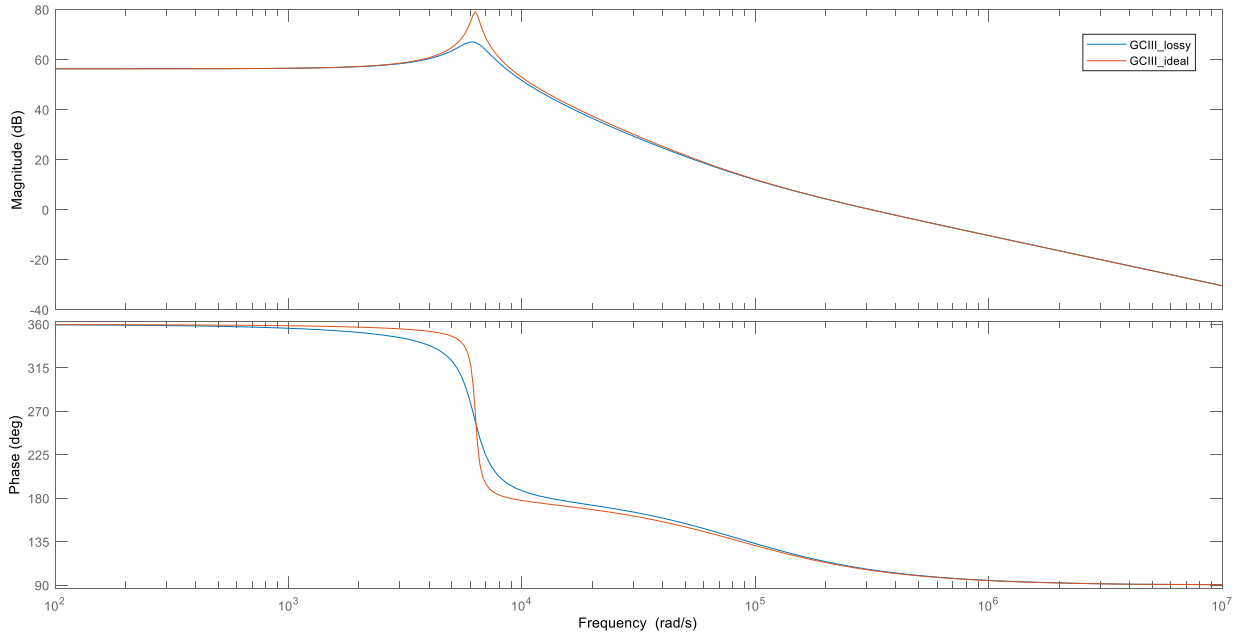

Source: Elaborated by the author.

The comparation between the ideal model versus the lossy model is shown in Figure 4.14, which keeps the same kind of response discrepancy as seen for the GC-V. Regarding the pole-zero map of Figure 4.15, again when comparing both lossy and ideal models it is clear that accounting parasitic components resulted in multiple poles and zeros in the left half-plane and one zero in the right half-plane over the real axis, while the lossless model shows just two symmetrical poles along the imaginary axis (conjugate complex poles) in the left half-plane and also one zero in the right half-plane over the real axis.

Figure 4.15 – Pole-zero map of GC-V lossy model (blue) versus ideal model (orange).

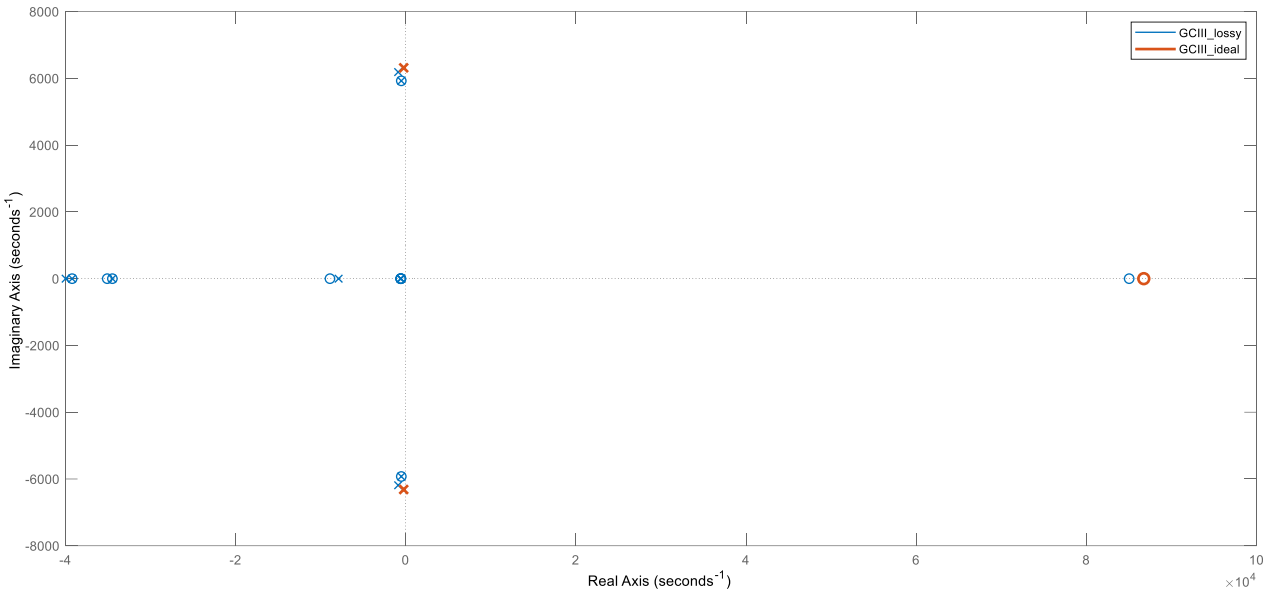

Source: Elaborated by the author.

4.4 GC-I EXPERIMENTAL RESULTS

The final test was conducted with the converter connected to the GC-I. The project for this configuration with a duty cycle of 60%, also following Appendix D equations and the parameters given in the previous section, expected to reach the maximum output voltage of 400 V with an input voltage of 33 V and a static gain of 12.1. The results shown in Table 4.7 demonstrated that the static gain prediction error is 2.8%. This gain cell was not tested in the expected maximum output voltage because the output diode used had a maximum voltage of 500 V and to reach the converter maximum output voltage it would be necessary to change this component since its voltage would get higher than the supported level. To maintain the prototype as projected, the maximum output voltage reached during testing was 176.5 V for an input voltage of 15 V.

Table 4.7 – GC-I prototype static gain test.

Duty cycle	$d = 0.6$
Output Voltage	$V_o = 400$ V*
Input Voltage	$V_i = 34$ V*
Static Gain	$M = 11.76$

**Projected values based in the static gain obtained in test with $V_i = 15$ V and a $V_o = 176.5$ V.*

Source: Elaborated by the author.

With the duty cycle increasing from 0.6 to 0.606 and an input voltage of 15 V, this step response test obtained the results shown in Figure 4.16. The yellow graph is printed from the oscilloscope connected to the prototype and the red wave form is from the lossy model. These results are the most accurate among the studied models, with the closer result to the prototype response. The lossless switching model of the Bost converter with gain cell I and the transfer function block with the lossy small-signal model already tested in this section are shown in Figure 4.17. Figure 4.18 shows the comparation between the lossless model and the lossy model transfer function step responses. The lossless model has a much higher overshoot and takes much longer to reach the steady state value.

Figure 4.16 – Duty cycle step response of the GC-I prototype (yellow) versus PSIM simulation (red) of the model transfer function.

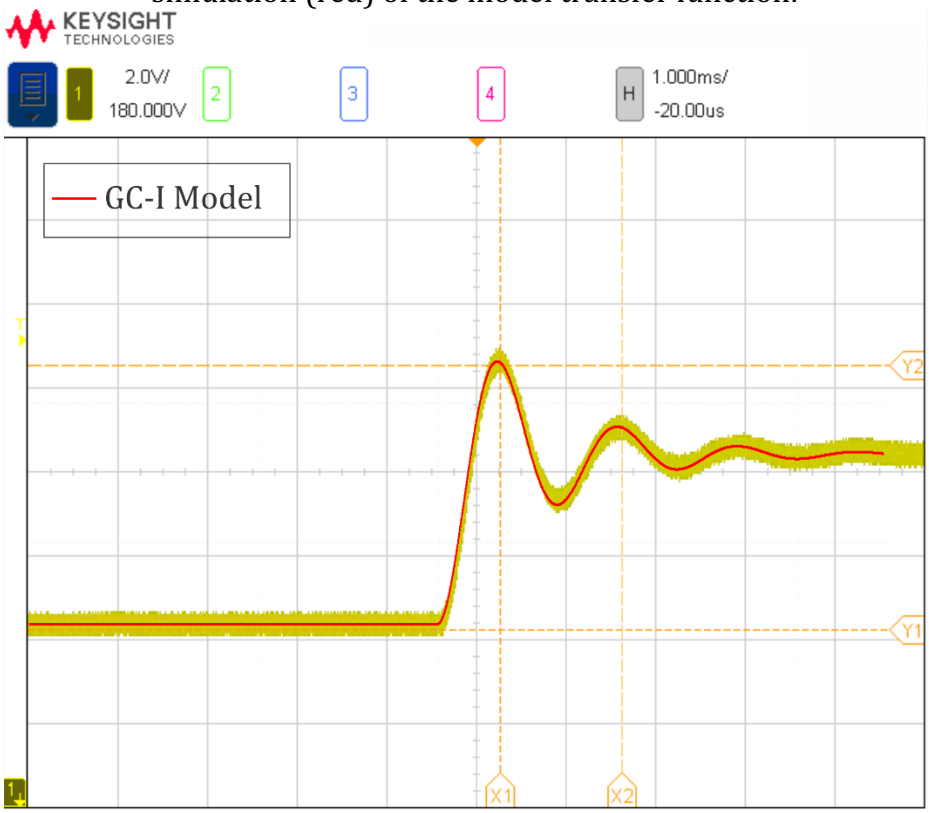

Source: Elaborated by the author.

Figure 4.17 – Switching model of the lossless Boost converter with gain cell I and the transfer function block with the lossy small-signal model.

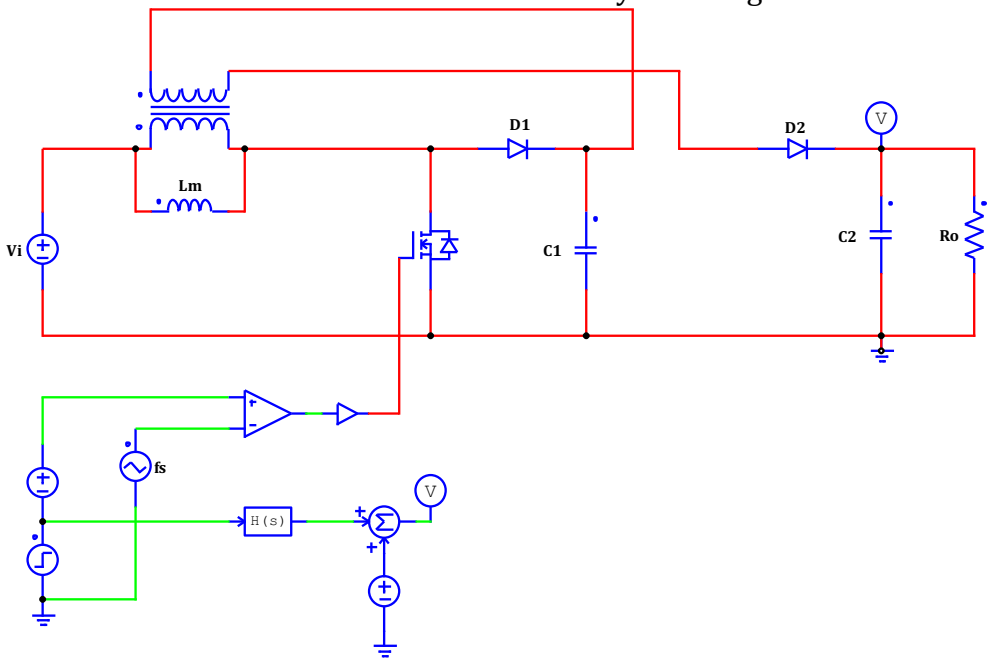

Source: Elaborated by the author.

Figure 4.18 – Duty cycle step response of the switching model of the lossless Boost converter with gain cell I (yellow line) and of the transfer function block with the lossy small-signal model (red line).

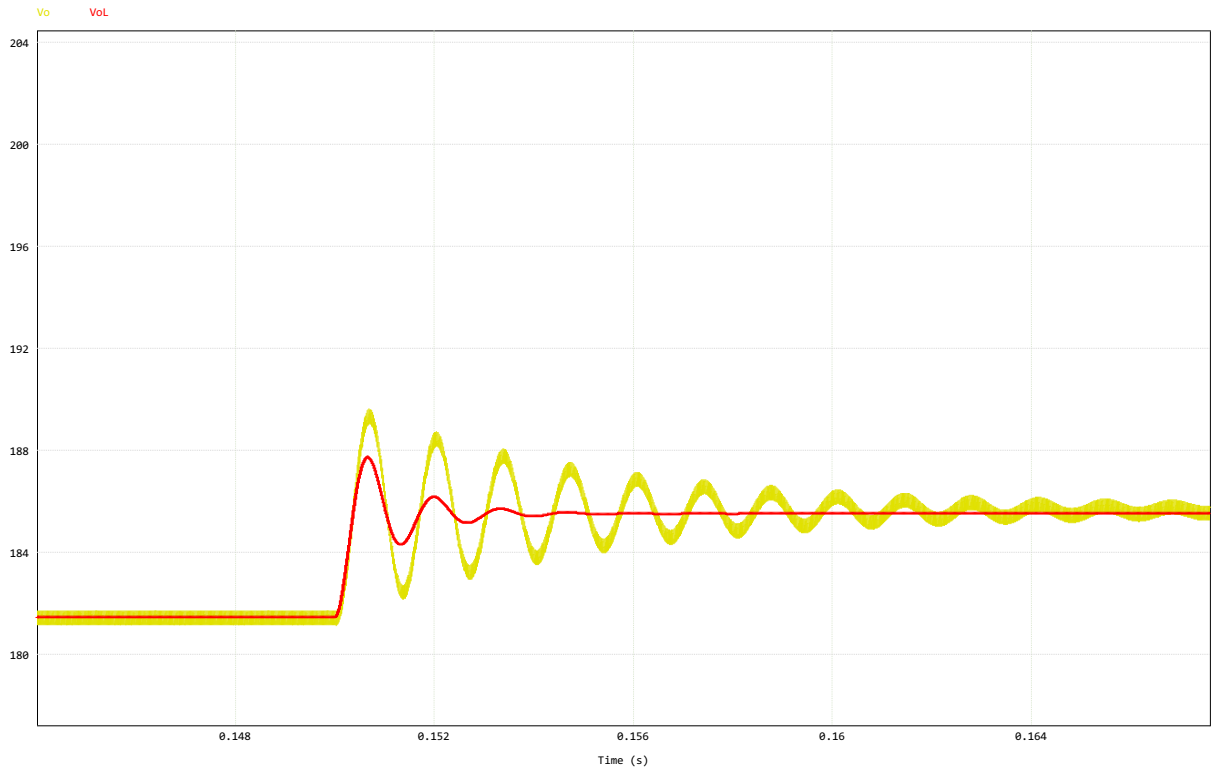

Source: Elaborated by the author.

As seen in Figure 4.19, the frequency response obtained with the prototype was very similar to the lossy model response. The model with the parasitic components represents more accurately the real response of the prototype than the ideal model, as shown in Figure 4.20. The ideal model presents an accentuated resonant peak, while the prototype shows a more damped curve, as the lossy model. The two systems have very similar magnitudes, besides the resonant peak, but different phases in the Bode diagram, and this can have important implications for the behavior and performance of these systems. The fact that the magnitudes are similar indicates that the systems have comparable gain characteristics. They may provide similar levels of amplification or attenuation to input signals across different frequencies.

On the other hand, different phase responses in general indicate that the systems have different time delay or phase shift behaviors at different frequencies. This can affect the timing and alignment of signals in the time domain. The phase response is crucial for analyzing the stability of control systems. Differences in phase can result in variations in transient response, settling time, and overall system behavior at different frequencies. So, since the lossy model represents similarly the frequency response of the prototype than the ideal model, it reproduces with more accuracy the real behavior of this converter.

Figure 4.19 – GC-I Bode diagram simulated versus the data obtained from the prototype experiment.

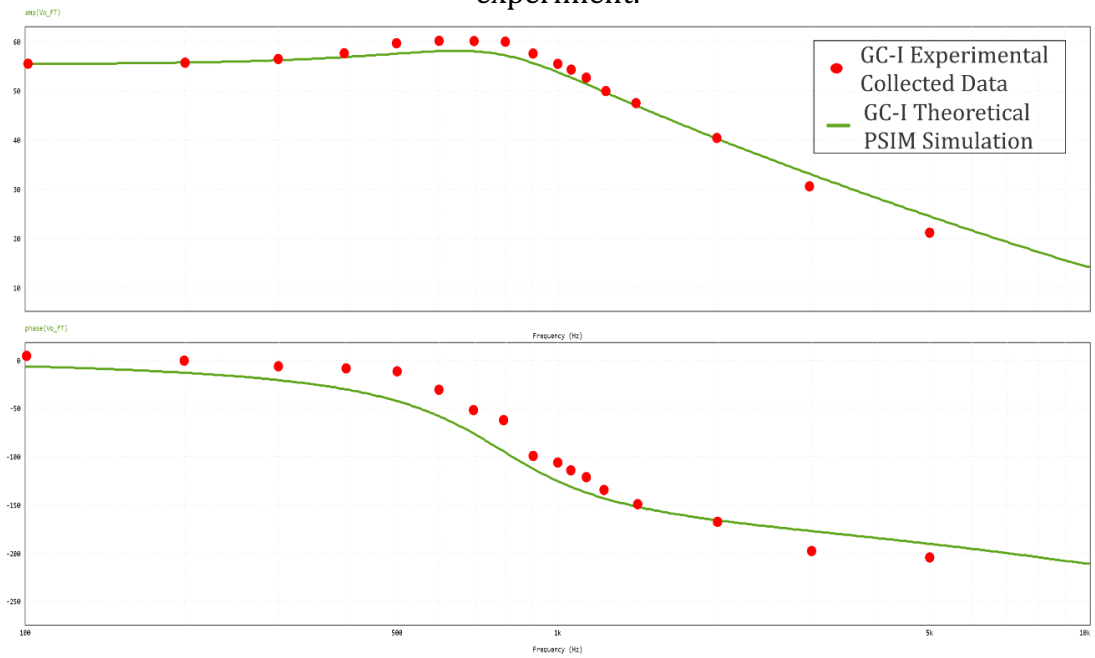

Source: Elaborated by the author.

Figure 4.20 – GC-I Bode diagram lossy model (blue) versus ideal model (orange.

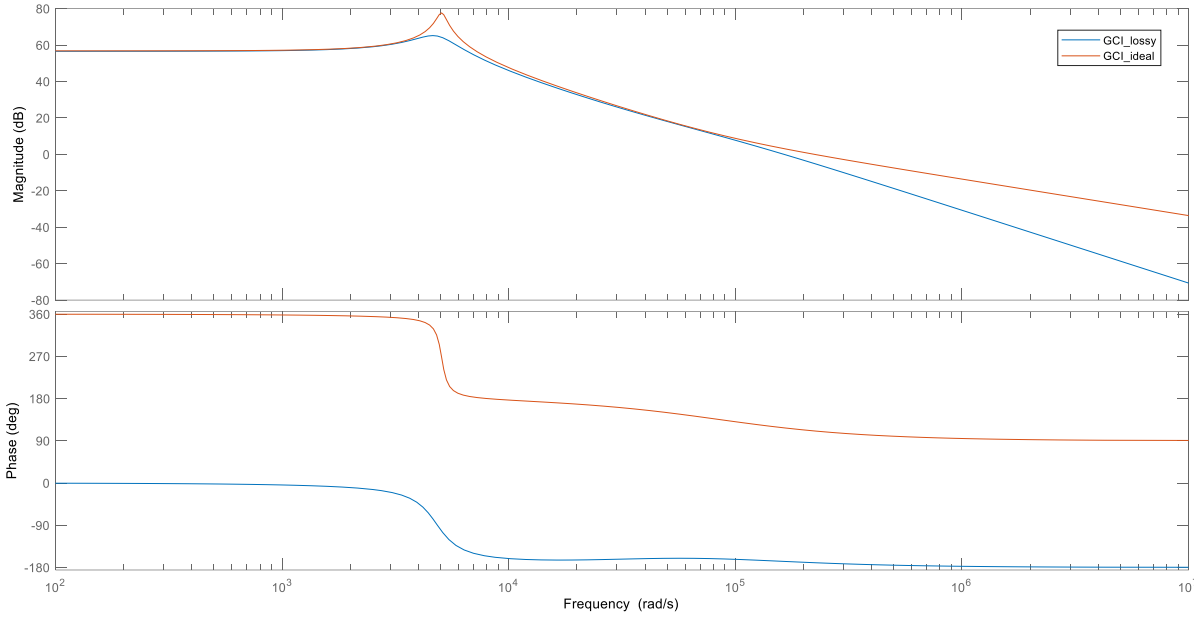

Source: Elaborated by the author.

Figure 4.21 shows the pole-zero map of both lossy model and ideal model. The lossy model presents two symmetrical poles along the imaginary axis (conjugate complex poles), one pole in the left half-plane over the real axis and one zero in the left half-plane over the real axis. Also, the ideal model has two symmetrical poles along the imaginary axis (conjugate complex poles), and one zero in the right half-plane over the real axis. Both configurations have poles in the left half-plane, which contributes to stability. However, the lossy model has an additional pole and zero in the left half-plane, potentially enhancing stability further and may offer better transient response characteristics as well. It can potentially lead to faster settling times and reduced overshoot. The presence of additional poles and zeros in the lossy model could also provide more flexibility for control system design and compensation, potentially leading to better robustness. Since the model should represent the real system within the control bandwidth, the effect of poles and zeros at high frequency, not accounted for by the model, can be disregarded as it does not impact the control design.

Figure 4.21 – Pole-zero map of GC-I lossy model (blue) versus ideal model (orange).

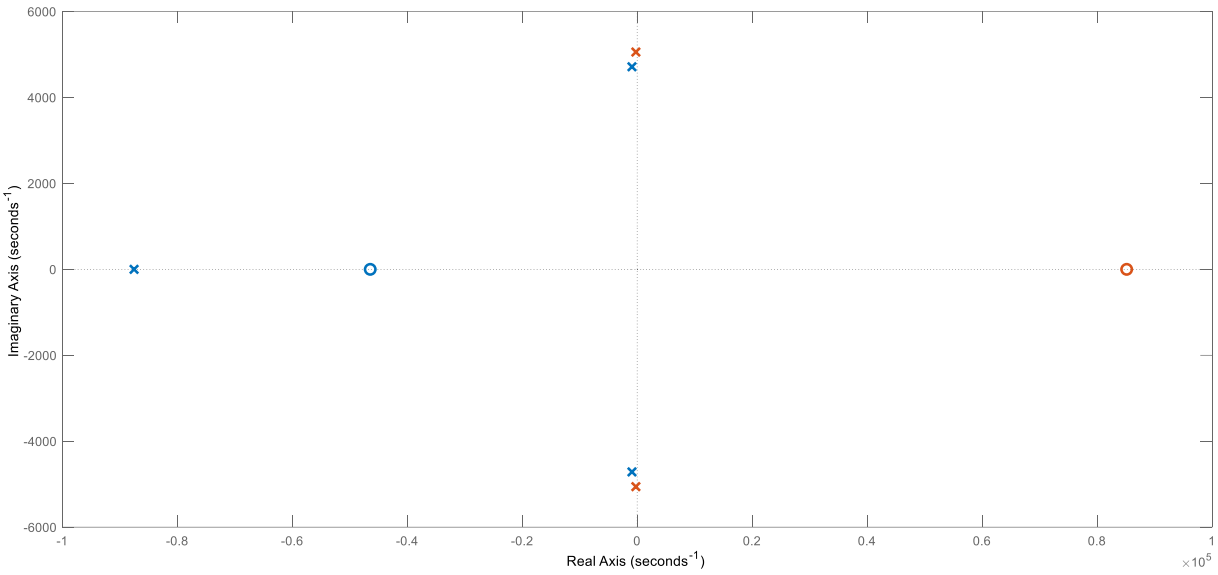

Source: Elaborated by the author.

4.5 CHAPTER CONCLUSIONS

In this chapter, the development and testing of the prototype of the gain cell converter were presented, aiming to validate the models developed in the previous chapters. The design methodology of the constructed converter was based on [9], and the component selection took into consideration that the same prototype would be used for the three studied gain cells with minor modifications tailored to each for testing purposes. The tests consisted of an initial performance test to assess the static gain of the converter, as well as tests for step response and frequency response.

The static gain test demonstrated that the estimated gains for each cell were accurate, as the prototype results exhibited errors of less than 7%, and in some cases, even approaching 2%. Subsequently, the step response and frequency response tests also yielded satisfactory results, although they pointed out the possibility of improvements in loss estimation.

While the developed models are much more accurate in representing the actual behavior of the converter than the ideal model (without losses), the prototype exhibited a more damped behavior than the model. This damping effect was possibly caused by the estimation of losses in the coupled inductor, and further in-depth studies to represent these losses should be pursued in the future, especially when dealing with higher-order

converters. The model used and developed in [5] demonstrated good behavior for lower-order transfer functions, but as the order of the transfer function increases, the result diverges further from the actual converter response.

5 CONCLUDING REMARKS

This document addressed an analysis of including parasitic components in the modeling of Boost converters with coupled inductor gain cells. With the goals outlined in the initial chapter of this thesis in mind, the subsequent chapters delved into the fundamental concepts necessary for understanding the modeling methodology of gain cell converters within the proposed configurations.

Chapter 2 examined the key elements that constitute a high-gain boost DC-DC converter with coupled inductor gain cells operating in continuous conduction mode in detail. An analysis of the modeling of an ideal boost converter was presented, along with the concept of a coupled inductor and its equivalent electrical model. Subsequently, the concept of a gain cell was addressed, and the three chosen configurations for this study were introduced: GC-I, GC-III, and GC-V. The modeling of the integrated boost converter with these cells was then discussed.

Chapter 3 addressed the most relevant parasitic components in this type of converter, presenting the concept of losses in the MOSFETs, diodes, capacitors, and coupled inductor. These losses were represented through equivalent models that were introduced into the models of gain cell converters under discussion. The inclusion of these elements resulted in more complex equations than those obtained in Chapter 2, yielding transfer functions of significantly higher order. The models were validated through simulations that compared the small-signal models obtained to switching models of these converters.

Chapter 4 introduced the prototype of the built boost DC-DC converter with coupled inductor gain cell, which was used to compare the results obtained from the developed models with the actual converter response. Step response and frequency response tests were conducted, and the obtained results support the thesis that including parasitic components in the modeling of high-gain boost converters generates more accurate models than ideal models.

Using more complex and accurate dynamic models for projecting a dc-dc converter could be recommended in some scenarios such as: when a detailed understanding of the converter's behavior is required, especially in complex operating conditions or under various loads and input voltage levels, common in research or development of cutting-edge technologies; for designing advanced control strategies, especially in applications

where tight regulation of output voltage or current is critical, since accurate models are essential for stability analysis and control loop tuning; in situations where precise prediction of transient responses – such as startup, shutdown, or load transients – is crucial, for ensuring the converter can handle rapid changes in operating conditions.

Also, for converters operating at high switching frequencies, where parasitic effects – such as parasitic capacitances, inductances, and electromagnetic interference – have a significant impact, accurate models are needed to account these effects. Another relevant scenario is when dealing with non-standard or advanced converter topologies, like multi-level converters, resonant converters, or soft-switching topologies. These often have complex operating modes that require accurate modeling. Research environments or when developing prototypes for new technologies, where a deep understanding of the converter's behavior is required to validate theoretical models and test new concepts, and in applications where safety is paramount, such as medical devices or aerospace systems, accurate modeling is essential to ensure the converter operates reliably under all conditions.

As a future work, it is suggested to delve further into the study of representing parasitic components in the modeling of DC-DC converters. Specifically, the representation of the coupled inductor's leakage inductance, along with the estimation of its copper and core losses, requires theoretical elaboration for the enhancement of loss models.

REFERENCES

[1] PAIXAO, J. L.; ABAIDE, A. R.; FILHO, P. G. A. Impact evaluation of the photovoltaic generation input on a concessionaire's network. **2018 Simposio Brasileiro de Sistemas Eletricos (SBSE)**, pp. 1-6, 2018.

[2] STILPEN, D.; CHENG, V. Solar photovoltaics in Brazil: A promising renewable energy market. **3rd International Renewable and Sustainable Energy Conference (IRSEC)**, pp. 1-5, 2015.

[3] ESTEVES, G.; LEITE, I. Solar Energy for Descentralized Energy Supply: a real option approach. **IEEE Xplore**, pp. 1-6, 2017.

[4] GORJIAN, S.; SHUKLA, A. **Photovoltaic Solar Energy Conversion Technologies, Applications and Environmental Impacts**. London: Academic Press, 2020.

[5] JIEB, Y.A.; HOSSAIN, E. **Photovoltaic Systems: Fundamentals and Applications**. Switzerland: Springer, 2021.

[6] KUMAR, L.A.; ALEXANDER, S.A.; RAJENDRAN, M. **Power Electronic Converters for Solar Photovoltaic Systems**. London: Academic Press, 2021.

[7] ERICKSON, R. W.; MAKSIMOVIC, D. **Fundamentals of Power Electronics**. 3. ed. Switzerland: Springer, 2020.

[8] SCHMITZ, Lenon. **Metodologia para Concepção de Conversores CC-CC de Alto Ganho Baseados em Topologias Básicas com Indutor Acoplado e Células Multiplicadoras de Tensão.** 2020. Tese (Doutorado em Engenharia Elétrica) – Departamento de Engenharia Elétrica e Eletrônica, Universidade Federal de Santa Catarina, Florianópolis, 2020.

[9] SCHMITZ, Lenon. **Conversores cc-cc não isolados de alto ganho e alto rendimento destinados a aplicações fotovoltaicas e baseados no conversor Boost com células de ganho.** 2015. Dissertação (Mestrado em Engenharia Elétrica) – Departamento de Engenharia Elétrica e Eletrônica, Universidade Federal de Santa Catarina, Florianópolis, 2015.

[10] SCHMITZ, L.; MARTINS, D. C.; COELHO, R. F. A Simple, Accurate Small-Signal Model of a Coupled-Inductor-Based DC-DC Converter Including the Leakage Inductance Effect. **IEEE Trans. Circuits Syst. II: Exp. Briefs**, v. 68, n. 7, p. 2533-2537, jul. 2021.

[11] ORAW, B.; RAJAPANDIAN, A. Large signal average model for an Extended Duty Ratio and conventional Buck. **Proc. IEEE 30th Int. Telecommun. Energy Conf**., pp. 1-8, 2008.

[12] KAZIMIERCZUK, M. K. **Pulse-Width Modulated DC–DC Power Converters**. 2. ed. West Sussex: John Wiley & Sons, 2016.

[13] DWARI, S.; et al. Dynamics characterization of coupled-inductor boost DC–DC converters. **Proc. IEEE Workshops Comput. Power Electron**., pp. 264-269, 2006.

[14] HORN, T. P. **Modelagem dinâmica de Conversores CC-CC elevadores de alto ganho.** 2018. Monografia (Graduação em Engenharia de Controle e Automação) – Departamento de Engenharia de Controle e Automação, Universidade Federal de Santa Catarina, Florianópolis, 2018.

[15] SCHMITZ, L.; MARTINS, D. C.; COELHO, R. F. Generalized high step-up dc-dc boost-based converter with gain cell. **IEEE Trans. Circuits Syst. I, Reg. Papers**, v. 64, n. 2, p. 480-493, fev. 2017.

[16] ZHU, B.; WANG, H.; VILATHGAMUWA, D. M. Single-switch high step-up boost converter based on a novel voltage multiplier. **IET Power Electronics**, vol. 12, n.14, pp. 3732-3738, nov. 2019.

[17] HONADIA, P.; BARRO, F.; SANE, M. Performance Analysis of a Boost Converter with Components Losses. **Energy and Power Engineering**, v.10, p. 399-413, 2018.

[18] MOHAN, N.; UNDELAND, T. M.; ROBBINS, W. P. **Power Electronics: Converters.** 2. ed. New York: John Wiley & Sons, 1995.

[19] FOROUZESH, M.; SIWAKOTI, Y. P.; GORJI, S. A.; BLAABJERG, F.; LEHMAN, B. Step-up dc-dc converters: a comprehensive review of voltage-boosting techniques, topologies, and applications. **IEEE Trans. Power Electron**., v. 32, n. 12, p. 9143-9178, dez. 2017.

[20] LIU, H.; HU, H.; WU, H.; XING, Y.; BATARSEH, I. Overview of high-step-up cou- pled-inductor boost converters. **IEEE J. Emerg. Sel. Topics Power Electron.**, v. 4, n. 2, p. 689-704, jun. 2016.

[21] MENESES, D.; BLAABJERG, F.; GARCIA, O.; COBOS, J. A. Review and comparison of step-up transformerless topologies for photovoltaic ac-module application. **IEEE Trans. Power Electron.**, v. 28, n. 6, p. 2649-2663, jun. 2013.

[22] LI, W.; HE, X. Review of nonisolated high-step-up dc/dc converters in photovoltaic grid- connected applications. **IEEE Trans. Ind. Electron.**, v. 58, n. 4, p. 1239-1250, abr. 2011.

[23] MAKSIMOVIC, D.; CUK, S. Switching converters with wide dc conversion range. **IEEE Trans. Power Electron.**, v. 6, n. 1, p. 151-157, jan. 1991.

[24] PRUDENTE, M.; PFISCHER, L. L.; EMMENDOERFER, G.; ROMANELI, E. F.; GULES, R. Voltage multiplier cells applied to non-isolated dc-dc converters. **IEEE Trans. Power Electron**., v. 23, n. 2, p. 871-887, mar. 2008.

[24] ISMAIL, E. H.; AL-SAFFAR, M. A.; SABZALI, A. J.; FARDOUN, A. A. A family of single-switch PWM converters with high step-up conversion ratio. **IEEE Trans. Circuits Syst. I, Reg. Papers**, v. 55, n. 4, p. 1159–1171, maio 2008.

[25] SALVADOR, M. A.; LAZZARIN, T. B.; COELHO, R. F. High step-up dc-dc converter with active switched-inductor and passive switched-capacitor networks. **IEEE Trans. Ind. Electron.**, v. 65, n. 7, p. 5644-5654, jul. 2018.

[26] DWARI, S.; JAYAWANT, S.; BEECHNER, T.; MILLER, S. K.; MATHEW, A.; CHEN, M.; RIEHL, J.; SUN, J. Dynamics characterization of coupled-inductor boost dc-dc converters. In: IEEE COMPEL, 2006, Troy. **Annals** […]. [S. l.: s. n.], 2007, p. 264-269.

[27] DAS, M.; AGARWAL, V. Generalized small signal modelling of coupled-indutor-based high-gain high-efficiency dc-dc converters. **IEEE Trans. Ind. App**., v. 53, n. 3, p. 2257- 2270, may 2017.

[28] D'AMICO,M. B.; GONZÁLEZ, S. A. Modelling and dynamical analysis of a dc-dc converter with coupled inductors. **Electrical Engineering**, v. 101, n. 1, p. 67-80, abr. 2019.

[29] CHEN, M.; LI, K.; IOINOVICI, A. Generation of a family of very high dc gain power electronics circuits based on switched-capacitor-inductor cells starting from a simple graph. **IEEE Trans. Circuits Syst. I, Reg. Papers**, v. 63, n. 12, p. 2381-2392, dez. 2016.

[30] ANDRADE, A. M. S. S.; MATTOS, E.; SCHUCH, L.; HEY, H. L.; MARTINS, M. L. S. Synthesis and comparative analysis of very high step-up dc-dc converters adopting coupled- inductor and voltage multipler cells. **IEEE Trans. Power Electron.**, v. 33, n. 7, p. 5880- 5897, jul. 2018.

[31] HSIEH, Y.-P.; CHEN, J.-F.; LIANG, T.-J.; YANG, L.-S. Novel high step-up dc-dc converter for distributed generation system. **IEEE Trans. Ind. Electron.**, v. 60, n. 4, p. 1473- 1482, abr. 2013.

[32] WAI, R.-J.; DUAN, R.-Y. High step-up converter with coupled-inductor. **IEEE Trans. Power Electron.**, v. 20, n. 5, p. 1025-1035, set. 2005.

[33] GU, B.; DOMINIC, J.; LAI, J.-S.; ZHAO, Z.; LIU, C. High boost ratio hybrid transformer dc-dc converter for photovoltaic module applications. In: IEEE APEC, 27., 2012, Orlando. **Annals** […]. [S. l.: s. n.], 2012, p. 598-606.

APPENDIX A – Operating Principle of Gain Cell Boost Converter in Continuous Conduction Mode (CCM)

According to [5], the gain cell converters studied in this thesis exhibit five distinct stages during their operation, with the exception of the Boost converter with gain cell I, which exhibits only four stages. For a more accurate analysis, the presence of a leakage inductor referenced to the primary winding of the ideal electrical model of the coupled inductor, as previously introduced in Chapter 2, will be considered. This inductor represents the leakage flux - a portion of the total flux that does not contribute to the voltage induction in the secondary winding. Furthermore, it will be assumed that all other passive and active components are ideal, and all capacitors are sufficiently large so that their voltages can be considered constant during the switching period. Figure A.1 illustrates the analyzed circuit, where the "GC" block represents a generic gain cell. When referring to gain cell diodes and capacitors, generically as D_{GC} and C_{GC}, notice that in the thesis models and prototype these components where called D_3, $D_{4,}C_3$ and C_4, respectively.

Figure A.1 – Switched model of the Gain Cell Boost Converter considering the leakage flux in the inductor coupling.

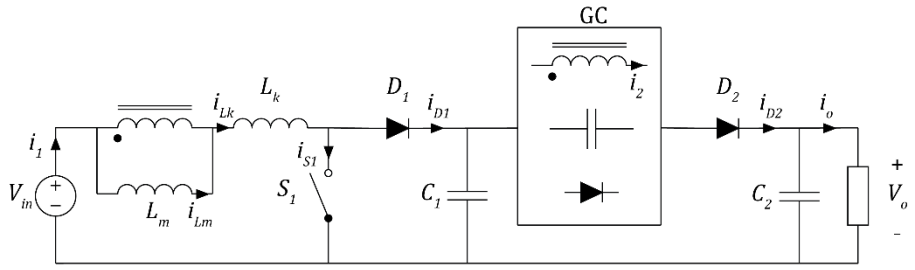

Source: Adapted from [3].

1st Operating stage ($t_0 < t < t_1$):

In this first stage, switch S_1 is in conduction, and the magnetizing inductor $L_m$and the leakage inductor L_k are storing energy from the input source V_i. Except for gain cell I, a portion of the energy from source V_i is transferred to the gain cell through the coupled inductor to charge its capacitors C_{GC1}. Diode D_2 is reverse-biased, and capacitor C_2 powers the load Ro. This stage, depicted in Figure 3.3 (a), comes to an end when switch S_1 is commanded to block.

2nd Operating stage ($t_1 < t < t_2$):

With the switch S_1 being turned off, diode D_1 starts conducting. Thus, the energy stored in inductor L_k is transferred to capacitor C_1. The gain cell remains in operation while the magnetizing inductor L_m continues to receive energy from source V_i and diode D_2 remains blocked. This stage ends when the current i_{Lk} becomes equal to the current i_{Lm}. For gain cell I, this stage is non-existent, as i_{Lk} is equal to i_{Lm} from the previous stage since, in this cell, there is no energy storage in capacitors. In other words, when S_1 is commanded to turn off, diode D_2 immediately becomes conductive.

3rd Operating stage ($t_2 < t < t_3$):

When the current i_{Lk} becomes equal to the current i_{Lm}, the current in the secondary winding of the coupled inductor, i_2, drops to zero. Diode D_2 becomes conductive. In this manner, the capacitors C_{GC1} of the gain cells, capacitor C_1, and the magnetizing inductor L_m, via the coupled inductor, start providing energy to capacitor C_2 and load R_o. Simultaneously, the energy stored in inductor L_k continues to be delivered to capacitor C_1 through diode D_1. This stage is completed when the energy stored in L_k is depleted, meaning when the current i_{Lk} becomes zero.

4th Operating stage ($t_3 < t < t_4$):

As the stored energy in L_k is depleted, diode D_1 is blocked. Capacitors C_{GC1}, capacitor C_1, and magnetizing inductor L_m continue to provide energy to capacitor C_2 and load R_o. This stage concludes when switch S_1 is commanded to conduct.

5th Operating stage ($t_4 < t < t_5$):

The final stage begins with the switch S_1 entering conduction. The input source V_i starts supplying energy to the leakage inductor L_k. Capacitors C_{GC1}, capacitor C_1, and magnetizing inductor L_m continue to provide energy to capacitor C_2 and load R_o. When i_{Lk} becomes equal to i_{Lm}, the current i_2 in the secondary winding of the coupled inductor cancels out and diode D_2 to become blocked. This marks the end of this operational stage.

Figure A.2 - Key waveforms of the Boost converter using gain cell (a) GC-III and GC-V and (b) GC-I.

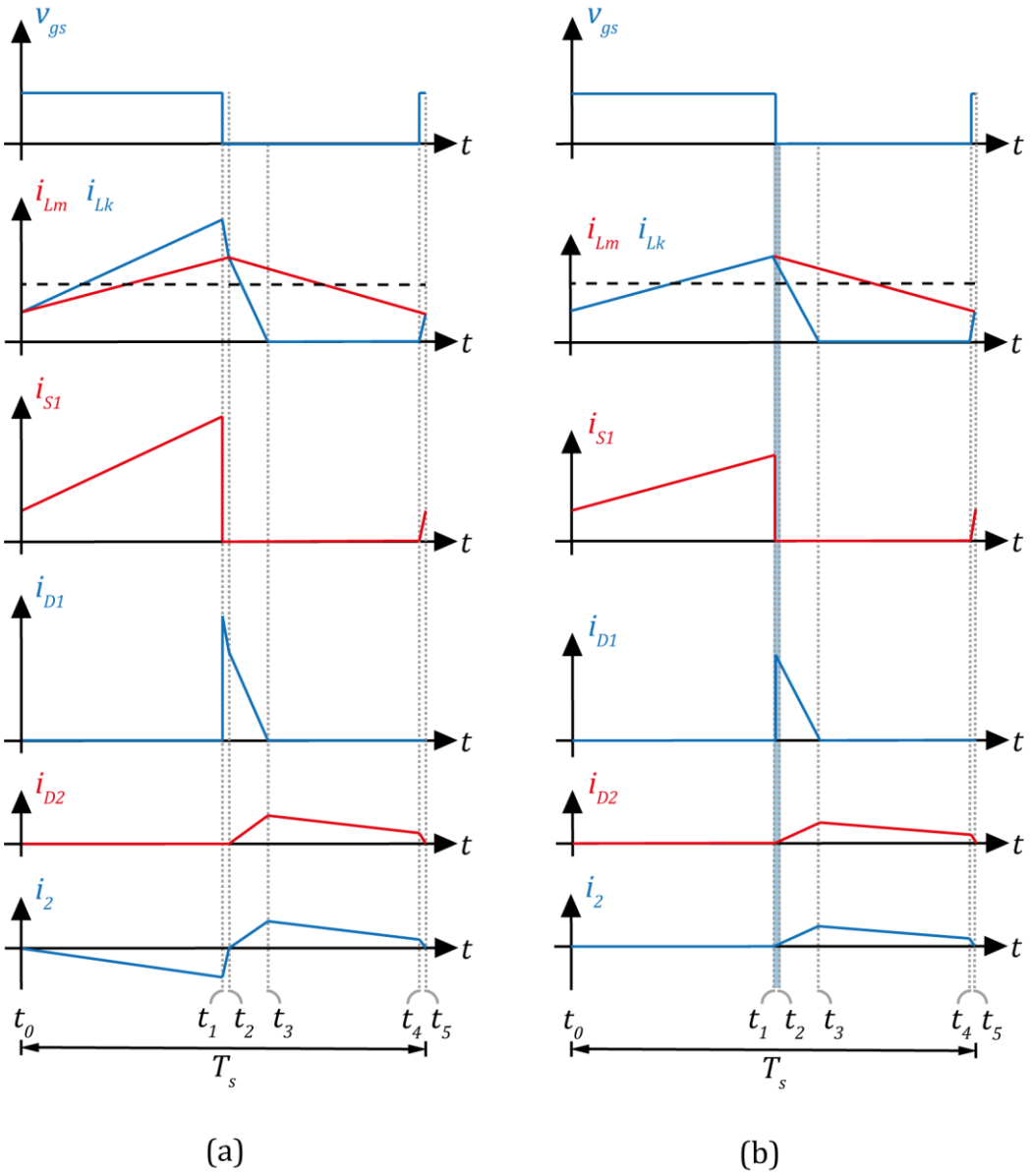

Source: Adapted from [5].

In Figure A.2 (a), the main waveforms are depicted, except for gain cell I, whose waveforms are illustrated in Figure A.2 (b), in which, the highlighted regions, illustrate the non-existent operating stages when compared to the waveforms in Figure A.2(a).

APPENDIX B – State Space Modeling Review

State space modeling is a mathematical technique widely used in control system analysis and design. It offers a compact representation of a system's dynamic behavior in terms of its internal states, inputs, and outputs. In the realm of DC-DC converters, state space modeling provides a detailed insight into the converter's transient response, stability, and overall performance. By representing the system's behavior in state space, engineers can apply advanced control techniques and optimize the converter's operation.

State Vector ($\boldsymbol{x}$): A column vector that contains the internal states of the system. Each element of the vector represents a state variable.

$$\boldsymbol{x} = \begin{bmatrix} x_1 \\ x_2 \\ \vdots \\ x_n \end{bmatrix} \tag{B.1}$$

Input Vector ($\boldsymbol{u}$): A column vector that contains the control inputs or disturbances applied to the system.

$$\boldsymbol{u} = \begin{bmatrix} u_1 \\ u_2 \\ \vdots \\ u_n \end{bmatrix} \tag{B.2}$$

Output Vector ($\boldsymbol{y}$): A column vector that contains the measured or observed outputs of the system.

$$\boldsymbol{y} = \begin{bmatrix} y_1 \\ y_2 \\ \vdots \\ y_n \end{bmatrix} \tag{B.3}$$

State Equations: The state equations describe how the states evolve over time. They are typically represented using the matrix equation:

$$\frac{d\boldsymbol{x}}{dt} = \boldsymbol{Ax} + \boldsymbol{Bu} \tag{B.4}$$

Where:

- $d\mathbf{x}/dt$ is the rate of change of the state vector $\boldsymbol{x}$, also represented as $\dot{\boldsymbol{x}}$;
- $\boldsymbol{A}$ is the state matrix:

$$\boldsymbol{A} = \begin{bmatrix} 1 & 0 & \cdots & 0 & 0 \\ 0 & 1 & \cdots & 0 & 0 \\ \vdots & \ddots & \ddots & 0 & 0 \\ 0 & 0 & \cdots & 1 & 0 \\ -a_0 & -a_1 & \cdots & -a_{n-2} & -a_{n-1} \end{bmatrix} \tag{B.5}$$

- $\boldsymbol{B}$ is the input matrix;

$$\boldsymbol{B} = \begin{bmatrix} 0 \\ 0 \\ \vdots \\ 0 \\ 1 \end{bmatrix} \tag{B.6}$$

- $\boldsymbol{u}$ is the input vector.

Output Equation: The output equation defines the relationship between the states and the measured outputs:

$$\boldsymbol{y} = \boldsymbol{Cx} + \boldsymbol{Du} \tag{B.7}$$

Where:

- $\boldsymbol{y}$ is the output vector,
- $\boldsymbol{C}$ is the output matrix;

$$\boldsymbol{C} = [c_0 \quad c_1 \quad \dots \quad c_{n-2} \quad c_{n-1}] \tag{B.8}$$

- $\boldsymbol{D}$ is the feedforward matrix.

$$\boldsymbol{D} = [d_0] \tag{B.9}$$

Average Model: After obtaining the state equations, their quasi-instantaneous average values are calculated over a switching period according to each operation stage, as seen in Chapter 2. The general formula for the average model can be written as:

$$\frac{d\langle \boldsymbol{x} \rangle}{dt} = \sum_{\boldsymbol{i=1}}^{\boldsymbol{N}} \langle \boldsymbol{h_i A_i} \rangle \langle \boldsymbol{x} \rangle + \sum_{\boldsymbol{i=1}}^{\boldsymbol{N}} \langle \boldsymbol{h_i B_i} \rangle \langle \boldsymbol{u} \rangle \tag{B.10}$$

For a two operating stage system it can be considered $\boldsymbol{A_1}$ and $\boldsymbol{B_1}$ as first operating stage equations, and $\boldsymbol{A_1}$ and $\boldsymbol{B_1}$, as second operating stage equations, and the validating function h_i as $h_1 = \langle s \rangle = d$ e $h_2 = 1 - \langle s \rangle = 1 - d$:

$$\sum_{\boldsymbol{i=1}}^{\boldsymbol{N}} \langle \boldsymbol{h_i A_i} \rangle = \langle \boldsymbol{h_1} \rangle \boldsymbol{A_1} + \langle \boldsymbol{h_2} \rangle \boldsymbol{A_2} \tag{B.11}$$

$$\sum_{\boldsymbol{i=1}}^{\boldsymbol{N}} \langle \boldsymbol{h_i B_i} \rangle = \langle \boldsymbol{h_1} \rangle \boldsymbol{B_1} + \langle \boldsymbol{h_2} \rangle \boldsymbol{B_2} \tag{B.12}$$

Example: *State Space Modeling of a Boost Converter operating in Continuous Conduction Mode (CCM).*

A simplified boost converter consists of an inductor (L) and its series resistance (R_L), a switch (controlled by the switching signal s), a diode (D), and an output capacitor (C), connected to a resistive output load (R_o). The objective is to model the converter's behavior in terms of inductor current (I_L) and output voltage (V_{out}). This example is very similar to the Boost converter example in Chapter 2, where are more details about operating stages.

Figure B.1 – Switching Model of a Boost Converter.

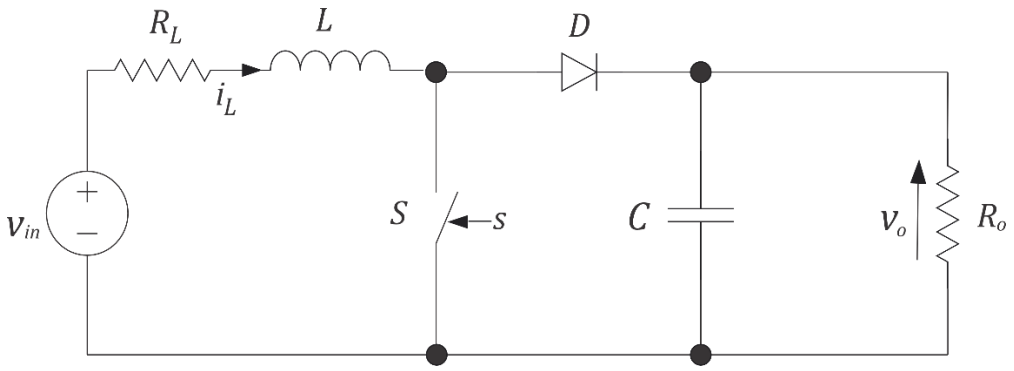

Source: Elaborated by the author.

States:

- *State 1 (x1):* Inductor current (i_L);

- *State 2 (x2):* Output voltage (v_o).

Inputs and Outputs:

- *Input (u):* input voltage (v_{in});

- *Output (y):* Output voltage (same as State 2).

State Equations: The state equations $\frac{dx}{dt} = \boldsymbol{Ax} + \boldsymbol{Bu}$ for the boost converter can be represented in matrix form as follows:

$$\frac{d\boldsymbol{x}}{dt} = \begin{bmatrix} -{}^{R_L}/_{L} & -{}^{(1-s)}/_{L} \\ -{}^{(1-s)}/_{C} & -{}^{1}/_{R_o C} \end{bmatrix} \begin{bmatrix} i_L \\ v_o \end{bmatrix} + \begin{bmatrix} {}^{1}/_{L} \\ 0 \end{bmatrix} [v_{in}] \tag{B.13}$$

Where:

$$s = \begin{cases} 1, \text{if the switch is on;} \\ 0, \text{if the switch is off.} \end{cases}$$

Output Equation: The output equation $\boldsymbol{y} = \boldsymbol{Cx} + \boldsymbol{Du}$ relates the output voltage to the states, being $\boldsymbol{D} = [0]$:

$$\boldsymbol{y} = [0 \quad 1] \begin{bmatrix} i_L \\ v_o \end{bmatrix}. \tag{B.14}$$

Average Model: After obtaining the state equations, it is possible to write its quasi-instantaneous average values:

$$\frac{d\langle \boldsymbol{x} \rangle}{dt} = \begin{bmatrix} -{}^{R_L}/_{L} & -{}^{(1-d)}/_{L} \\ -{}^{(1-d)}/_{C} & -{}^{1}/_{R_o C} \end{bmatrix} \begin{bmatrix} \langle i_L \rangle \\ \langle v_o \rangle \end{bmatrix} + \begin{bmatrix} {}^{1}/_{L} \\ 0 \end{bmatrix} [\langle v_{in} \rangle] \tag{B.15}$$

$$\langle \boldsymbol{y} \rangle = [0 \quad 1] \begin{bmatrix} \langle i_L \rangle \\ \langle v_o \rangle \end{bmatrix}. \tag{B.16}$$

Where *d* represents the duty cycle signal of the converter.

State space modeling using matrices allows us to describe and analyze the behavior of a boost converter in a concise and systematic manner. This example illustrates how state space modeling is a powerful tool in the field of power electronics, enabling engineers to design and optimize DC-DC converters for various applications.

APPENDIX C – Linearization of a Nonlinear System via Taylor Series Expansion

Linearization using the Taylor expansion is a common technique to approximate the behavior of a nonlinear system around an equilibrium point. This process involves representing the nonlinear state space model as a linear approximation using matrices.

Nonlinear State Space Average Model: Start the linearization with the given nonlinear state space average model, which can be represented in the form differential equation as follows:

$$\langle \dot{\boldsymbol{x}} \rangle = \boldsymbol{f}(\langle \boldsymbol{x} \rangle, \langle \boldsymbol{u} \rangle) \tag{C.1}$$

$$\langle \boldsymbol{y} \rangle = \boldsymbol{g}(\langle \boldsymbol{x} \rangle, \langle \boldsymbol{u} \rangle) \tag{C.2}$$

Where:

- $\langle \boldsymbol{x} \rangle$ is the state vector.

- $\langle \boldsymbol{u} \rangle$ is the input vector.

- $\langle \dot{\boldsymbol{x}} \rangle$ represents the time derivative of $\boldsymbol{x}$.

- $\langle \boldsymbol{y} \rangle$ is the output vector.

- $\boldsymbol{f}$ is a vector function that describes the dynamics of the system.

- $\boldsymbol{g}$ is a vector function that relates the states to the output.

Equilibrium Point: Identify an operating point $(\langle x_0 \rangle, \langle y_0 \rangle)$ where the system is in equilibrium $(\langle \dot{\boldsymbol{x}} \rangle = \boldsymbol{0})$. This is the point around which you want to linearize the system.

Perturbations: Introduce small perturbations Δx and Δu around the equilibrium point:

$$\langle x \rangle = \langle x_0 \rangle + \Delta x \tag{C.3}$$

$$\langle u \rangle = \langle u_0 \rangle + \Delta u \tag{C.4}$$

Taylor Expansion: Apply the Taylor expansion to the nonlinear functions $\boldsymbol{f}(\langle \boldsymbol{x} \rangle, \langle \boldsymbol{u} \rangle)$ and $\boldsymbol{g}(\langle \boldsymbol{x} \rangle, \langle \boldsymbol{u} \rangle)$ to obtain their linear approximations in terms of perturbations:

$$\boldsymbol{f}(\langle \boldsymbol{x} \rangle, \langle \boldsymbol{u} \rangle) \approx \boldsymbol{f}(\langle x_0 \rangle, \langle u_0 \rangle) + \left.\frac{\partial \langle \boldsymbol{f} \rangle}{\partial \langle \boldsymbol{x} \rangle}\right|_{\langle x_0 \rangle \langle, u_0 \rangle} \Delta \boldsymbol{x} + \left.\frac{\partial \langle \boldsymbol{f} \rangle}{\partial \langle \boldsymbol{u} \rangle}\right|_{\langle x_0 \rangle, \langle u_0 \rangle} \Delta \boldsymbol{u} \tag{C.5}$$

$$\boldsymbol{g}(\langle \boldsymbol{x} \rangle, \langle \boldsymbol{u} \rangle) \approx \boldsymbol{g}(\langle x_0 \rangle, \langle u_0 \rangle) + \left.\frac{\partial \langle \boldsymbol{g} \rangle}{\partial \langle \boldsymbol{x} \rangle}\right|_{\langle x_0 \rangle, \langle u_0 \rangle} \Delta \boldsymbol{x} + \left.\frac{\partial \langle \boldsymbol{g} \rangle}{\partial \langle \boldsymbol{u} \rangle}\right|_{\langle x_0 \rangle, \langle u_0 \rangle} \Delta \boldsymbol{u} \tag{C.6}$$

Linearized State Equations: Substitute the linear approximations into the original state space equations to obtain the linearized state space model:

$$\Delta \dot{\boldsymbol{x}} = \left.\frac{\partial \langle \boldsymbol{f} \rangle}{\partial \langle \boldsymbol{x} \rangle}\right|_{\langle x_0 \rangle, \langle u_0 \rangle} \Delta \boldsymbol{x} + \left.\frac{\partial \langle \boldsymbol{f} \rangle}{\partial \langle \boldsymbol{u} \rangle}\right|_{\langle x_0 \rangle, \langle u_0 \rangle} \Delta \boldsymbol{u} \tag{C.7}$$

$$\Delta \boldsymbol{y} = \left.\frac{\partial \langle \boldsymbol{g} \rangle}{\partial \langle \boldsymbol{x} \rangle}\right|_{\langle x_0 \rangle, \langle u_0 \rangle} \Delta \boldsymbol{x} + \left.\frac{\partial \langle \boldsymbol{g} \rangle}{\partial \langle \boldsymbol{u} \rangle}\right|_{\langle x_0 \rangle, \langle u_0 \rangle} \Delta \boldsymbol{u} \tag{C.7}$$

Jacobian Matrices: The matrices that appear in the linearized equations are called Jacobian matrices, as follows:

$$\boldsymbol{A} = \left.\frac{\partial \langle \boldsymbol{f} \rangle}{\partial \langle \boldsymbol{x} \rangle}\right|_{\langle x_0 \rangle, \langle u_0 \rangle} \tag{C.8}$$

$$\boldsymbol{B} = \left.\frac{\partial \langle \boldsymbol{f} \rangle}{\partial \langle \boldsymbol{u} \rangle}\right|_{\langle x_0 \rangle, \langle u_0 \rangle} \tag{C.9}$$

$$\boldsymbol{C} = \left.\frac{\partial \langle \boldsymbol{g} \rangle}{\partial \langle \boldsymbol{x} \rangle}\right|_{\langle x_0 \rangle, \langle u_0 \rangle} \tag{C.10}$$

$$\boldsymbol{D} = \left.\frac{\partial \langle \boldsymbol{g} \rangle}{\partial \langle \boldsymbol{u} \rangle}\right|_{\langle x_0 \rangle, \langle u_0 \rangle} \tag{C.11}$$

Linearized State Space Model: The linearized state space model can now be expressed in matrix form:

$$\Delta \dot{\boldsymbol{x}} = \boldsymbol{A} \Delta \boldsymbol{x} + \boldsymbol{B} \Delta \boldsymbol{u} \tag{C.12}$$

$$\Delta \boldsymbol{y} = \boldsymbol{C} \Delta \boldsymbol{x} + \boldsymbol{D} \Delta \boldsymbol{u} \tag{C.13}$$

Small-Signal Model: Analyze the linearized state space model to gain insights into the behavior of the system around the equilibrium point. This approximation is valid as long as the perturbations remain small, and this is the reason this is called *small-signal model*.

Transfer Function: With the matrices **A**, **B**, **C**, and **D** obtained in the small-signal model plus the identity matrix **I**, and knowing that s is here the Laplace variable, the equation below is used to obtain the transfer function:

$$\vec{Y}(s) = \boldsymbol{C}(s\boldsymbol{I} - \boldsymbol{A})^{-1}\boldsymbol{B}\vec{U}(s) + \boldsymbol{D}\vec{U}(s) \tag{C.14}$$

Example: *Linearize a Boost Converter.*

Average Model: In this example is illustrate how to linearize the state space model of a boost converter using Jacobian matrices. Consider the same converter seen in Figure B.1. From the Appendix B, it is known the converter average model:

$$\frac{d\langle \boldsymbol{x}\rangle}{dt} = \begin{bmatrix} -{}^{R_L}/_{L} & -{}^{(1-d)}/_{L} \\ -{}^{(1-d)}/_{C} & -{}^{1}/_{R_o C} \end{bmatrix}\begin{bmatrix}\langle i_L\rangle \\ \langle v_o\rangle\end{bmatrix} + \begin{bmatrix}{}^{1}/_{L} \\ 0\end{bmatrix}[\langle v_{in}\rangle] \tag{C.15}$$

$$\langle \boldsymbol{y}\rangle = [0 \quad 1]\begin{bmatrix}\langle i_L\rangle \\ \langle v_o\rangle\end{bmatrix}. \tag{C.16}$$

Vector-valued functions: The average model can be rewritten in the form of vector-valued functions $\langle \boldsymbol{f}\rangle$ and $\langle \boldsymbol{g}\rangle$:

$$\langle \boldsymbol{f}\rangle = \begin{bmatrix} \frac{1}{L}\cdot(\langle v_{in}\rangle - R_L\langle i_L\rangle - (1-d)\langle v_o\rangle) \\ \frac{1}{C}\cdot((1-d)\langle i_L\rangle - \frac{\langle v_o\rangle}{R_o}) \end{bmatrix} \tag{C.16}$$

$$\langle \boldsymbol{g}\rangle = [\langle v_o\rangle] \tag{C.17}$$

Operating Point: The operating point is defined as $\frac{d\langle \boldsymbol{f}\rangle}{dt} = 0$:

$$\begin{bmatrix}0\\0\end{bmatrix} = \begin{bmatrix} \frac{1}{L}\cdot(V_{in} - R_L I_L - (1-D)V_o) \\ \frac{1}{C}\cdot((1-D)I_L - \frac{V_o}{R_o}) \end{bmatrix} \tag{C.18}$$

Resulting in the operating points:

$$I_L = \frac{V_{in}}{R_L + (1-D)^2 R_o}, \tag{C.19}$$

$$V_o = \frac{V_{in}(1-D)R_o}{R_L + (1-D)^2 R_o}, \tag{C.20}$$

so the small perturbations are going to be introduced around this point.

Jacobian Matrices: The Jacobian matrices in respect of $\langle i_L \rangle, \langle v_o \rangle, \langle v_{in} \rangle \; and \; d$ are given by:

$$\boldsymbol{A} = \begin{bmatrix} -{}^{R_L}/_{L} & -{}^{(1-D)}/_{L} \\ -{}^{(1-D)}/_{C} & -{}^{1}/_{R_o C} \end{bmatrix} \tag{C.21}$$

$$\boldsymbol{B} = \begin{bmatrix} {}^{V_o}/_{L} & {}^{1}/_{L} \\ -{}^{I_L}/_{C} & 0 \end{bmatrix} \tag{C.22}$$

$$\boldsymbol{C} = [0 \quad 1] \tag{C.23}$$

$$\boldsymbol{D} = [0 \quad 0] \tag{C.24}$$

Linearized State Equations: The linearized state equations become:

$$\frac{d}{dt}\begin{bmatrix} \Delta i_L \\ \Delta v_o \end{bmatrix} = \begin{bmatrix} -{}^{R_L}/_{L} & -{}^{(1-D)}/_{L} \\ -{}^{(1-D)}/_{C} & -{}^{1}/_{R_o C} \end{bmatrix}\begin{bmatrix} \Delta i_L \\ \Delta v_o \end{bmatrix} + \begin{bmatrix} {}^{V_o}/_{L} & {}^{1}/_{L} \\ -{}^{I_L}/_{C} & 0 \end{bmatrix}\begin{bmatrix} \Delta d \\ \Delta v_{in} \end{bmatrix} \tag{C.25}$$

$$\langle \Delta v_o \rangle = [0 \quad 1]\begin{bmatrix} \Delta i_L \\ \Delta v_o \end{bmatrix} + [0 \quad 0]\begin{bmatrix} \Delta d \\ \Delta v_{in} \end{bmatrix} \tag{C.26}$$

Using Jacobian matrices, it is possible to successfully linearize the boost converter around a steady-state operating point. The resulting matrices **A** and **B** provide valuable insights into the local behavior of the system and are crucial for designing control strategies to stabilize or optimize the converter's performance.

Transfer Function: The transfer function, $G(s) = {}^{\vec{Y}(s)}/_{\vec{U}(s)}$, is the Laplace transform of the output over the Laplace transform of the input, representing the relationship between the output and input by solving the equation C.X, resulting in:

$$G(s) = {}^{\vec{Y}(s)}/_{\vec{U}(s)} = \begin{bmatrix} \frac{\widetilde{V_o}(s)}{\widetilde{D}(s)} & \frac{\widetilde{V_o}(s)}{\widetilde{V_{in}}(s)} \end{bmatrix} \tag{C.27}$$

$$G(s) = \begin{bmatrix} \frac{s + \frac{R_L}{L} + \frac{(1-D)V_o}{LI_L}}{LCs^2 + \left(R_L C + \frac{L}{R_L}\right)s + (1-D)^2 + \frac{R_L}{R_o}} & \frac{(1-D)}{LCs^2 + \left(R_L C + \frac{L}{R_L}\right)s + (1-D)^2 + \frac{R_L}{R_o}} \end{bmatrix} \tag{C.28}$$

This is the transfer function relates the output to the input in the Laplace domain. By applying the Laplace transform and using the linearized state space model, it is derived

the transfer function of the boost converter. This transfer function, $G(s)$, captures the converter's dynamic behavior and is a valuable tool for analyzing its response and designing control systems.

APPENDIX D – Gain Cell Boost Converter: Power Stage Design Equations

The following equations were developed in [5], consider the operating stages and waveforms of Appendix A and assume negligible leakage inductance, rendering the 2nd and 5th stages negligible as well. Thus, only the 1st, 3rd, and 4th stages will be considered, as depicted in Figure D.1, where the times t_c and t_x are defined by (D.1) and (D.2), respectively.

$$t_c \triangleq DT_s \tag{D.1}$$

$$t_x \triangleq D_x T_s \tag{D.2}$$

Figure D.1 - Waveforms of currents i_{Lm}, i_{Lk}, and i_2 disregarding the 2nd and 5th stages.

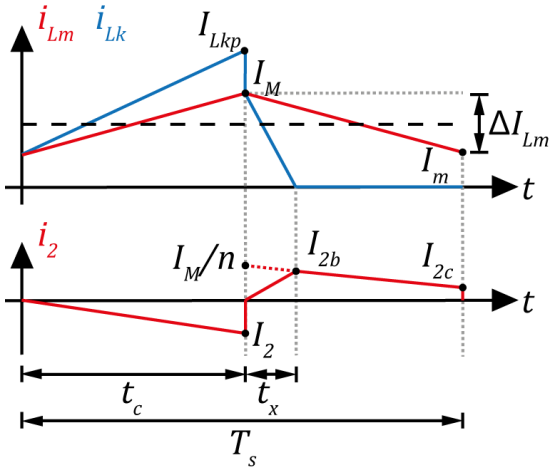

Source: Adapted from [5].

Current in the magnetizing inductor L_m:

The equation that defines the average value of the current i_{Lm} is (D.3):

$$I_{Lm} = [M - (a - b)n]I_o \tag{D.3}$$

The ripple in the current of inductor L_m can be determined through the volt-ampere relationship of the inductor:

$$\Delta I_{Lm} = \frac{DV_i}{L_m f_s} \tag{D.4}$$

Using (3.4), one can express the maximum value (D.5) and the minimum value (D.6) of the current i_{Lm}:

$$I_M = I_{Lm} + \frac{\Delta I_{Lm}}{2} = [M - (a-b)n]I_o + \frac{DV_i}{2L_m f_s} \tag{D.5}$$

$$I_m = I_{Lm} - \frac{\Delta I_{Lm}}{2} = [M - (a-b)n]I_o - \frac{DV_i}{2L_m f_s} \tag{D.6}$$

Average value of the currents in the diodes:

Since the average value of the current in any capacitor is equal to zero, it is observed that the average values of the currents in diodes D_1 and D_2 are equal to the average value of the output current io, as will be the case for any diode D_{GC} present in a gain cell. When referring to gain cell diodes and capacitors, generically as D_{GC} and C_{GC}, notice that in the thesis models and prototype these components where called D_3, $D_{4,}C_3$ and C_4, respectively. Therefore:

$$I_{D1} = I_{D2} = I_{Dcg} = I_o \tag{D.7}$$

Conduction time t_x of diode D1:

By knowing the average value of the current in diode D_1, it is possible to determine its conduction time t_x, as illustrated in Figure D.1, given that the peak value of the current in this diode is equal to the maximum value of the magnetizing current. Thus:

$$I_o = \frac{1}{T_s}\int_0^{t_x} i_{Lk}(t)\,dt = \frac{1}{T_s}\frac{I_M D_x T_s}{2} \tag{D.8}$$

$$D_x = \frac{2I_o}{I_M} \tag{D.9}$$

Current in switch S_1:

Analyzing the switching model of the gain cell Boost converter, such as the illustrated in A.1, it is known that:

$$D_x = \frac{2I_o}{I_M} \tag{D.9}$$

$$i_{S1} = i_{Lk} - i_{D1} \tag{D.10}$$

Therefore, since the average values of this currents are known, the average value of S_1 is:

$$i_{S1} = (M-1)I_o \tag{D.11}$$

Current in the leakage inductor L_k:

The average value of the current in L_k is:

$$i_{Lk} = I_i = MI_o \tag{D.12}$$

The peak value of the current in inductor L_k can be obtained through the calculation of the average value of the current in switch S_1:

$$i_{S1} = \frac{1}{T_s}\int_0^{t_c} i_{Lk}(t)\,dt = \frac{\left(I_m + I_{Lkp}\right)D}{2} \tag{D.13}$$

Substituting (D.11) into (D.13) and isolating I_{Lkp} yields (D.14).

$$I_{Lkp} = \frac{2(M-1)I_o}{D} - I_m \tag{D.14}$$

Current i_2 in the secondary winding of the coupled inductor:

The average value of the current in the secondary winding of the coupled inductor is given by:

$$I_2 = (b-a)I_o \tag{D.15}$$

Analyzing the figure D.1 and rewriting the known equation $i_{Lm} = i_1 + ni_2$ to isolate i_2:

$$i_2 = \frac{i_{Lm} - i_{Lk}}{n} \tag{D.16}$$

$$I_{2a} = i_2(t_c) = \frac{i_{Lm}(t_c) - i_{Lk}(t_c)}{n} = \frac{I_M - I_{Lkp}}{n} \tag{D.17}$$

Thus, substituting (D.14) into (D.17):

$$I_{2a} = \frac{2I_{Lm}}{n} - \frac{2(M-1)I_o}{nD} \tag{D.18}$$

Observing Figure D.1, it can be noted that at $t = T_s$:

$$I_{2c} = i_2(T_s) = \frac{i_{Lm}(T_s) - i_{Lk}(T_s)}{n} = \frac{I_m - 0}{n} \tag{D.19}$$

Finally, for the calculation of I_{2b}, the expression of i_2 for the period $(1 - D - D_x)T_s$, corresponding to the dashed line in Figure A.1, can be derived as follows:

$$i_2(t) = \frac{nI_{2c} - I_M}{n(1-D)T_s} t + \frac{I_M}{n} \text{ para } t \geq t_c + t_x \tag{D.20}$$

At $t_c + t_x$:

$$I_{2b} = i_2(t_c + t_x) = \frac{nI_{2c} - I_M}{n(1 - D)T_s} D_x T_s + \frac{I_M}{n} \tag{D.21}$$

Current in diode D_2:

A more in-depth analysis can be found in [5], and the values of the currents in diode D_2 for gain cells I, III, and V (which have de parameter p=1, as seen in Chapter 3) are:

$$I_{D2a} = -I_{2a} \frac{(1 - p)}{2} \tag{D.22}$$

$$I_{D2b} = I_{2b} \frac{(1 + p)}{2} \tag{D.23}$$

$$I_{D2C} = I_{2C} \frac{(1 + p)}{2} \tag{D.24}$$

Currents in the gain cell diodes:

In a gain cell, there can be diodes that conduct simultaneously with diode D_2. These diodes have the same waveform as the current i_{D2} and will be represented by D_{GC2}, as indicated in (D.25). The other diodes present in the gain cell, referred to as D_{GC1}, conduct the portion of the current i_2 during the time interval in which diode D_1 is blocked, and these currents are (D.26), (D.27) and (D.28). The parameters a and b for each gain cell were shown in Chapter 3.

$$I_{Dcg2} = I_{D2} \tag{D.25}$$

$$I_{Dcg1a} = -\frac{I_{2a}}{[(a + b) - 1]} \frac{(1 + p)}{2} \tag{D.26}$$

$$I_{Dcg1b} = -\frac{I_{2b}}{[(a + b) - 1]} \frac{(1 - p)}{2} \tag{D.27}$$

$$I_{Dcg1c} = -\frac{I_{2c}}{[(a+b)-1]}\frac{(1-p)}{2} \tag{D.28}$$

Next, the root-mean-square (RMS) current values, peak voltage values and other important quantities from [5] are presented. It is worth noting that substitutions will not be performed, as this action would lead to lengthy expressions.

RMS value of the current in the leakage inductor L_k:

$$I_{Lkrms} = \sqrt{\frac{D}{3}\left({I_m}^2 + I_m I_{Lkp} + {I_{Lkp}}^2\right) + \frac{D_x}{3}{I_M}^2} \tag{D.29}$$

RMS value of the current in switch S_1:

$$I_{S1rms} = \sqrt{\frac{D}{3}\left({I_m}^2 + I_m I_{Lkp} + {I_{Lkp}}^2\right)} \tag{D.30}$$

RMS value of the current in diode D_1:

$$I_{D1rms} = \sqrt{\frac{D_x}{3}{I_M}^2} \tag{D.31}$$

RMS value of the current in the secondary winding of the coupled inductor:

$$I_{2rms} = \sqrt{\frac{D}{3}{I_{2a}}^2 + \frac{D_x}{3}{I_{2b}}^2 + \frac{1-D-D_x}{3}\left({I_{2b}}^2 + I_{2b}I_{2c} + {I_{2b}}^2\right)} \tag{D.32}$$

RMS value of the current in diode D_2:

$$I_{D2rms} = \sqrt{\begin{matrix}\frac{D}{3}{I_{D2a}}^2 + \frac{D_x}{3}{I_{D2b}}^2 + \cdots \\ + \frac{1-D-D_x}{3}\left({I_{D2b}}^2 + I_{D2b}I_{D2c} + {I_{D2b}}^2\right)\end{matrix}} \tag{D.33}$$

RMS value of the current in diode D_{GC1}:

$$I_{Dcg1rms} = \sqrt{\begin{matrix}\frac{D}{3}{I_{Dcg1a}}^2 + \frac{D_x}{3}{I_{Dcg1b}}^2 + \cdots \\ + \frac{1-D-D_x}{3}\left({I_{Dcg1b}}^2 + I_{Dcg1b}I_{Dcg1c} + {I_{Dcg1b}}^2\right)\end{matrix}} \tag{D.34}$$

RMS value of the current in diode D_{GC2}:

$$I_{Dcg2rms} = I_{D2rms} \tag{D.35}$$

Peak value of the voltage across switch S_1:

$$V_{S1p} = V_B = \frac{1}{1-D} V_i \tag{D.36}$$

Peak value of the voltage across diode D_1:

$$V_{D1p} = V_B = \frac{1}{1-D} V_i \tag{D.37}$$

Peak value of the voltage across diode D_2, D_{GC1}, and D_{GC2} :

$$V_{D2p} = V_{Dcgp} = V_a + V_b = \frac{n}{1-D} V_i \tag{D.38}$$

Input current i_i:

$$i_i = i_{Lk} \tag{D.39}$$

Current in capacitors C_1 and C_2:

$$i_{C1} = i_{D1} - i_{D2} \tag{D.40}$$

$$i_{C2} = i_{D2} - i_o \tag{D.41}$$

Voltage across capacitors C_1 and C_2:

$$V_{C1} = \frac{1}{1-D} V_i + \frac{D_x}{1-D} V_{Lk2} \tag{D.42}$$

$$V_{C2} \cong V_o \tag{D.43}$$

Output Capacitor C_2:

$$C_2 \geq \frac{D T_s I_o}{\Delta V_o} \tag{D.44}$$

Where ΔV_o is the output voltage ripple, that in this project was considered 5%.

Capacitors C_1 and C_{GC}:

$$C_1 = C_{cg} \geq \frac{4(a+b)}{\pi^2 {f_s}^2 n^2 L_k} \tag{D.45}$$

APPENDIX E – Prototype Schematic